

Air Force Institute of Technology AFIT Scholar

Theses and Dissertations

Student Graduate Works

9-10-2010

Improving Range Estimation of a 3D FLASH LADAR via Blind Deconvolution

Jason R. McMahon

Follow this and additional works at: <https://scholar.afit.edu/etd>

Part of the [Electrical and Electronics Commons](#), and the [Electromagnetics and Photonics Commons](#)

Recommended Citation

McMahon, Jason R., "Improving Range Estimation of a 3D FLASH LADAR via Blind Deconvolution" (2010). *Theses and Dissertations*. 1971.
<https://scholar.afit.edu/etd/1971>

This Dissertation is brought to you for free and open access by the Student Graduate Works at AFIT Scholar. It has been accepted for inclusion in Theses and Dissertations by an authorized administrator of AFIT Scholar. For more information, please contact richard.mansfield@afit.edu.



IMPROVING RANGE ESTIMATION OF A
3-DIMENSIONAL FLASH LADAR
VIA BLIND DECONVOLUTION

DISSERTATION

Jason R. McMahon, Major, USAF

AFIT/DEE/ENG/10-13

DEPARTMENT OF THE AIR FORCE
AIR UNIVERSITY

AIR FORCE INSTITUTE OF TECHNOLOGY

Wright-Patterson Air Force Base, Ohio

APPROVED FOR PUBLIC RELEASE; DISTRIBUTION UNLIMITED.

The views expressed in this dissertation are those of the author and do not reflect the official policy or position of the United States Air Force, Department of Defense, or the United States Government.

AFIT/DEE/ENG/10-13

IMPROVING RANGE ESTIMATION OF A
3-DIMENSIONAL FLASH LADAR
VIA BLIND DECONVOLUTION

DISSERTATION

Presented to the Faculty
Graduate School of Engineering and Management
Air Force Institute of Technology
Air University
Air Education and Training Command
In Partial Fulfillment of the Requirements for the
Degree of Doctor of Philosophy

Jason R. McMahon, BSEE, MSEE
Major, USAF

September 2010

APPROVED FOR PUBLIC RELEASE; DISTRIBUTION UNLIMITED.

IMPROVING RANGE ESTIMATION OF A
3-DIMENSIONAL FLASH LADAR
VIA BLIND DECONVOLUTION

Jason R. McMahon, BSEE, MSEE
Major, USAF

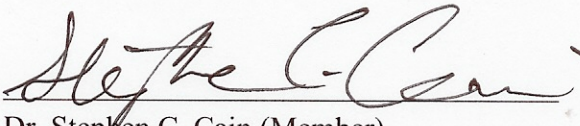
Approved:

Date



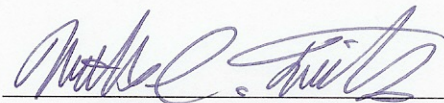
Dr. Richard K. Martin (Chairman)

13 July 2010



Dr. Stephen C. Cain (Member)

13 July 2010



Dr. Matthew C. Fickus (Member)

13 July 2010

Accepted:

M. U. Thomas

Dean, Graduate School of Engineering and Management

Date

Abstract

The purpose of this research effort is to improve and characterize range estimation in a three-dimensional FLASH LAsER Detection And Ranging (3D FLASH LADAR) by investigating spatial dimension blurring effects. The myriad of emerging applications for 3D FLASH LADAR both as primary and supplemental sensor necessitate superior performance including accurate range estimates. Along with range information, this sensor also provides an imaging or laser vision capability. Consequently, accurate range estimates would also greatly aid in image quality of a target or remote scene under interrogation.

Unlike previous efforts, this research accounts for pixel coupling by defining the range image mathematical model as a 2D convolution between the system spatial impulse response and the object (target or remote scene) at a particular range slice. Using this model, improved range estimation is possible by object restoration from the data observations. Object estimation is principally performed by deriving a blind deconvolution Generalized Expectation Maximization (GEM) algorithm with the range determined from the estimated object by a normalized correlation method. Theoretical derivations and simulation results are verified with experimental data of a bar target taken from a 3D FLASH LADAR system in a laboratory environment. Simulation examples show that the GEM object restoration improves range estimation over the unprocessed data and a Wiener filter method by 75% and 26% respectively. In the laboratory experiment, the GEM object restoration improves range estimation by 34% and 18% over the unprocessed data and Wiener filter method respectively.

This research also derives the Cramer-Rao bound (CRB) on range separation estimation of two point sources interrogated by a 3D FLASH LADAR system. Using an unbiased estimator, range separation estimation variance was attained through simulation and compared favorably to the range separation CRB theory. The results show that the CRB does indeed provide a lower bound on the range separation estimation variance and that the es-

imator is nearly efficient. With respect to the estimator, traditional pixel-based estimators like peak detection and matched filtering are biased because they assume there is only one target in the pixel. Therefore, an unbiased estimator was derived accounting for the possibility of two targets within a single pixel.

Additionally, among other factors, the range separation CRB is a function of two LADAR design parameters (range sampling interval and transmitted pulse-width), which can be optimized using the expected range resolution between two point sources. Typically, a shorter transmitted pulse-width corresponds to better range resolution (the ability to resolve two targets in range). Given a particular range sampling capability determined by the receiver electronics, the CRB theory shows there is an optimal pulse-width where a shorter pulse-width would increase estimation variance due to the under-sampling of the pulse and a longer pulse-width would degrade the resolving capability. Using both CRB theory and simulation results, an investigation is accomplished that finds the optimal pulse-width for several range sampling scenarios. For example, given a Gaussian received pulse model sampled every 1.876 ns, both range separation CRB theory and simulation predict an optimal pulse-width standard deviation equal to 0.88 ns. As the speed of the optical receiver is increased, the range resolution is improved with a corresponding narrower optimal pulse-width attained by the ability to sufficiently sample a shorter pulse-width. Conversely, the optimal pulse-width is wider with slower electronics with an associated negative impact on range resolution.

Acknowledgements

I would like to thank my family and friends for supporting me through this academic journey which was filled with discovery, hard work, and laughter. Special thanks goes to my wife and children who provided love, support, positive distractions, and encouragement. A substantial “thank you” also goes to my advisor, Dr. Richard Martin, whose guidance and advice was indispensable. Finally, I am most grateful to the giants whose shoulders I stood upon while completing my degree.

Jason R. McMahon

Table of Contents

	Page
Abstract	iv
Acknowledgements	vi
List of Figures	x
List of Tables	xii
I. Introduction	1
1.1 Motivation	2
1.2 3D FLASH LADAR Research Contributions	4
1.2.1 Improving Range Estimation by Spatial Processing (Chapter V)	4
1.2.2 Unbiased Two Point Target Temporal and Spatial Estimator (Chapter IV)	4
1.2.3 Lower Bound on Range Separation Estimation Vari- ance (Chapter VI)	4
1.2.4 Optimal Pulse-Width based on Range Resolution (Chapter VI)	5
1.3 Organization	5
II. Background	7
2.1 LADAR Imaging Theory	7
2.1.1 Description of Light	8
2.1.2 Optical Field Propagation	9
2.1.3 Impulse Response of an Imaging System with a Thin Lens	12
2.1.4 Optical Imaging as a Linear and Nonlinear System	15
2.1.5 Coherence Theory and Laser Light Statistics	16
2.2 Deconvolution	23
2.2.1 Inverse Filtering	24
2.2.2 Iterative Algorithms	26
2.3 Maximum Likelihood	29
2.4 Generalized Expectation Maximization	31
2.5 3D FLASH LADAR Data Model	33
2.6 Previous Research	42
2.6.1 3D FLASH LADAR	43
2.6.2 3D FLASH LADAR Post-Processing	47
2.6.3 Blind Deconvolution	53
2.6.4 CRB and Parameter Optimization	56

	Page
III. Laboratory Data Collection	58
3.1 3D FLASH LADAR Hardware Description	58
3.2 Data Collection Details	61
3.3 Spatial Aliasing	62
3.4 Data Pre-processing	63
3.5 Experimental PSF	66
3.6 Speckle Parameter Estimation – Incoherent Imaging	67
IV. Range Estimation	71
4.1 Peak Detection	71
4.2 Maximum Likelihood	72
4.3 Normalized Cross-Correlation	74
4.4 Two Point Target Range and Spatial Separation Estimator	76
4.4.1 Two Point Target Data Model	76
4.4.2 Estimator Derivation	79
4.5 Pixel-Dependent Two Surface Range Separation Estimator	81
V. Improving 3D FLASH LADAR Range Estimation via Object Recovery	84
5.1 Theoretical Development	86
5.1.1 Object Deconvolution	87
5.1.2 <u>Pulse-Shape Blind Deconvolution via the GEM Algorithm</u>	88
5.1.3 <u>Object Blind Deconvolution via the GEM Algorithm</u>	96
5.2 Simulation	101
5.3 Experimental Results	108
5.4 Conclusions	110
VI. Range Separation Performance and Optimal Pulse-Width Prediction of a 3D FLASH LADAR using the Cramer-Rao Bound	112
6.1 CRB on Range Separation Estimation	113
6.2 Range Separation Estimation Results	120
6.3 Optimal Pulse-width Investigation	121
6.3.1 Optimal Pulse for Two Point Target	124
6.3.2 Optimal Pulse for Complex Targets	126
6.3.3 Optimal Pulse for a Two Point Target using Normalized Pulse Definition	132
6.4 Conclusions	134

	Page
VII. Summary	135
7.1 Chapter Summary	135
7.2 Summary of Contributions	136
7.2.1 Improving Range Estimation by Spatial Processing	136
7.2.2 Unbiased Two Point Target Temporal and Spatial Estimator	137
7.2.3 Lower Bound on Range Separation Estimation . .	137
7.2.4 Optimal Pulse-Width based on Range Resolution .	138
7.3 Future Research	138
7.3.1 Outlier Detection	139
7.3.2 Foliage PENetration (FOPEN) Capability Investigation	139
7.3.3 Pixel Impulse Response Deconvolution	139
7.3.4 Object blind deconvolution using partially coherent light model	140
Bibliography	141

List of Figures

Figure		Page
2.1	Simplified depiction of a 3D FLASH LADAR imaging system.	9
2.2	Speckle parameter effect on negative binomial distribution.	21
2.3	Pictorial views 3D FLASH LADAR operation.	34
2.4	Signal definitions for the simple and high fidelity models.	35
2.5	Diffraction limited OTF.	39
2.6	Diffraction limited OTF cut-outs.	40
2.7	Organizational chart for the literature review.	42
3.1	Picture of ASC FLASH LADAR.	60
3.2	True ranges for the three-bar target.	62
3.3	Pixel gain correction.	64
3.4	Step target and experimental PSF and OTF.	68
3.5	Estimated average speckle parameter for 3D FLASH LADAR.	70
4.1	Representations of the two point target scene.	77
5.1	Pictorial views 3D FLASH LADAR operation.	85
5.2	True ranges for simulation targets.	103
5.3	Estimated ranges for simulation targets	104
5.4	Comparing waveforms with and without object recovery using the GEM _o algorithm	106
5.5	Estimated ranges for experimental target using GEM _o algorithm	109
6.1	Range separation CRB example	117
6.2	Parameter effects on range separation CRB	119
6.3	Two point target simulation results.	122
6.4	CRB compared to simulation estimation variance.	123
6.5	Range resolution example.	124
6.6	Optimal pulse-width investigation results.	125

Figure		Page
6.7	Optimal pulse-width percentage changes for different range sampling cases.	126
6.8	Optimal pulse results for a multi-bar target.	128
6.9	Optimal pulse results for a three-bar target.	128
6.10	Optimal pulse results for a connected blocks target.	129
6.11	Estimation statistics across pulse-widths along different range separations for the multi-bar target.	130
6.12	Estimation statistics across range separations along different pulse-widths for the multi-bar target.	131
6.13	Optimal pulse results using normalized method.	133

List of Tables

Table		Page
3.1	3D FLASH LADAR parameters	59
5.1	3D FLASH LADAR parameters	102
5.2	Range estimation results for simulation data	107
5.3	Range estimation results for experimental data	109
6.1	Optimal pulse-width results - two point target	124
6.2	Optimal pulse-width results - complex targets	127

IMPROVING RANGE ESTIMATION OF A 3-DIMENSIONAL FLASH LADAR VIA BLIND DECONVOLUTION

I. Introduction

The ability to accurately view a remote scene has long been a human military endeavor. From primeval warriors using mountains or trees to see troop formations with their naked eye to early seafarers using primitive optics to assess ship capabilities or harbor defenses to today's combatants operating advanced optics (manned and unmanned platforms) and imaging satellites to observe troop or missile movements, the advantage to the military that can accurately assess the remote battlefield has never been questioned.

With modern technology development, remote sensing has advanced and, in one particular sensor area, has bonded with another indispensable military capability: *Radio Detection And Ranging* (RADAR). Since World War II, RADAR capability has been a critical technology with respect to offensive and defensive capabilities and missile defense. Advances in RADAR have steadily progressed since the early effective use of RADAR by Great Britain against Germany in the Battle of Britain. However, RADAR is fundamentally limited in some ways by its operating wavelength in the electromagnetic spectrum. One of the latest advancements in the field of RADAR is adapting the use of lasers to the ranging issue and developing a *LAsEr Detection And Ranging* (LADAR) system. LADAR allows for the benefit of a smaller operating wavelength (e.g., resolution and material interaction) and the directionality of laser transmissions (which are ideal for urban environment interrogation) while still retaining the imaging and ranging benefit of a traditional RADAR. Just as there is no one branch of the military that can operate independently in the modern battlefield, a LADAR is not meant to be a panacea and there are applications where RADAR is still preferred. Though, as the technology continues to mature, LADAR will be an invaluable contributor in imaging and ranging sensor suite available to the warfighter.

Motivation for this research effort is accomplished in this chapter by introducing LADAR and explaining the importance of range estimation. Specifics of the research contributions are described with corresponding benefits. Finally, the document organization is given.

1.1 Motivation

The driving force behind this research endeavor is to adopt a realistic physical model for the return signals of a three-dimensional FLASH LAsER Detection And Ranging (3D FLASH LADAR) and then develop methods of improving the most vital unknown parameter from that model: range to target. More precise range measurements aid intelligence gathering, target recognition, mapping, imaging, object classification, navigation, and precision strike capabilities. The trend towards computer vision systems with active illumination necessitates the use of 3D FLASH LADARs capable of rapid range data acquisition with a wide enough field of view (FOV) to allow the operator access to an appropriate battlefield representation. By acquiring the remote scene in this manner, however, the sensor will be negatively affected by the spatial blurring inherent in the image formation process.

The importance of being able to correctly range to the remote environment is characterized by General T. Michael Moseley in a 2007 CSAF white paper:

The Air Force is often first to the fight and last to leave. We give unique options to all Joint Force Commanders. The Air Force must safeguard our ability to: see anything on the face of the earth; **range** it; observe or hold it at risk; supply, rescue, support or destroy it; assess the effects; and exercise global command and control of all these activities. Rising to the 21st Century challenge is not a choice. It is our responsibility to bequeath a dominant Air Force to Americas joint team that will follow us in service to the Nation [57].

Unlike 3D scanning LADARs that build a 3D scene by rastering multiple laser scans with a dwell required at each point, a 3D FLASH LADAR system produces a set of sequential two-dimensional (2D) images due to a fast range gate (i.e. shutter) resulting in a three-dimensional data cube (spatial and range) of the remote scene. In reality, the sensor captures a fourth dimension which is the photo-electron count for each volume element (voxel). Each 2D range slice image contains the detected photo-electrons at each pixel for

a particular range. The photo-electron counts are directly proportional to the return signal intensities incident upon the detector. Unique to the FLASH LADAR sensors, each pixel in the array detects its own attenuated and time-delayed version of the transmitted signal. Investigating pixel data, the blurring effects are evident in the pixel's received waveform.

3D FLASH LADAR range estimation errors of a remote scene can occur due to several system factors including the optical spatial impulse response (diffraction limited, atmospheric turbulence), detector blurring, photon noise, and readout noise. These factors either cause the scene's intensity to spread, or blur, across pixels or add unwanted and disruptive noise effects. The intensity spreading and noise corrupts the correct pixel intensities at each range gate by mixing intensities with neighboring pixels thereby providing false intensity values and therefore incorrect photon counts to the range estimator. Without blur and noise compensation, the range estimates would then be inaccurate to a degree depending on the blur and noise severity.

3D FLASH LADAR's popularity is increasing due to its small size, rapid image acquisition, and range resolving capabilities. There are several examples that highlight applications in practical situations: As part of its return to flight efforts following the Columbia disaster, NASA uses a 3D imaging LADAR to inspect the integrity of the Space Shuttle's Thermal Protection System prior to reentry [45]. Sandia National Laboratory developed a counter-sniper 3D coherent detection LADAR sensor designed to trace the source of the bullet by optical signature and bullet trajectory analysis [74].

Augmenting the FLASH technology to the LADAR's active sensing capability, the possibilities of future technology include remote video feeds from airborne or spaceborne platforms to command and control centers, precise autonomous navigation in GPS-denied regions, autonomous precision strike with guided cruise missiles or intelligent gravity munitions, and battlefield awareness in day/night conditions for airborne or ground forces in dynamic environments.

1.2 3D FLASH LADAR Research Contributions

1.2.1 Improving Range Estimation by Spatial Processing (Chapter V). Previous work in 3D FLASH LADAR has only modeled an ideal return per pixel and not the real world effects of spatial blurring [9], [38]. This research will enhance the model by adding the spatial impulse response thereby considering all the pixel's signals in the range estimation algorithm for a particular pixel. The benefit of this research is for future implementation in an operational environment. Previously, a 3D representation of a remote scene was built by single-pixel LADAR scanners. Consequently, the scanning 3D LADARs have limited spatial extents on each collect and do not see the effects of spatial blurring. As laser vision hardware improves, the development will trend towards FLASH systems that capture scene data very rapidly over a large pixel array. Given proper spatial sampling, this method of data capture would see the effects of spatial blurring. The spatial blurring would contribute negatively to current methods of range estimation because each pixel's return waveform would interact with those of its neighboring pixels. New estimation solutions must be developed that account for these blurring effects and essentially "deblur" the data to increase range estimation performance. This research builds this enhanced model and improves range estimation by spatially processing the data using a well-known spatial filter (deconvolution) and a novel object recovery algorithm (blind deconvolution) [56].

1.2.2 Unbiased Two Point Target Temporal and Spatial Estimator (Chapter IV). This contribution supports the CRB work from the previous section. Given the two target model, conventional pixel-based estimators like peak detection and matched filtering are biased because they assume there is only target in the pixel. Therefore, an unbiased estimator was developed accounting for the possibility of two targets within a single pixel. Based on a least sum squares approach, the ability to sufficiently estimate the ranges and amplitudes of two point targets is developed and verified to be unbiased.

1.2.3 Lower Bound on Range Separation Estimation Variance (Chapter VI). An important metric of a physical model with several unknowns is to understand the optimal es-

estimator variance achievable regardless of the specific estimation scheme. The Cramer-Rao Bound (CRB) provides the lower bound on estimator variance given an unbiased estimator. Previous CRB work in 3D FLASH LADAR adopted a physical model that did not account for the spatial blurring between pixels [9], [38]. The benefit of including these spatial effects in the CRB development is that the estimation and CRB results would now be negatively affected by the signals from adjacent pixels to a degree depending on the pixel range differences. A two point target scene model is adopted to show the CRB on range separation estimation. The effects of changing the separation are shown to drastically affect the ability to estimate that separation.

1.2.4 Optimal Pulse-Width based on Range Resolution (Chapter VI). Utilizing the CRB and unbiased two point target range separation estimator, a method is developed where an optimal pulse-width is determined based on the expected range resolution using the two point target model. Typically, a shorter transmitted pulse-width corresponds to better range resolution (the ability to estimate two distinct targets in range). Given a particular range sampling capability determined by the receiver electronics, the CRB and simulation shows there is an optimal pulse-width where a shorter pulse-width would increase estimation variance due to the under-sampling of the pulse and a longer pulse-width would degrade the resolving capability. Using two distinct and separate techniques of CRB and simulation, an investigation is accomplished that finds the optimal pulse-width for several range sampling scenarios. Benefits of this analysis include the ability to aid in LADAR system design using independent statistical methods (CRB).

1.3 Organization

The dissertation is organized as follows: Chapter II provides background theory, data model, and a discussion of previous LADAR research. Chapter III details the 3D FLASH LADAR hardware used in experimental collects as well as the procedures used to condition the data for appropriate use for the selected mathematical model. Chapter IV contains the pertinent pixel-based range estimation algorithms. Chapter V shows that object recovery

does improve range estimation. Chapter VI derives the CRB for range separation estimation and predicts an optimal pulse-width that provides the best range resolution. Finally, Chapter VII summarizes the research contributions and outlines future research opportunities.

II. Background

This chapter serves as a review of background theory and previous research related to three-dimensional FLASH LAsER Detection And Ranging (3D FLASH LADAR). The focus on the theory and literature review will be related to the major topic areas: range estimation, spatial processing, performance bounding, and optimal parameter selection.

This chapter is organized as follows: Section 2.1 discusses imaging and coherence theory and how it applies to 3D FLASH LADAR. Sections 2.2, 2.3, and 2.4 discuss deconvolution, maximum likelihood parameter estimation, and the Generalized Expectation Maximization (GEM) algorithm respectively. Section 2.5 describes the data model that will be used in Chapters III, IV, and V. Finally, Section 2.6 reviews previous research related to LADAR data processing, blind deconvolution, bounding performance, and parameter optimization.

2.1 LADAR Imaging Theory

The goal of this section is to describe the 3D FLASH LADAR imaging operation as a linear and spatially-invariant system. Linear systems theory has many benefits with the chief benefit of being able to describe the observed data (image) as a convolution of the object's intensity with a spatial impulse response. This convolution is an integral part of the mathematical model used in this research describing the detected photons in the 3D FLASH LADAR. The spatial impulse response completely describes the optical system to include any random atmospheric disturbance. The argument that optical imaging can be cast in the linear system framework has been established in the literature [24], [25]. Similar arguments are made here to verify that this framework is applicable to this research. A foundational understanding of why this object-image relationship holds is key because it allows the use of object reconstruction algorithms from the simple inverse filter to the more complicated blind deconvolution methods. First, a method is needed to accurately describe the illuminating light's movement and interaction with its environment and how light propagates. Following, the linear system framework can be constructed with an example of a spatial impulse response for a simple imaging system.

2.1.1 Description of Light. From [30], there are three mathematical descriptions in which the light used in optical imaging systems can be described. They are geometrical optics, quantum optics, and physical (wave) optics.

The simplest and least accurate mathematical model is called geometrical optics (GO) and is a good approximation when wavelengths are small compared to the dimensions of the optics. GO analysis operates on the principle of light described as rays and is a valid technique to determine basic properties of an imaging system like object distance, magnification, and pixel area at the target. For instance, the location of an object's image through an imaging system is based on the ray tracing method. While being able to show optical aberrations, GO does not handle diffraction or interference effects and predicts the location of an image to be a point (without aberrations). The blurring of the imaging system is not accounted for in GO which makes it a poor choice to describe light propagation in this research.

From [30], the most accurate and complex mathematical description of light is called quantum optics (QO) and is valid in all optical scenarios (wavelength, irradiance levels, and optic dimensions). In QO, light is considered an electromagnetic wave with its energy quantized into massless particles called photons rather than a continuous wave. While being the most physically accurate, computations tend to be slow and cumbersome. Concerning imaging applications, the extra time and resources required for QO is not beneficial when trying to understand and mitigate the macroscopic light blurring effects of an optical system.

Also from [30], the remaining mathematical method is called physical optics (PO), or wave optics, in which the light is considered to propagate as a transverse electromagnetic wave. In general, PO can be used to describe diffraction and interference effects by Maxwell's equations using a scalar theory approximation. Rather than a vector-based theory, scalar theory is valid for describing light behavior when the wavelength of the light is much less than the dimensions of the diffracting objects and when traveling through a uniformly dielectric medium. Whereas GO describes an image to be a point, PO utilizes

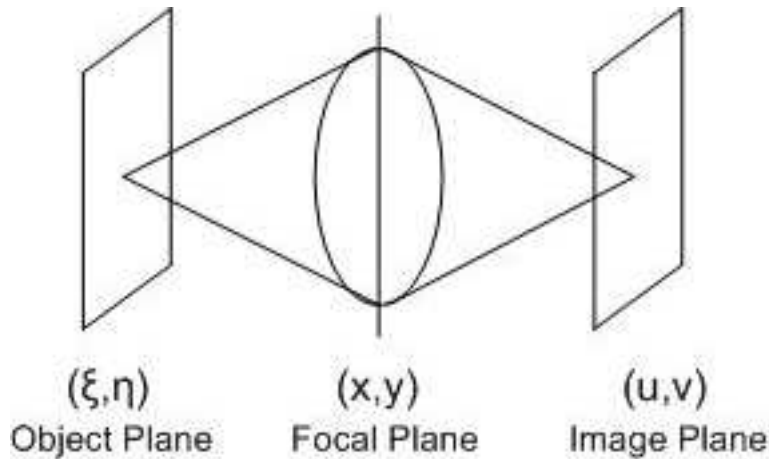


Figure 2.1: Simplified depiction of an imaging system. In the 3D FLASH LADAR, the object is the target under illumination, the lens are the front end optics, and the image would be the 2D range slice image of the intensity return from the object at a particular return time.

diffraction effects through the optical system to depict the image spread about the point that GO predicted. While there may be situations where the physical optics assumptions and approximations fail, the more accurate quantum optics approach tends to be impractical due to increased complexity and processing times for operational use. In most practical situations, PO is sufficient to describe the light's movement and interactions with structures given high enough irradiance levels.

A common practice in imaging systems is to treat light as an electromagnetic wave using PO until the light hits the detector in which the light is then considered a particle or photon. This assumption allows for the benefit of the dual nature of light and will be adopted for this research. Furthermore, PO is sufficiently accurate to describe an optical imaging system as a linear system.

2.1.2 Optical Field Propagation. Based on [25] and referring to Figure 2.1, the purpose of this section is to be able to describe how to mathematically propagate an optical field from one plane to another with varying levels of accuracy. In order to mathematically propagate an optical field, a diffraction formula must be used due to the many point sources in the observation plane.

Through Maxwell's equations, the Huygens-Fresnel principle, and Kirchhoff's theory, a closed-form mathematical solution for the optical field at a remote point can be attained called the Rayleigh-Sommerfeld diffraction formula. This diffraction formula is a general result from scalar diffraction theory with the only assumptions lying within scalar diffraction theory. With monochromatic and narrowband assumptions, the Rayleigh-Sommerfeld diffraction formula is given by the following equation for the complex phasor U_a of the scalar optical field at a distance z away from the source field U [25]:

$$U_a(u, v) = \int_{-\infty}^{\infty} \int_{-\infty}^{\infty} \frac{U(\xi, \eta) e^{\frac{j2\pi R(\xi, \eta, u, v)}{\lambda}}}{j\lambda R(\xi, \eta, u, v)} d\xi d\eta \quad (2.1)$$

where (u, v) are observation plane coordinates, (ξ, η) are source plane coordinates, λ is the mean wavelength, and $R(\xi, \eta, u, v) = \sqrt{z^2 + (\xi - u)^2 + (\eta - v)^2}$ is the distance between every point in the source plane to every point in the observation plane. The complex phasor is related to the scalar optical field by

$$\mathbf{u}_a(u, v, t) = \text{Re} \{U_a(u, v) \exp(-j2\pi\nu t)\} \quad (2.2)$$

where $\text{Re} \{ \}$ means the "real part", $j = \sqrt{-1}$, ν is the frequency of the light, and t signifies time. The optical field theory focuses on the complex phasor U development since the time dependence is already known [25].

A useful simplification called the Fresnel approximation (near-field or paraxial approximation) can be employed to reduce the complexity of the range term, although the two instances of the range term need to be handled differently. Small errors in range term in the denominator are usually not critical due to the range to target (z) being much, much bigger than the spatial extents in the observation and image plane. Conversely, small errors in the range term residing in the exponential can be significant given that it is divided by the light's wavelength which is on the order of hundreds of nanometers in the light or infrared

spectrum. Using the binomial approximation for R in the exponential results in

$$\begin{aligned}
R &= \sqrt{z^2 + (\xi - u)^2 + (\eta - v)^2} \\
&= z\sqrt{1 + ((\xi - u)/z)^2 + ((\eta - v)/z)^2} \\
&\cong z\left(1 + 0.5((\xi - u)/z)^2 + 0.5((\eta - v)/z)^2\right) \\
&\cong z + \frac{(\xi - u)^2}{2z} + \frac{(\eta - v)^2}{2z}
\end{aligned} \tag{2.3}$$

and approximating $R \approx z$ in the denominator, results in the Fresnel diffraction formula given by [25]

$$U_a(u, v) \cong \frac{e^{j\frac{2\pi z}{\lambda}}}{j\lambda z} \int_{-\infty}^{\infty} \int_{-\infty}^{\infty} U(\xi, \eta) e^{j\frac{\pi}{\lambda z} [(\xi - u)^2 + (\eta - v)^2]} d\xi d\eta \tag{2.4}$$

which describes a convolution operation for the free space propagation of an optical field from one plane to another. A spatial impulse response (spatial point spread function) for free space propagation is then defined by

$$h(\xi, \eta) \cong \frac{e^{j\frac{2\pi z}{\lambda}}}{j\lambda z} e^{j\frac{\pi}{\lambda z} [\xi^2 + \eta^2]}. \tag{2.5}$$

It is interesting to note that even free-space propagation can be cast in the linear systems framework. A later section will make the argument that an imaging system can be represented as a linear system as well.

An alternate way to view the free-space Fresnel diffraction integral is by factoring out the variables that don't depend on the variables of integration and results in

$$U_a(u, v) = \frac{e^{j\frac{2\pi z}{\lambda}} e^{j\frac{\pi(u^2 + v^2)}{\lambda z}}}{j\lambda z} \int_{-\infty}^{\infty} \int_{-\infty}^{\infty} U(\xi, \eta) e^{j\frac{\pi(\xi^2 + \eta^2)}{\lambda z}} e^{-j\frac{2\pi(u\xi + v\eta)}{\lambda z}} d\xi d\eta. \tag{2.6}$$

which is a scaled Fourier Transform of the aperture field and the quadratic exponential. The Fresnel diffraction formula still accounts for the curvature of the wavefront, but assumes

a parabolic rather than spherical wavefront shape. While Equation (2.6) specifies the optical field (volts/meter) at a distance, the intensity at that point is the quantity of interest in imaging. Considering the wave is monochromatic, the intensity (watts/meter²) can be determined by taking the magnitude squared of the complex phasor of the optical field or $I_a(u, v) = |U_a(u, v)|^2$. When the wave is not monochromatic, the intensity becomes the time-average $\langle \cdot \rangle$ of the amplitude squared of the scalar optical field

$$I_a(u, v) = \langle |\mathbf{u}_a(u, v, t)|^2 \rangle \quad (2.7)$$

where $\mathbf{u}_a(u, v, t)$ was defined in Equation (2.2). All future references to an “optical field” refer to the complex phasor U unless explicitly stated otherwise.

Equation (2.4) or (2.6) can now be used to describe the imaging operation where optics are placed between the object and image. The next section summarizes the resulting impulse response of a general imaging scenario.

2.1.3 Impulse Response of an Imaging System with a Thin Lens. The purpose of this subsection is to illustrate an example of the impulse response from a simple imaging architecture. The imaging system converts the diverging spherical waves emanating from an object to converging spherical waves culminating at the image. The lens is assumed to be a thin lens meaning the light enters and leaves the lens at the same coordinates. Of course, there is a diameter to all lenses as well as irregularities that make this assumption invalid. However, it will suffice for the purposes of a theoretical understanding of the lens’ effect on incident light.

In general, the purpose of the imaging system is to reproduce an object in a better manner than possible without the system. With no aberrations, the geometrical optics analysis predicts a “perfect” image aside from a scaling term, although this image is only valid as the wavelength goes to infinity ($\lambda \rightarrow 0$). Wave optics predicts a more physically accurate image that is dominated by the effects of diffraction. As stated previously, a significant concept in this research is that the 3D LADAR is operating in a linear system. This assumption

allows for the LADAR to be entirely represented by a spatial impulse response. The images are then produced by the convolution of the object and spatial impulse response. The key is to be able to describe an optical imaging system by a spatial impulse response. By placing a point source in front of a lens, the impulse response of the lens can be attained. This lens impulse response is valid for compound or more complex optics since all the imaging system optics convert a diverging spherical wave into a converging spherical wave.

Under the general assumption of the linearity of wave propagation, the relationship between a field at the image and object plane can be given by a superposition integral [25]:

$$U_i(u, v) = \int_{-\infty}^{\infty} \int_{-\infty}^{\infty} h(u, v; \xi, \eta) U_o(\xi, \eta) d\xi d\eta \quad (2.8)$$

where U_i and U_o are the image and object plane optical field respectively and h is the impulse response and is an optical field at (u, v) produced by an amplitude point source at (ξ, η) . The spatial impulse response can describe optical systems from simple free-space to the most complicated optics. If the system is considered space invariant (i.e. an isoplanatic imaging situation exists) then h is $h(u - \xi, v - \eta)$ where Equation (2.8) is now a convolution integral. From [25], however, the Fresnel diffraction integral (Equation (2.4)) is used along with the phase transformation of a lens to derive the general form for a spatial impulse response of a single thin lens to be

$$\begin{aligned} h(u, v; \xi, \eta) &= \frac{1}{\lambda^2 z_1 z_2} e^{\frac{j2\pi}{z_2}(u^2+v^2)} e^{\frac{j2\pi}{z_1}(\xi^2+\eta^2)} \\ &\times \int_{-\infty}^{\infty} \int_{-\infty}^{\infty} P(x, y) \exp \left\{ j \frac{\pi}{\lambda} \left(\frac{1}{z_1} + \frac{1}{z_2} - \frac{1}{f} \right) (x^2 + y^2) \right\} \\ &\times \exp \left\{ -j \frac{2\pi}{\lambda} \left[\left(\frac{\xi}{z_1} + \frac{u}{z_2} \right) x + \left(\frac{\eta}{z_1} + \frac{v}{z_2} \right) y \right] \right\} dx dy \quad (2.9) \end{aligned}$$

with (u, v) being the image plane coordinates, (ξ, η) as the object plane coordinates, λ as the wavelength, z_1 as the distance from the object to focal plane, z_2 as the distance from the focal to image plane, f being the focal length, P as the pupil function, and (x, y) as the focal

plane coordinates. Using assumptions about the quadratic phase terms and normalizing the coordinates to eliminate effects of inversion and magnification, the general form reduces to a normalized point spread function

$$\tilde{h}(u, v) \cong \frac{A}{\lambda z_2} \mathfrak{F} [P(x, y)]_{f_x = \frac{u}{\lambda z_i}, f_y = \frac{v}{\lambda z_i}} \quad (2.10)$$

with A being the optical field amplitude, \mathfrak{F} as the Fourier transform operator, and (f_x, f_y) are the focal plane spatial frequency coordinates. It is only under specific conditions that Equation (2.10) results from the more general impulse response. First, the lens law must be satisfied:

$$\frac{1}{f} = \frac{1}{z_1} + \frac{1}{z_2} \quad (2.11)$$

which is a mandatory condition for imaging to occur and thus

$$\exp \left\{ j \frac{\pi}{\lambda} \left(\frac{1}{z_1} + \frac{1}{z_2} - \frac{1}{f} \right) (x^2 + y^2) \right\} \quad (2.12)$$

in Equation (2.9) reduces to unity. Second, since the goal of imaging is to obtain the intensity of the image, any multiplicative phase terms with dependence only on image plane coordinates can be discarded. In other words, the term $\exp \left(\frac{j2\pi}{z_2} (u^2 + v^2) \right)$ can be ignored. Finally, the quadratic phase term dependent on object plane coordinates, $\exp \left(\frac{j2\pi}{z_1} (\xi^2 + \eta^2) \right)$, is ignored by noting that the object is a point source and the span of the object coordinates are very small. Therefore, it would contribute a trivial amount to the intensity on the focal plane. With these three conditions satisfied, the impulse response for a thin lens takes the form of Equation (2.10).

This result is an example of an ideal impulse response for an optical imaging system. It is ideal in the sense that there are no aberrations or atmospheric turbulence. Using the principle planes concept from geometrical optics, most optics in an imaging systems can be considered a “thin lens” with light entering the system with one orientation and exiting at another orientation without regard to the inner optical structures. Thus, the thin lens impulse response is a good approximation or starting point for reconstruction algorithms.

2.1.4 *Optical Imaging as a Linear and Nonlinear System.* In order to validate the mathematical model adopted in this research, the relationship between the object intensity and image intensity needs to be a linear relationship. Depending on the coherence properties of the illuminating light, this linear relationship may or may not exist. This subsection gives examples of both. The next subsection concentrates on coherence theory, how it affects the object-image linear relationship, and why this research can assume a linear relationship between the object and image intensity does exist in a 3D FLASH LADAR.

Presented again for convenience, the relationship between a field at the image and object plane can be given by a superposition integral due to the linearity of wave propagation

$$U_i(u, v) = \int_{-\infty}^{\infty} \int_{-\infty}^{\infty} h(u, v; \xi, \eta) U_o(\xi, \eta) d\xi d\eta \quad (2.13)$$

where U_i and U_o are the image and object plane optical fields respectively and h is the impulse response and is an optical field at (u, v) produced by an amplitude point source at (ξ, η) . Again, if the system is considered space invariant (i.e. an isoplanatic imaging situation exists) then h is $h(u - \xi, v - \eta)$ where Equation (2.13) is now a convolution integral.

In a simplified imaging situation, the imaging system consists of an object, a lens, and an image. The ideal image predicted by geometrical optics is

$$U_g(u, v) = \frac{1}{|M|} U_o\left(\frac{u}{M}, \frac{v}{M}\right) \quad (2.14)$$

where M is the magnification and U_o is the object. This ideal image is the result of the superposition integral as $\lambda \rightarrow 0$. Using this result as the object plane amplitude in Equation (2.13), the field at image plane is a convolution of the impulse response and image predicted by geometrical optics [25]:

$$U_i(u, v) = h(u, v) \otimes U_g(u, v) \quad (2.15)$$

This result highlights the spreading effect that diffraction imposes on the ideal image.

Unless further propagation is necessary where the optical field is required, the optical intensity at the detector is the quantity of interest. Results for image intensity will be stated here and justified in the next section using coherence theory. The image intensity is the time-averaged, magnitude squared of the field and is defined by an intensity convolution for incoherent illumination

$$I_i(u, v) = |h(u, v)|^2 \otimes |U_g(u, v)|^2. \quad (2.16)$$

This result for image intensity is the important result of this section. It serves as the basis for the mathematical model and allows for advanced techniques for object restoration. If coherent illumination is encountered, the linear relationship for intensity vanishes and image intensity is defined by an amplitude convolution:

$$I_i(u, v) = |h(u, v) \otimes U_g(u, v)|^2. \quad (2.17)$$

which results in a non-linear relationship between the object and image. Clearly, it is seen that incoherent illumination is linear in intensity and coherent illumination is linear in amplitude. The spatial impulse response for incoherent illumination is the amplitude squared of the coherent illumination spatial impulse response.

It must be shown or proven that the 3D FLASH LADAR produces or approaches incoherent object illumination in order to develop algorithms for the recovery of the original object, U_g , using deconvolution algorithms. Otherwise, the mathematical model would change from object intensity (i.e. photon counts) to object field recovery in order to benefit from linear systems theory. Since the observed data is based on the image intensity, backing out the object field from coherent illumination would require other methods rather than deconvolution.

2.1.5 Coherence Theory and Laser Light Statistics. Using [24] and [25], this section serves as background on coherence theory and how to use this theory to express the

image intensity as in Equation (2.16) or (2.17). Coherence theory also dictates the statistics that govern the laser light incident on the detector surface.

The image intensity related to different types of coherence is governed by the laser light's spatial coherence between two points called mutual intensity. In order to understand how coherence affects imaging, the monochromatic light assumption has to be relaxed and the light model changed to polychromatic. This yields a generic optical scalar field defined by

$$\mathbf{u}(u, v, t) = \{U(u, v, t) \exp(-j2\pi\nu t)\}. \quad (2.18)$$

where the complex phasor is changed to be time-varying. The image plane complex phasor $U_i(u, v, t)$ results from a convolution between the impulse response and the object plane complex phasor $U_g(\xi, \eta, t)$. Neglecting the different time delays from different coordinates, the subsequent image plane intensity (from Equation (2.7)) becomes

$$\begin{aligned} I_i(u, v) &= \int_{-\infty}^{\infty} \int_{-\infty}^{\infty} d\xi_1 d\eta_1 \int_{-\infty}^{\infty} \int_{-\infty}^{\infty} d\xi_2 d\eta_2 h(u - \xi_1, v - \eta_1) h^*(u - \xi_2, v - \eta_2) \\ &\quad \times J_g(\xi_1, \eta_1; \xi_2, \eta_2) \end{aligned} \quad (2.19)$$

with the mutual intensity defined as

$$J_g(\xi_1, \eta_1; \xi_2, \eta_2) = \langle U_g(\xi_1, \eta_1; t) U_g^*(\xi_2, \eta_2; t) \rangle. \quad (2.20)$$

The physical properties of the two coherence extremum (fully coherent and fully incoherent) can be exploited to define mutual intensity. Considering coherent light, all the points in the field interfere with each other (statistically dependent) and it is characterized by the mutual intensity

$$J_g(\xi_1, \eta_1; \xi_2, \eta_2) = U_g(\xi_1, \eta_1) U_g^*(\xi_2, \eta_2) \quad (2.21)$$

and the resulting image intensity is

$$\begin{aligned}
I_i(u, v) &= \int_{-\infty}^{\infty} \int_{-\infty}^{\infty} h(u - \xi_1, v - \eta_1) U_g(\xi_1, \eta_1) d\xi_1 d\eta_1 \\
&\quad \times \int_{-\infty}^{\infty} \int_{-\infty}^{\infty} h^*(u - \xi_2, v - \eta_2) U_g^*(\xi_2, \eta_2) d\xi_2 d\eta_2 \\
&= \left[\int_{-\infty}^{\infty} \int_{-\infty}^{\infty} h(u - \xi, v - \eta) U_g(\xi, \eta) d\xi d\eta \right] \\
&\quad \times \left[\int_{-\infty}^{\infty} \int_{-\infty}^{\infty} h(u - \xi, v - \eta) U_g(\xi, \eta) d\xi d\eta \right]^* \\
&= \left| \int_{-\infty}^{\infty} \int_{-\infty}^{\infty} h(u - \xi, v - \eta) U_g(\xi, \eta) d\xi d\eta \right|^2 \tag{2.22}
\end{aligned}$$

where the relationship between the object and image intensity is described by the magnitude squared of an amplitude convolution relationship between the amplitude impulse response and object optical field.

For incoherent light, the object's phasor amplitudes are considered statistically independent from each other or, in other words, the amplitude at one point on the object does not affect the amplitude at a different point. The mutual intensity describing incoherent light is

$$J_g(\xi_1, \eta_1; \xi_2, \eta_2) = \kappa I_g(\xi_1, \eta_1) \delta(\xi_1 - \xi_2, \eta_1 - \eta_2) \tag{2.23}$$

with κ being a real constant and the resulting image intensity is

$$\begin{aligned}
I_i(u, v) &= \int_{-\infty}^{\infty} \int_{-\infty}^{\infty} d\xi_1 d\eta_1 \int_{-\infty}^{\infty} \int_{-\infty}^{\infty} d\xi_2 d\eta_2 \times h(u - \xi_1, v - \eta_1) h^*(u - \xi_2, v - \eta_2) \\
&\quad \times \kappa I_g(\xi_1, \eta_1) \delta(\xi_1 - \xi_2, \eta_1 - \eta_2) \tag{2.24}
\end{aligned}$$

and simplifying gives

$$\begin{aligned}
I_i(u, v) &= \kappa \int_{-\infty}^{\infty} \int_{-\infty}^{\infty} h(u - \xi, v - \eta) h^*(u - \xi, v - \eta) I_g(\xi, \eta) d\xi d\eta \\
&= \kappa \int_{-\infty}^{\infty} \int_{-\infty}^{\infty} |h(u - \xi, v - \eta)|^2 I_g(\xi, \eta) d\xi d\eta
\end{aligned} \tag{2.25}$$

where the image intensity is a result of an intensity convolution between the intensity point spread function and the object intensity. Equation (2.22) and (2.25) confirm (2.16) and (2.17) concerning the differences concerning intensity calculations between incoherent and coherent illumination.

In LADAR, it is common to collect many images to increase the signal to noise ratio (SNR) to better enable detection and data processing. An additional benefit is the partial coherence of the illumination tends to go from coherent to incoherent when averaging collects together. This fact is due to the many coherent images with correlated randomly varying phases and amplitudes combining to yield a statistically independent incoherent image map. Another way to look at why the coherent illumination goes to incoherent illumination from a statistical point of view is through the resulting probability mass function (PMF) of a partially coherent system. The PMF of a partially coherent system governing the probability of photons hitting the detector within one sampling interval is the the negative binomial distribution given by [24]

$$P_k(K) = \frac{\Gamma(K + M)}{\Gamma(K + 1)\Gamma(M)} \left[1 + \frac{M}{\bar{K}}\right]^{-K} \left[1 + \frac{\bar{K}}{M}\right]^{-M}, \quad k = 0, 1, 2, 3... \tag{2.26}$$

where $\Gamma(n) = (n - 1)!$ for any positive integer n , M is the speckle parameter dictating the amount of coherence, and \bar{K} is the expected number of photons. At the limits, $M = 1$ specifies totally coherence and $M = \infty$ leads to total incoherence. In practice, all systems fall somewhere in between the extremes, but assumptions can be made about which end of the spectrums dominates. A simple method to check the coherence limits from statistics is

to look at the mean and variance of the negative binomial distribution given by

$$\mu_{NB} = \bar{K} \quad (2.27)$$

$$\sigma_{NB}^2 = \bar{K} \left(1 + \frac{\bar{K}}{M} \right). \quad (2.28)$$

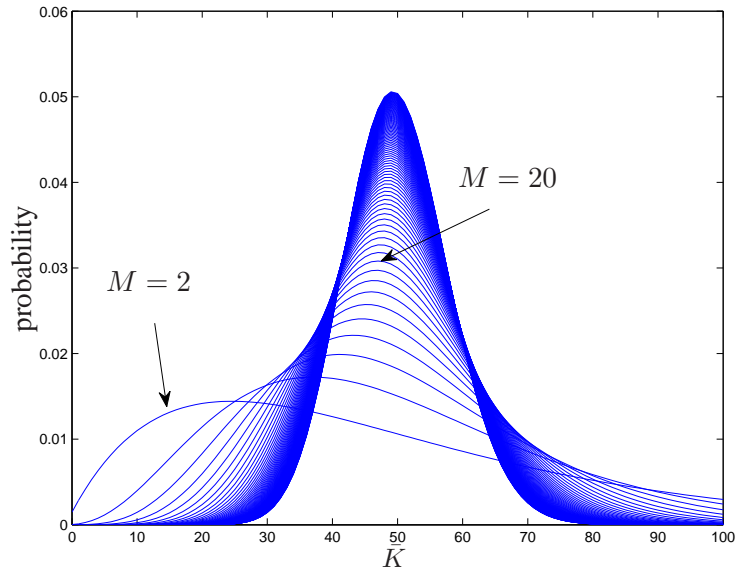
As the speckle parameter M increases towards infinity at the limit, the mean stays constant, but the variance changes to

$$\lim_{M \rightarrow \infty} \bar{K} \left(1 + \frac{\bar{K}}{M} \right) = \bar{K} \quad (2.29)$$

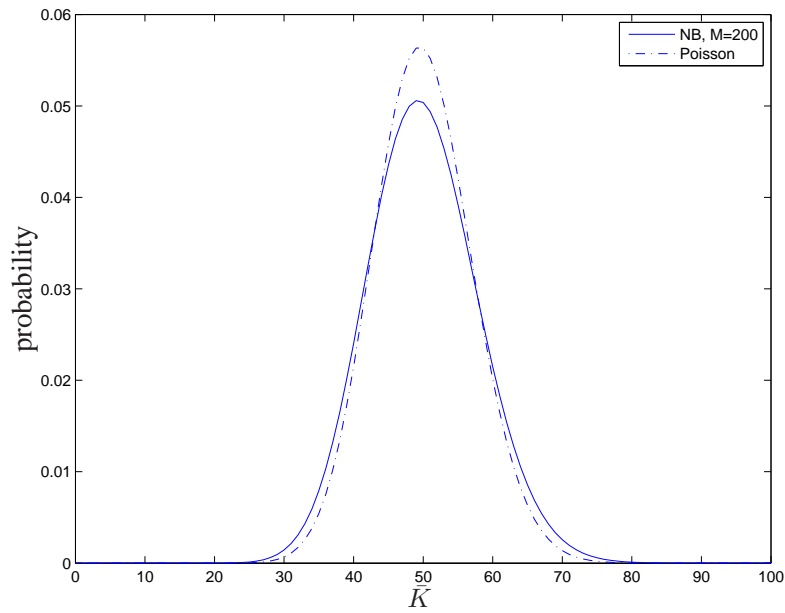
resulting in the mean and variance being equal. This fact is a characteristic of the Poisson distribution which has been derived independently to characterize the probability of photon hitting a detector given incoherent object illumination [24]. Figure 2.2 shows the effects of speckle parameter increase on the negative binomial PMF as it approaches the Poisson PMF.

The following question still needs to be answered explicitly: Can the 3D FLASH LADAR be considered to be a result of an incoherent imaging process? Are many cubes needed or just one? The two analytical methods to provide convincing proof center around obtaining a high speckle parameter in the partially coherent (negative binomial) PMF.

The first method to attain a high spatial speckle parameter is to take many independent collects of a particular remote scene. The speckle parameter for each collect is added together to yield a combined parameter which is typically high enough to assume incoherent object illumination. For example, with a mean number of photons of 50 ($\bar{K} = 50$), it takes a speckle parameter of about 200 for the negative binomial PMF to appear Poisson. This fact means that even if the light is totally coherent ($M = 1$) the resultant speckle parameter from summing the collects would be sufficient to assume incoherent object illumination. The obvious question then arises: Does an operator have both the time and loitering capability to take 200 collects of the exact same scene? Assuming the LADAR takes $6.7 \mu\text{s}$ to take one collect at a range of 1000 meters, 200 collects would only require 1.3 ms which is a reasonable amount of time. The assumption that the 200 collects consist of exactly the



(a)



(b)

Figure 2.2: (a) This figure shows the negative binomial PMF for increasing values of the speckle parameter at a mean photon count of $\bar{K} = 50$. As M increases, the probability gets more Poisson-like with the main hump centered on the mean photon count.
 (b) This figure shows the negative binomial PMF at a speckle parameter of $M = 200$ and a mean photon count of $\bar{K} = 50$ compared with the Poisson PMF with the same mean.

same scene is more troublesome. If an airborne platform is targeting in the direction of its velocity, then the consistent scene could be realized (if the target isn't moving either). However, as the laser firing direction shifts to either side, the scenes are most likely rapidly changing due to typical airborne platform speeds. A mitigation to the changing scenes is to use available 3D image registration algorithms. With respect to averaging, Bayesian estimation attempts have been made to mitigate the shifts between cubes for a particular pixel using partial coherent light [63]. Since the 3D FLASH LADAR used in this research mounts on a tripod and can easily obtain 200 or more collects of a scene, the LADAR *can* be used to collect data with the approximation of incoherent object illumination.

The second method to ascertain if the speckle parameter is large enough is from direct calculation. From [24], the overall speckle parameter M can be defined as

$$M = M_s M_t \quad (2.30)$$

where M_s and M_t are the spatial and temporal degrees of freedom respectively. Given the operating configuration, the area of the detector A_d is smaller than the coherence area A_c resulting in $M_s = 1$ [24]. The area of the detector is $A_d = (100 \mu\text{m})^2 = 10 \text{ nm}^2$ while the coherence area A_c is defined by the amount of coherence present in the light given by [24]

$$A_c = \int_{-\infty}^{\infty} \int_{-\infty}^{\infty} |\mu(\Delta x, \Delta y)|^2 d\Delta x d\Delta y \quad (2.31)$$

with $\mu(\Delta x, \Delta y)$ as the complex coherence factor that provides a measure of the amount of coherence between two points and $(\Delta x, \Delta y)$ are the difference in coordinates between two points in the observation plane. In the imaging case, it is shown that for any incoherent source that

$$A_c = \frac{(\lambda f)^2}{A_s} \quad (2.32)$$

with λ as the mean wavelength, f as the focal length, and A_s as the area of the incoherent light source. For a circular aperture, the area of the light source is $A_s = \pi r^2$. Thus, the

coherence area becomes

$$A_c = \frac{((1.55 \mu\text{m}) (0.3 \text{ m}))^2}{\pi(1 \text{ mm})^2} = 69 \text{ nm}^2 \quad (2.33)$$

and it can be seen that $M_s = 1$ due to $A_d < A_c$ or $10 \text{ nm}^2 < 69 \text{ nm}^2$. The other part of the overall speckle parameter is the temporal degree of freedom M_t which is defined for a light beam with a rectangular power spectral density by [24]

$$M_t = \frac{\Delta}{\tau_c} = \frac{\Delta}{1/\Delta v} \quad (2.34)$$

where Δ is the pixel integration time, τ_c is the coherence time, and Δv is the bandwidth of the laser light. The mean frequency of the laser light $\bar{\nu}$ is

$$\bar{\nu} = \frac{c}{\lambda} = \frac{3 \times 10^8 \text{ m/s}}{1.55 \mu\text{m}} = 194 \text{ THz} \quad (2.35)$$

and assuming a bandwidth of $\pm 0.05 \mu\text{m}$ gives a frequency bandwidth $\Delta v = 12.5 \text{ THz}$. Considering an integration time $\Delta = 1 \text{ ns}$, the resulting temporal degrees of freedom M_t is

$$M_t = \frac{\Delta}{1/\Delta v} = \frac{1 \text{ ns}}{1/12.5 \text{ THz}} = 12500. \quad (2.36)$$

Consequently, the overall speckle parameter is $M = 12500$ which is most likely high enough to assume incoherent imaging by considering the Poisson distribution a valid approximation for the negative binomial distribution. This assumption would probably still be valid even if Δv or M_t is reduced by several orders of magnitude.

2.2 Deconvolution

With the optical system able to be represented by a linear system, the attention turns to the main topic area in this research: range estimation from object retrieval from data observations of a 3D FLASH LADAR. The system is modeled by a linear system characterized by an impulse response. The observed data is modeled as being generated from a

convolution between the object and impulse response corrupted by noise. For this research, the object primarily consists of recorded amplitudes and range location of the target under interrogation by the 3D FLASH LADAR. In order to retrieve the object, the effects of the convolution and noise must be reversed. In other words, one must deconvolve the object from the impulse response while minimizing noise effects. As such, a review of standard deconvolution theory is warranted. The chosen model in this research is in units of detected photons per second while the image intensity has only been defined thus far. If I_D denotes the intensity at the detector (watts/m²), then the following conversion results in detected photons per second, or mean photon flux: [30]

$$\Phi = \frac{AI_D}{hf} \quad (2.37)$$

where A is the cross-sectional area of the incident light, h is Planck's constant (6.626×10^{-34} Joules · sec), and f is the light's frequency. Substituting Equation (2.25) into Equation (2.37) gives the photons per second at (u, v) in the detector plane as

$$\Phi(u, v) = \frac{A}{hf} \kappa \int_{-\infty}^{\infty} \int_{-\infty}^{\infty} |h(u - \xi, v - \eta)|^2 I_g(\xi, \eta) d\xi d\eta \quad (2.38)$$

where the units would be congruent to the mathematical model for the returned signal presented in the future sections.

In physical measurements, noise mitigation and an unknown system impulse response make the problem more difficult. The system impulse response may not be known in most operational ranging or imaging applications. Thus, the process of object retrieval is termed blind deconvolution due to the unknown system impulse response. In this case, estimates of the impulse response need to be calculated along with the object estimates.

2.2.1 Inverse Filtering. If there is no noise term and the system impulse response is known, the deconvolution can be performed easily in the spatial frequency domain. Note that the previous convention concerning image and object planes changes from (u, v) and

(ξ, η) to (x, y) and (m, n) respectively. Taking the 2D Fourier transform of noiseless observations from a 3D FLASH LADAR, $d_k(x, y)$ in the (x, y) spatial dimensions (k is the time dimension) results in

$$D_k(f_x, f_y) = O_k(f_x, f_y)H(f_x, f_y) \quad (2.39)$$

where $O_k(f_x, f_y)$ and $H(f_x, f_y)$ are the Fourier Transform of the object and the system impulse response respectively. The object can be retrieved by setting the filter, G , as the inverse of the Fourier Transform of the point spread function

$$\begin{aligned} o_k(m, n) &= \mathfrak{F}^{-1} \{ D_k(f_x, f_y) G(f_x, f_y) \} \\ &= \mathfrak{F}^{-1} \left\{ \frac{D_k(f_x, f_y)}{H(f_x, f_y)} \right\} \\ &= \mathfrak{F}^{-1} \left\{ \frac{O_k(f_x, f_y) H(f_x, f_y)}{H(f_x, f_y)} \right\} \\ &= \mathfrak{F}^{-1} \{ O_k(f_x, f_y) \}. \end{aligned} \quad (2.40)$$

Conversely, the following highlights the severe limitation of inverse filtering when random noise effects are introduced:

$$\begin{aligned} \hat{o}_k(m, n) &= \mathfrak{F}^{-1} \left\{ \frac{D_k(f_x, f_y)}{H(f_x, f_y)} \right\} \\ &= \mathfrak{F}^{-1} \left\{ \frac{O_k(f_x, f_y)H(f_x, f_y) + N_k(f_x, f_y)}{H(f_x, f_y)} \right\} \\ &= \mathfrak{F}^{-1} \left\{ O_k(f_x, f_y) + \frac{N_k(f_x, f_y)}{H(f_x, f_y)} \right\}. \end{aligned} \quad (2.41)$$

$$(2.42)$$

The inverse filter solution will be skewed to the degree that the impulse response amplifies the noise term which can be significant. This noise amplification is a primary driver towards other solutions based on minimizing the effects of noise.

According to [37], the Wiener filter minimizes the mean squared error between the real object and the estimated object, $E[(o - \hat{o})^2]$, resulting in the following functional form

$$G(f_x, f_y) = \frac{H^*(f_x, f_y)}{|H(f_x, f_y)|^2 + S_{nn}(f_x, f_y)/S_{ii}(f_x, f_y)} \quad (2.43)$$

where $*$ is the conjugate operator and S_{nn} and S_{ii} are the power spectra of the noise and signal respectively. The resulting estimate for the object is

$$\begin{aligned} \hat{o}_k(m, n) &= \mathfrak{F}^{-1} \left\{ \frac{D_k(f_x, f_y) H^*(f_x, f_y)}{|H(f_x, f_y)|^2 + S_{nn}(f_x, f_y)/S_{ii}(f_x, f_y)} \right\} \\ &= \mathfrak{F}^{-1} \left\{ \frac{[O_k(f_x, f_y) H(f_x, f_y) + N_k(f_x, f_y)] H^*(f_x, f_y)}{|H(f_x, f_y)|^2 + S_{nn}(f_x, f_y)/S_{ii}(f_x, f_y)} \right\} \\ &= \mathfrak{F}^{-1} \left\{ \frac{[O_k(f_x, f_y) |H(f_x, f_y)|^2 + N_k(f_x, f_y) H^*(f_x, f_y)]}{|H(f_x, f_y)|^2 + S_{nn}(f_x, f_y)/S_{ii}(f_x, f_y)} \right\} \end{aligned} \quad (2.44)$$

Examining this final form is enlightening to how the filter handles certain noise situations. When the noise spectrum is zero or dominated by signal, the filter simplifies to the inverse filter. When the noise power is severe or the signal level is low at some frequencies, the filter approaches zero attenuating these frequencies with high noise power.

2.2.2 Iterative Algorithms. Iterative deconvolution techniques also exist to include the Richardson-Lucy and error minimization algorithms which are useful when data models are complex or non-linear. From [62], the Richardson-Lucy algorithm was developed to be an approximate deconvolution to recover the object W from the degraded noiseless image $H = W \otimes S$ with \otimes as the convolution operator and S as the point spread function. Temporarily adopting notation from [62], the problem is constructed based on Bayes theorem given by [60]

$$P(W_j|H_q) = \frac{P(H_q|W_j) P(W_j)}{\sum_i P(H_q|W_i) P(W_i)} \quad (2.45)$$

where $P(W|H)$ is the conditional probability of W given H (also called the *a posteriori* density), $P(H|W)$ is the conditional probability of H given W , $P(W)$ is the marginal probability of W (also called the *a priori* density), and $P(H)$ is the marginal probability of H . The subscripts j and q correspond to pixel locations with $W = \sum_j W_j$ and $H = \sum_q H_q$ equalling the value for the entire object and degraded image arrays respectively. The prior probability can be defined by [60]

$$P(W_j) = \sum_z P(W_j|H_z) P(H_z) \quad (2.46)$$

and by combining Equations (2.45) and (2.46) results in the following equation [62]

$$P(W_j) = \sum_z \frac{P(H_z|W_j) P(W_j) P(H_z)}{\sum_i P(H_z|W_i) P(W_i)}. \quad (2.47)$$

Noting that the desired solution, $P(W_j)$, is also on the right-hand-side of the equation and is not a function of the summation, a common practice is to make an initial guess and set up the iterative updates as

$$P_{r+1}(W_j) = P_r(W_j) \sum_z \frac{P(H_z|W_j) P(H_z)}{\sum_i P(H_z|W_i) P(W_i)}. \quad (2.48)$$

Reduction of Equation (2.48) is still necessary due to being in terms of probability. This equation is changed so that it uses actual variable values rather than probability. Using the laws of probability and the conservation of energy, the probabilities can be reformed into

$$\begin{aligned} P(W_j) &= W_j/W, \\ P(H_q) &= H_q/H = H_q/W, \\ \text{and } P(H_q|W_j) &= P(S_{j,q}) = S_{j,q}/S. \end{aligned} \quad (2.49)$$

Consequently, Equation (2.48) can be reduced to

$$W_{j,r+1} = W_{j,r} \sum_z \frac{S_{j,z} H_z}{\sum_i S_{i,z} W_{i,r}} \quad (2.50)$$

which represents the final form of the Richardson-Lucy object recovery algorithm. One weakness of this algorithm is its lack of proven convergence. In practice, however, the iterations provide the perfect solution in the noiseless case and an improved solution with noisy data.

From [8], the last reviewed method of deconvolution involves using a cost function and minimizing it with respect to the data and the true image. The cost function is defined by

$$C = \sum_{x=1}^M \sum_{y=1}^N (d(x, y) - i(x, y))^2 \quad (2.51)$$

where the data equals $d(x, y) = i(x, y) + n(x, y)$ where $n(x, y)$ is the signal independent, additive noise and the true image is defined as

$$i(x, y) = \sum_{m=1}^M \sum_{n=1}^N o(m, n) h(x - m, y - n) \quad (2.52)$$

with $o(m, n)$ as the object and $h(m, n)$ as the point spread function. In order to minimize the cost with respect to the unknown, the derivative of the cost function is taken with respect to the object with the result set to zero. The solution is obtained by solving this equation for the object. Thus, the derivative of Equation (2.51) is taken with respect to a single object pixel (m_o, n_o) and set to zero

$$\frac{\partial C}{\partial o(m_o, n_o)} = -2 \sum_{x=1}^M \sum_{y=1}^N (d(x, y) - i(x, y)) \frac{\partial i(x, y)}{\partial o(m_o, n_o)} = 0. \quad (2.53)$$

The partial derivative of the image is

$$\begin{aligned}\frac{\partial i(x, y)}{\partial o(m_o, n_o)} &= \frac{\partial}{\partial o(m_o, n_o)} [o(m_o, n_o) h(x - m_o, y - n_o)] \\ &= h(x - m_o, y - n_o)\end{aligned}\quad (2.54)$$

giving the resulting expression and reduction

$$\begin{aligned}\sum_{x=1}^M \sum_{y=1}^N (d(x, y) - i(x, y))h(x - m_o, y - n_o) &= 0 \\ \frac{\sum_{x=1}^M \sum_{y=1}^N d(x, y)h(x - m_o, y - n_o)}{\sum_{x=1}^M \sum_{y=1}^N i(x, y)h(x - m_o, y - n_o)} &= 1.\end{aligned}\quad (2.55)$$

Using reasoning similar to [62], the object is then multiplied on both sides of Equation (2.55) giving the final form of the object recovery as

$$o^{new}(m_o, n_o) = o^{old}(m_o, n_o) \frac{\sum_{x=1}^M \sum_{y=1}^N d(x, y)h(x - m_o, y - n_o)}{\sum_{x=1}^M \sum_{y=1}^N i^{old}(x, y)h(x - m_o, y - n_o)} \quad (2.56)$$

with $i^{old}(x, y) = \sum_{m=1}^M \sum_{n=1}^N o^{old}(m, n) h(x - m, y - n)$. An acceptable stopping point can be (1) minimal change from the previous iteration or (2) the appropriate amount of image noise in the estimated image based on prior knowledge of the noise source.

2.3 Maximum Likelihood

Maximum Likelihood (ML) estimation can be used for a data model that includes no blurring function because the model then implicitly assumes no coupling between pixels. The ML method can then operate on one pixel at a time. Another means of estimating parameters (e.g. object, received amplitude, range to target) is to employ ML estimation using the observation statistics to form a likelihood expression. From [84], the ML solution

is the outcome of a ML analysis where the estimate, \hat{a} , maximizes the likelihood function, $L(A)$, or

$$\hat{a} = \arg \max_A L(A) \quad (2.57)$$

where the parameter A can either be a single or vector variable. Considerations of maximum likelihood estimation include the uncertainty that a unique ML solution exists and local maximums in the likelihood function.

One way to view the ML solution is as a special case of Maximum a Posterior (MAP) estimation with the prior distribution being a uniform distribution. MAP estimation is Bayesian based and starts with Bayes Theorem. Recall that Bayes Theorem relates the conditional and marginal probabilities of events A and B with B having a non-zero probability. The equation for Bayes Theorem is defined again as [60]

$$P_{a|b}(A|B) = \frac{P_{b|a}(B|A)P_a(A)}{P_b(B)} \quad (2.58)$$

where $P(A|B)$ is the conditional probability of A given B (also called the *a posteriori* density), $P(B|A)$ is the conditional probability of B given A , $P(A)$ is the marginal probability of A (also called the *a priori* density), and $P(B)$ is the marginal probability of B . Bayes theorem calculates the probability of event A occurring given observing B . Maximizing Equation (2.58) is mathematically equivalent to maximizing the natural log resulting in

$$\ln[p_{a|b}(A|B)] = \ln p_{b|a}(B|A) + \ln p_a(A) - \ln p_B(B). \quad (2.59)$$

The MAP estimate is found by taking the derivative of Equation (2.59), setting it equal to zero, solving for A given by

$$\frac{\partial \ln(p(A|B))}{\partial A} = \frac{\partial \ln(p(B|A))}{\partial A} + \frac{\partial \ln(p(A))}{\partial A} - \frac{\partial \ln(p(B))}{\partial A} = 0 \quad (2.60)$$

where $\frac{\partial \ln(p(B))}{\partial A} = 0$ due to no dependence on A . The final form of the MAP estimator is then

$$\hat{a}_{map} = \arg \max_A (\ln p_{b|a}(B|A) + \ln p_a(A)). \quad (2.61)$$

When the prior probability $p_a(A)$ is unavailable or not postulated, it can be assumed that the prior probability can be described as a uniform RV. Thus, $p_a(A)$ has no dependence on A either and

$$\frac{\partial \ln(p(A))}{\partial A} = 0 \quad (2.62)$$

resulting in the ML solution of

$$\hat{a}_{map} = \arg \max_A (\ln p(B|A)). \quad (2.63)$$

A maximum likelihood technique is used for single pixel range estimation in Section 4.2.

2.4 Generalized Expectation Maximization

Traditional linear maximum likelihood efforts do not suffice to estimate target range given the unknowns (amplitude, target range, PSF, and pixel bias) in the statistical model from Equation (2.69). More powerful object estimation methods like the Generalized Expectation Maximization (GEM) algorithm must be employed due to the coupled unknowns which will be covered in the next section. While the final goal is to estimate range, a different tactic is employed due to the difficulty in having the target range term residing in the exponential. Consequently, the unknowns in the estimation process are the target amplitude, target *pulse shape* (or *object*), and PSF. With the pulse shape now as an unknown, it is much simpler to use the GEM to find maximum likelihood solutions. Once the maximum likelihood solution for the object or pulse shape is found, a correlation operation between the estimated pulse shape and a reference pulse shape determines the estimated target range. A full description of the algorithm will be given in the subsequent paragraphs. First, the GEM solutions for the unknown parameters must be found. However, a closed form solution for the EM algorithm's maximization step is intractable. Consequently, the

GEM algorithm goal is to modify the EM structure such that the likelihood is incrementally increased rather than globally maximized as in the EM algorithm. This incremental increase in the likelihood simplifies the maximization step allowing unknown, non-random parameter estimation.

In the case of blind deconvolution, the EM algorithm can be implemented to estimate the object, point spread function, range, and/or amplitude. This algorithm is another method to perform maximum likelihood estimation whereby the solution is found by using unobserved data (complete) rather than the observed data (incomplete). Although, the maximum likelihood solution is not always guaranteed as a result from the EM algorithm. Pertaining to the unobserved data, it may be necessary because the regular maximum likelihood solution may be analytically prohibitive. The EM algorithm uses the reduced complexity of the complete data problem to perform maximum likelihood estimation.

According to [54], the EM algorithm is composed of two steps. The first step (E-Step) is to find Q : the expected value of the desired variable given the latest parameter values or

$$Q(\Psi; \Psi^{(k)}) = E_{\Psi^{(k)}} \{ \ln L_{CD}(\Psi) | y \} \quad (2.64)$$

where Ψ is the vector of unknown parameters, k is the iteration, $L_{CD}(\Psi)$ is the complete data likelihood, and the expectation conditioned on the incomplete data y . Complete data can be viewed as the unobserved variables (fabricated or not) used to simplify the problem. Incomplete data is usually the observed data. The second step (M-Step) is to maximize this expected value with respect to the unknown parameters, Ψ , by choosing Ψ^{k+1} to maximize $Q(\Psi; \Psi^{(k)})$ or

$$Q(\Psi^{(k+1)}; \Psi^{(k)}) \geq Q(\Psi; \Psi^{(k)}) . \quad (2.65)$$

for all unknown parameters in Ψ . The EM algorithm is advantageous due to the guarantee of increasing the likelihood with each iteration and, in most cases, eventually converging on the maximum likelihood solution. As proven by [16], the incomplete-data log-likelihood

function increases with each iteration

$$L(\Psi^{(k+1)}) \geq L(\Psi^{(k)}) \quad (2.66)$$

and the EM algorithm converges to local or global maximum.

As is the case in this research where the maximization over all unknown parameters is difficult or doesn't exist in a closed form, an incremental EM algorithm is used called the generalized expectation maximization (GEM) where the goal is to simply increase the likelihood at each iteration without finding the maximum parameter value. A GEM requires that the likelihood be improved and not maximized such that

$$Q(\Psi^{(k+1)}; \Psi^{(k)}) \geq Q(\Psi^{(k)}; \Psi^{(k)}). \quad (2.67)$$

If Equation (2.67) holds for every iteration, it has been shown that the likelihood is increased with every iteration or [54]

$$L(\Psi^{(k+1)}) \geq L(\Psi^{(k)}) \quad (2.68)$$

and, if bounded, the GEM sequence converges to a local maximum due to the monotonicity of the algorithm. The GEM algorithm will be implemented on simulated and experimental data in Chapter V to show that object recovery improves range estimation.

2.5 3D FLASH LADAR Data Model

This section describes the physical 3D FLASH LADAR model. To increase readability, the model is defined in this chapter due to parts of Chapter IV and all of Chapter V using this particular model. (Other sections in Chapter IV and all of Chapter VI use a different, simplified observation model to allow for relatively uncomplicated mathematical expressions and for concept investigation. The changes in model definition are clearly identified.)

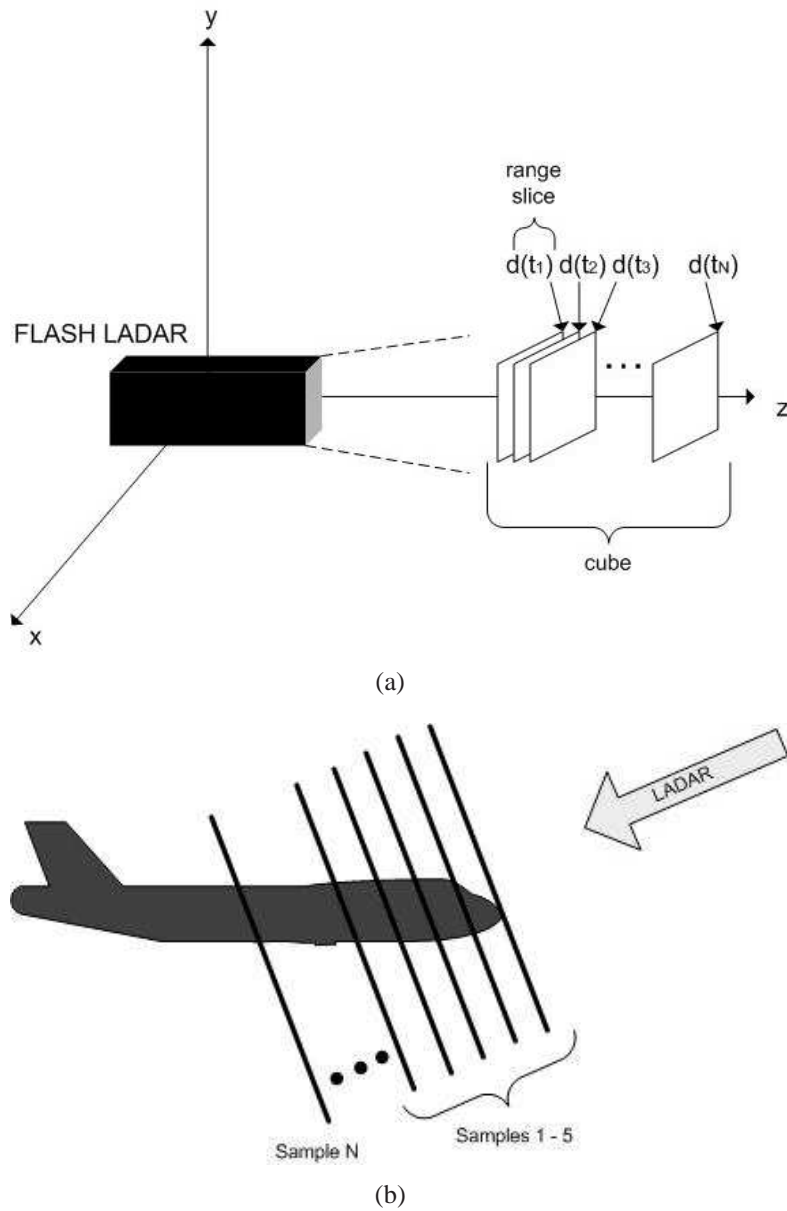


Figure 2.3: (a) 3D view of LADAR system model in Cartesian coordinates with each data cube having dimensions of $30 \times 30 \times 20$ corresponding to pixel \times pixel \times time sample. The variable $d(t_k)$ corresponds to the k^{th} receiver detected range slice image with $k \in [1, \dots, N]$ and $N = 20$. (b) Another view of the 3D FLASH LADAR operation. The N number of samples are meant to depict the available target information that the 2D range images (slices) would collect. The assumed time separation between the range images is 2 nanoseconds closely corresponding to the 3D LADAR system used for experimental collects.

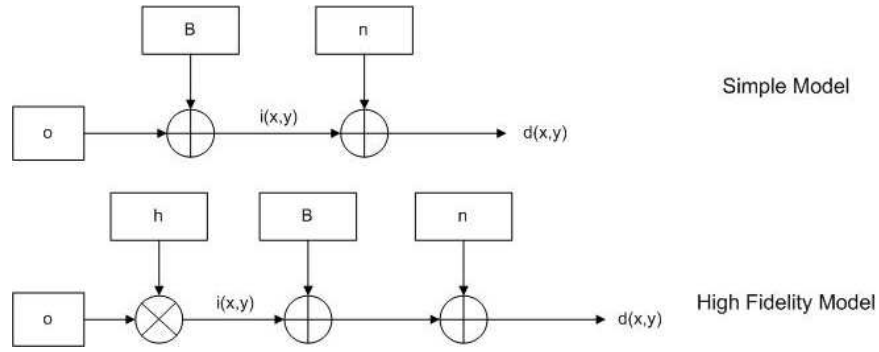


Figure 2.4: For a given range slice, this diagram shows the propagation of the object through optical system to the observation. Definitions: o is the object, h is the PSF, B is the pixel bias, n is the noise, and d is the observation. The simple signal model is used in previous 3D FLASH LADAR research such as [9], [39], and [55]. The high fidelity model is used in Chapters V and VI.

Figure 2.3 shows the sensor operation resulting in a data cube of spatial and range information. In simple terms, the LADAR laser transmits a pulse and the LADAR detector array receives an attenuated, time-delayed version of the transmitted pulse. Each detector receives a version of the waveform shape sampled according to the range gate. Thus, models can take advantage of this fact and perform range estimation on a per pixel basis. Referring to Figure 2.4, previous research has assumed the simple model [9], [39] where the spatial impulse response was a Dirac delta function. This definition meant there were no interactions between adjacent pixels. However, the research in this dissertation adopts the high fidelity model since it is more accurate concerning pixel spatial interactions. The limitation of the simplistic model and adaptation of the higher fidelity model is the catalyst of the material in Chapters V and VI.

In order to simplify the geometry and the mathematics, assumptions are made about the model to include: (i) target is perpendicular to the transmitter, (ii) target is in the far-field of the receiver, (iii) target is Lambertian, (iv) circular optics are in-focus, (v) monostatic RADAR operation, (vi) the waveform is a symmetric Gaussian pulse, (vii) each pixel from the detector array has an individual waveform associated with it, and (viii) the range slices of the data cube are registered. Other pulse shape models are available include an asymmetric Gaussian, a truncated negative parabolic, or some hybrid of a Gaussian and negative

parabolic. A symmetric Gaussian is chosen for notation purposes, but an asymmetric version is easily defined with different pulse-widths for the leading and trailing edges.

Considering a 3D FLASH LADAR sensor with statistically independent samples dominated by shot-noise [9], [39], the PMF of the observed photons, $d_{jk}(x, y)$, incorporating all cubes ($j \in [1, \dots, J]$), range samples ($k \in [1, \dots, K]$), and detector pixels ($x \in [1, \dots, X], y \in [1, \dots, Y]$) is

$$P [D_{jk}(x, y) = d_{jk}(x, y); \forall j, k, x, y] = \prod_{j,k,x,y} \frac{[i_{jk}(x, y) + B(x, y)]^{d_{jk}(x,y)} \exp\{-[i_{jk}(x, y) + B(x, y)]\}}{d_{jk}(x, y)!} \quad (2.69)$$

where the mean signal is $i_{jk}(x, y) + B(x, y)$ where $B(x, y)$ is the pixel bias and the blurry, non-noisy signal $i_{jk}(x, y)$ is defined by

$$i_{jk}(x, y) = \sum_{m=1}^M \sum_{n=1}^N o_k(m, n) h_j(x - m, y - n) \quad (2.70)$$

where the object $o_k(m, n)$ is defined at the object plane with coordinates ($m \in [1, \dots, M]$ and $n \in [1, \dots, N]$). The (x, y) and k variables correspond to a pixel in the detector array and to the returned signal time of arrival respectively. The time of arrival is computed based on the time from laser pulse transmission to photon detection. This assumption may require cube registration due to the possibility of moving targets, moving sensor platform, or inter-cube timing errors. Incorporating contributions from light propagation, optical aberrations, and atmospheric blurring, the intensity point spread function (PSF) $h_j(x, y)$ is constant within a single cube while changing across cubes. In this research, the PSF is considered constant within a single cube since collection times spans under forty nanoseconds and any time-dependent effects would be essentially frozen. In addition, the pixel bias $B(x, y)$ is constant between cubes as well as within a single cube due to the pixel's unchanging physical material and response to incident light (ambient radiation is assumed negligible).

Every pixel in the detector array records a time-delayed and attenuated version of the transmitted pulse. The physical outgoing pulse shape of a 3D FLASH LADAR is either

Gaussian, negative parabolic, or some hybrid of the two. The object can be defined by an amplitude term and a pulse shape or

$$o_k(m, n) = A(m, n) p_k(m, n). \quad (2.71)$$

Assuming a Gaussian transmitted pulse, the object is

$$o_k(m, n) = \frac{A(m, n)}{\sqrt{2\pi}\sigma_w} \exp\left\{-\frac{(t_k - 2R(m, n)/c)^2}{2\sigma_w^2}\right\} \quad (2.72)$$

where $A(m, n)$ is the object amplitude, σ_w is the waveform standard deviation, t_k is the time variable, c is the speed of light, and $R(m, n)$ is the range to the target. If a negative parabolic waveform model is desired, the object is defined by

$$o_k(m, n) = A(m, n) \left[1 - \frac{(2R(m, n) - t_k c)^2}{(cp_w)^2}\right] \text{rect}\left(\frac{2R(m, n) - t_k c}{2cp_w}\right) \quad (2.73)$$

where $2p_w$ is the pulse width and rect is the rectangle function defined by

$$\text{rect}(x) = \begin{cases} 0, & \text{if } |x| > 1/2 \\ 1/2, & \text{if } |x| = 1/2 \\ 1, & \text{if } |x| < 1/2. \end{cases} \quad (2.74)$$

Although, for simplicity and ease of differentiation, this research adopts the Gaussian model. For military targeting or navigation, range to target (located in the object term) is the desired unknown variable. In attempting to perform range estimation, a range term is not explicitly in the model, but it is buried within the object, $o_k(m, n)$, term given by Equation (2.72) or (2.73). If the object were exactly known, the target range could be then extracted from the object by peak detection methods. This statement presents the ideal situation that Chapter V attempts to create with an object degraded by spatial blurring and noise sources.

Given the LADAR's 3D nature, it is important to discern the formation of range slice images shown in Figure 2.3 versus the pixel waveform definition from (2.72). The range slice images are formed at a particular time by a spatial convolution between the original scene and the system's impulse response. The original scene's amplitude is variable at each time instant due to target roughness and Gaussian shaped transmitted pulse. Therefore, the returned amplitude changes for each range image formation operation. Considering atmospheric turbulence, the system's impulse response is assumed constant for each $[1, N]$ range image due to the short duration of the data cube collection (forty nanoseconds) [24]. Conversely, the pixel waveform definitions from Equation (2.72) define each pixel's un-blurred and non-noisy received signal where the model assumes only one target per pixel. The range estimation process estimates the target's range for every pixel. The following is a concise explanation of the difference between data generation and range estimation: the simulation forms 3D LADAR data cubes in the spatial domain while the range estimator operates in the range (time) domain. Also, as will be discussed later, image deblurring operates spatially like the image formation process.

Following [25], a transfer function describes the LADAR's effect on the target return assuming the system is linear and spatially invariant. The transfer function in optics is called an optical transfer function (OTF). If only considering the effects of the optical components, the OTF is diffraction-limited because the only way to increase performance would be to build better optical components. Otherwise, optical diffraction theory bounds the system performance.

While not the main focus of this research, it is important to understand that 3D FLASH LADAR operational use may encounter periods of considerable atmospheric turbulence that would modify the system OTF. As long as the imaging scenario stays within the isoplanatic angle, the PSF can still be considered spatially invariant which is a prerequisite to this deblurring technique [51]. Given this condition holds true, the OTF is then a function of the diffraction-limited OTF and the average OTF resulting from the atmosphere. Considering a substantial target distance, there could be atmospheric distortion and would manifest itself by modifying the diffraction-limited OTF to form an overall OTF [24]. Ne-

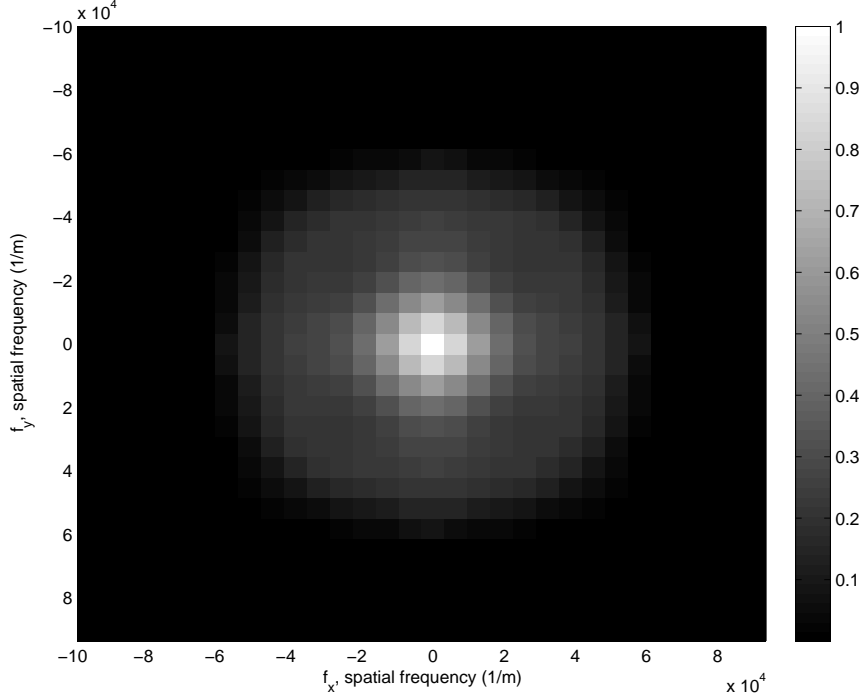


Figure 2.5: An example of a diffraction limited OTF. This OTF was generated using the parameters from this research.

glecting pixel integration effects, the form of the overall OTF, $H(f_x, f_y)$, could be

$$H(f_x, f_y) = H_o(f_x, f_y)\bar{H}_A(f_x, f_y) \quad (2.75)$$

where (f_x, f_y) are spatial frequency variables, $H_o(f_x, f_y)$ is the diffraction-limited OTF, and $\bar{H}_A(f_x, f_y)$ is the short-exposure average OTF due to atmospheric turbulence. The form of \bar{H}_A is [24] [67]

$$\bar{H}_A(\nu) = \exp \left\{ -3.44 \left(\frac{\bar{\lambda} f \nu}{r_o} \right)^{5/3} \left[1 - \left(\frac{\bar{\lambda} f \nu}{D} \right)^{1/3} \right] \right\} \quad (2.76)$$

with $\nu = \sqrt{f_x^2 + f_y^2}$, $\bar{\lambda}$ the mean wavelength, f the optic's focal length, r_o as the atmospheric coherence diameter or Fried's seeing parameter, and D is the aperture diameter.

With the OTF defined as the inverse Fourier Transform of the PSF, Figure 2.5 shows a two-dimensional representation of the simulation's diffraction-limited OTF. Using centered 1D cutouts, Figure 2.6 shows the effect of the atmosphere on the OTF whereby the atmosphere

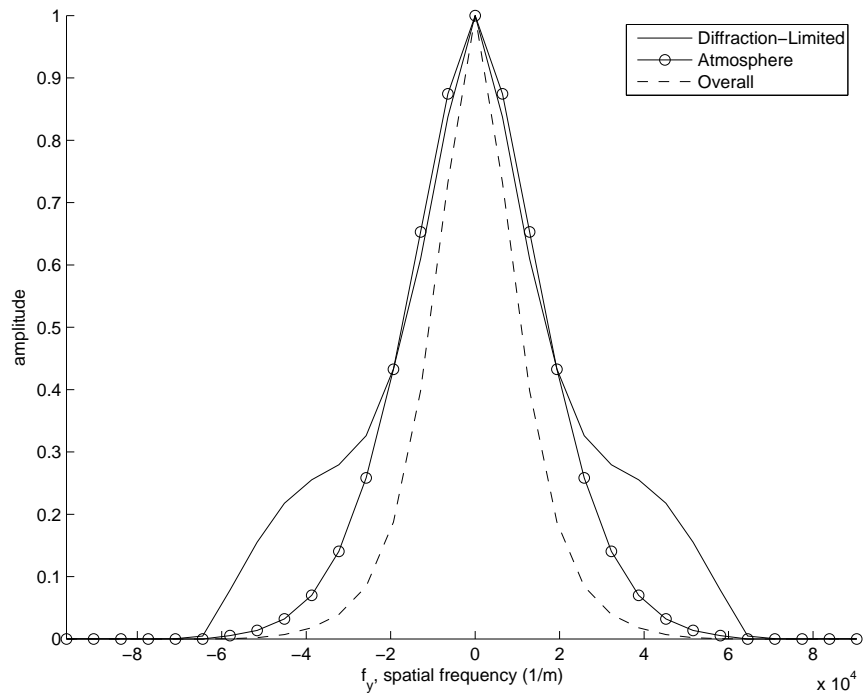


Figure 2.6: Cut-outs, $(0, f_y)$, of different OTFs to include diffraction-limited, atmosphere, and overall. The degradation in the overall OTF caused by the atmosphere is evident with higher spatial frequencies blocked.

degrades the overall OTF by narrowing the amount of spatial frequencies the system can pass. This truncation of spatial frequencies causes high frequency details in the range slice image (i.e. sharp corners, fine lines, etc.) to be lost. The narrowing of the OTF in the spatial frequency domain leads to a widening of the PSF in the spatial domain. This widening causes increased pixel mixing due to the convolution nature of the system. The resulting received waveform is further deviated from the idealized received waveform in (2.72). Blind deconvolution methods in Chapter V would effectively estimate any additional atmospheric blurring as long as the mode of operation remained in the isoplanatic angle (i.e. spatially invariant) [25].

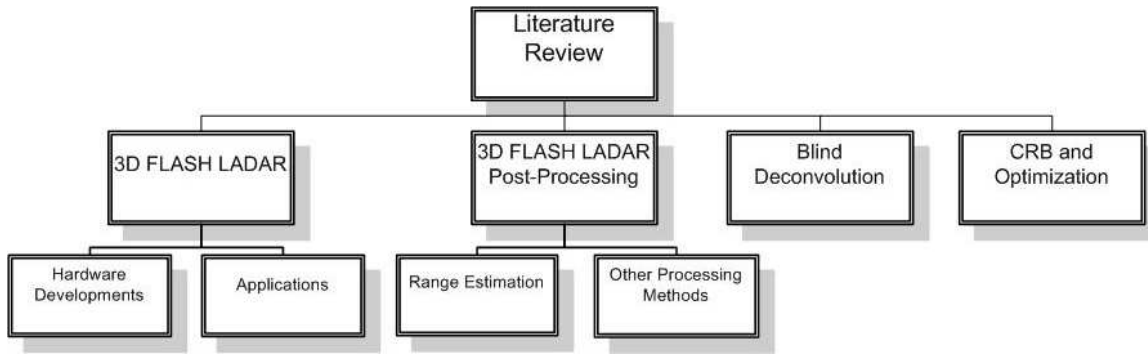


Figure 2.7: Organizational chart for the literature review. The review is broken down into the following sections: 3D FLASH LADAR Hardware and Applications - Section 2.6.1. 3D FLASH LADAR Post-Processing - Section 2.6.2. Blind Deconvolution - Section 2.6.3. CRB and Parameter Optimization - Section 2.6.4.

2.6 Previous Research

This section contains the literature review of publications relating to hardware development and post-processing of 3D FLASH LADAR data. The background review provides a treatment of several important topics: 3D FLASH LADAR hardware development and applications, 3D LADAR post-processing algorithms, LADAR range estimation, general blind deconvolution theory and applications, lucky imaging, and 3-D image registration. Seminal papers are reviewed as well as appropriate recent publications. For easy reference, Figure 2.7 shows the literature review organization.

LADAR theoretical development in the past 10–20 years has concentrated on 3D scanning LADAR systems almost exclusively because it was the only 3D LADAR available. 3D FLASH LADARs are a relatively new development, explaining the lack of publications compared to more mature technologies. The current 3D FLASH LADAR literature spans from hardware development to applications to post-processing. The post-processing papers consider important algorithms enabling improved range estimation, feature extraction, foliage penetration, world modeling, mapping, and navigational aiding.

The papers that do take advantage of the unique properties of a 3D FLASH system use a simplified data model. The spatial convolution nature between the object plane intensity and the detector plane intensity is not accounted for, leading to errors in parameter

estimation. There is a gap in the literature considering the spatial effects of a 3D LADAR system because the scanning systems simply don't see the effects of the spatial impulse response. Scanning LADARs don't operate fast enough spatially or have a wide enough field-of-view (FOV) to observe the blurring effects of the spatial impulse response like the FLASH systems do.

2.6.1 3D FLASH LADAR.

2.6.1.1 Hardware Developments. Although new advances LADAR hardware development is not the focus of this research, it is prudent to know about not only the hardware used in this research, but also other state-of-the-art 3D LADARs. Understanding where the technology stands and some of the details will lend an appreciation for the uniqueness and potential of the 3D FLASH LADARs. The advances made in the LADAR hardware have increased capability, but have created additional issues that need mitigation.

Based on work from [64], [65], and [66], the enabling technology allowing 3D FLASH LADAR to be realized culminated in 2004 with the development of a focal plane array (FPA) capable of collecting a series of two dimensional (2D) images of a remote scene at varying depths from a single laser pulse [81]. The modelling in this research is based on this hardware. Additionally, this particular 3D FLASH LADAR system will be used for experimental data collection in the future. The novel hardware design using detector material made of either InGaAs PIN or Avalanche Photodiodes (APD), along with the data acquisition board called the Readout Integrated Circuit (ROIC), allows for rapid data collection in the range dimension with each pixel able to digitally sample the returned waveform. The ROIC permits this rapid range sampling with a bank of capacitors behind each pixel capable of operating on the nanosecond scale. Of note, a similar LADAR developed with the same goals is summarized in [29]. The only noticeable difference in this LADAR was that it uses HgCdTe APD detector technology exclusively.

The FLASH LADAR is considered an improvement over scanning LADARs when considering all the scene's information is collected in one shot and that there is no need for

pixel registration. Additionally, the 3D FLASH LADAR is “eye-safe” because it operates in the short wave infrared (SWIR) regime (beyond 1.4 microns). It has been shown that the selected detector materials perform well at this wavelength with respect to both quantum efficiency and electrical bandwidth. Also, there are substantial cost and weight savings given that a mechanical steering mechanism is not needed like in the scanning systems.

While there are obvious benefits, there are several drawbacks to the system that need addressing in future hardware upgrades. There are a limited number of range samples available for each transmitted signal. Essentially, there is a limit to the time the “shutter” can be open. In one operating mode, this limits the operator to know where the target is *a priori* to within several meters. This limitation is not an issue in the laboratory, but will need to be addressed for operational use either in hardware upgrades that solve the problem or by CONOPS (Concept of Operations). For example, another sensor could roughly locate the target and pass that rough location to the 3D FLASH LADAR to fine tune the range measurements. Another issue mitigated in [73] is pixel coupling occurring throughout the detector array caused by a time-dependent gain variation. Finally, as mentioned before, spatial impulse response effects are now evident in the data and are the primary focus of this prospectus.

Advances in technology like the AFRL 3D FLASH LADAR are an example of hardware improvements opening up fields of research not otherwise considered. Evolving technology from scanning to FLASH LADARs will vastly increase operational capabilities and pave the way for future applications.

Other efforts to produce 3D FLASH LADAR hardware have succeeded as well. In [31], advances in detector, electric circuitry, and laser transmitter technology are discussed with the capability to capture an entire 3D scene in one transmitted pulse. The advances are similar to [81] with some minor differences: (1) using the APD in Geiger-mode due to laser compatibility and size and power requirements and (2) the capture circuitry is CMOS-based resulting in a 0.5 nanosecond timing resolution. This timing resolution corresponds to range information (i.e. taking a picture) every 15 cm (30 cm for the AFRL

3D FLASH LADAR). A key point in the paper is the huge benefit of employing a photon-counting 3D LADAR with APD detectors versus a CCD camera LADAR. The difference being the APD detectors are photon-counting devices enabling measurements to be made at very low signal levels (0.4 photo-electrons per pixel) as compared to the CCD camera (1.7 photo-electrons per pixel). The paper also highlights foliage penetration as another benefit of 3D LADAR with APD detectors. Tests are run where the LADAR can see through semi-transparent material (i.e. camouflage netting).

Referring to [77], a LADAR capability is presented that can provide target information on sea-skimming anti-ship missiles. Target information includes range and velocity data. Range data is captured by the time-of-flight principle. In RADAR, the target's velocity information is captured from the frequency changes between the transmitted and received pulses. Typical coherent LADAR architectures require mixing at light wavelengths to capture the differences which is very difficult. This paper shows an interesting work-around combining the preciseness of laser light operation and the mature radio frequency mixing technology. The LADAR collects velocity information by using a linear frequency modulated (LFM) radio frequency to amplitude modulate the laser pulse. The receiver collects and coherently mixes in the RF domain rather than at laser light wavelengths thereby reducing complexity.

A gated 3D LADAR is described where the detector is an intensified CCD camera with a Nd:YAG passively Q-switched 32.KHz pulsed green laser at 532 nm [6]. This wavelength provides substantial underwater transmission. However, the system is not covert or eye-safe at 532 nm like the SWIR 3D FLASH LADAR.

In order to perform data registration and extraction, a scanning LADAR is teamed with a 2D digital camera [85]. This paper illustrates an example of using an active and passive system to increase capabilities. One of the challenges with using two sensors is fusing the data sets to represent the information in a consistent coordinate system.

A time-of-flight (TOF) "real-time" 3D video capability using a 3D FLASH LADAR is described in [14]. This paper describes the architecture required which is very similar

to [81] with a focal plane array (FPA) and high-speed ROIC to capture the range data. Considering GPS-denied, GPS-degraded regions or geolocation improvement goals, a method is described where Global Positioning System (GPS) and Inertial Measurement Unit (IMU) data are fused with 3D FLASH LADAR data by Kalman filtering to enable autonomous vehicle control (relative navigation) for space vehicle docking or in-flight jet refueling.

2.6.1.2 Applications. Applications of the 3D FLASH LADAR technology include target identification, rendezvous operations, foliage penetration, mapping, and guidance and navigation. Given the infancy of the capability and the interest in active EO sensing, this list will expand with a substantial increase in performance in each of the areas.

A comprehensive overview of the LADAR topic area is given in [78]. The paper describes utilizing LADAR data to build synthetic environments, developing LADAR system models, and using training sets for algorithms to aid in target recognition and weapon applications (weapon guidance, aim point selection). At the time, the authors used synthetic data to simulate 3D FLASH LADAR data, but will have the hardware available in the future for collects. The fusion of LADAR data with other sensors yielding impressive results. Among the many benefits, one of the most important benefits is more precise targeting thereby reducing collateral damage.

Using an innovative scannerless Multiple-Slit Streak Tube Imaging LiDAR (MS-STIL), [22] reports on LiDAR tests that demonstrate target imaging through foliage and other obscurants. Another test demonstrates capability to image surf zones to identify anti-landing mines and other obstacles.

A variety of 3D scanning LADAR applications are discussed in [17] relating to the use of APDs in the receiver design. The performance of APDs is reported using different materials and at different wavelengths. Applications include: sensor-fused weapons, eye-safe range-finding, and fire-and-forget missiles.

Similar to [14], a very useful application for 3D FLASH LADAR is for aerial vehicle navigation in GPS-denied situations [86]. Teamed with IMU data, the 3D FLASH LADAR is capable of providing autonomous space vehicle navigation or landing systems on the

moon or other planets. IMU measurements drift over time due to the errors encountered in integrating many sensor measurements. GPS is one mitigation technique to combat this drift. In GPS-denied or degraded regions, 3D FLASH LADAR data can replace GPS data to recalibrate the IMU measurements.

Another example of applying 3D FLASH LADAR data for autonomous vehicle navigation focuses on spaceborne rendezvous and capture [40]. The LADAR data benefits this application area by providing an independent range to the docking platform regardless of the existence of other docking sensors. Additionally, the LADAR could provide an image of the docking platform used to verify its integrity.

2.6.2 3D FLASH LADAR Post-Processing. The post-processing of 3D LADAR data (scanning and FLASH systems) includes range estimation, object retrieval, data registration, edge detection, feature extraction, planar feature detection, multi-sensor assisted navigation and target identification, multiple return detection, surface imaging, noise reduction, detector response deconvolution, illumination pattern renormalization, jitter removal, super-resolution, and image enhancement. With the fields of image processing and RADAR being very mature, the application of theory to 3D LADARs from both these fields is, in many cases, novel. While the processing methods by themselves are not new, the application of these methods to the 3D LADAR data set may have never been done.

2.6.2.1 Range Estimation. In [9], the waveform parameters (target range, target amplitude, and pixel bias) of a 3D FLASH LADAR are estimated via a maximum likelihood derivation. A Cramer-Rao Lower Bound (CRLB) on range estimation is also derived. The unknown target parameters are estimated by using maximum likelihood analysis on an idealized waveform model (no pixel coupling). Results show that centimeter level range accuracy is attainable. Closed form solutions for the CRLB are provided in the follow-up work in [39]. Several different scenarios are investigated including multiple returns and distorted return pulses due to slanted surfaces.

Referring to [83], an unusual approach to range estimation in a 3D scanning LADAR is employed called the Viterbi algorithm which is a maximum likelihood sequence estimator (MLSE). It is an intelligent search algorithm that picks the most likely sequence at each stage resulting in the Viterbi path. The Viterbi path results in an estimated object from 3D LADAR scans. Without modifying the algorithm, computational complexity for a real-world array (e.g. 128×128) make this algorithm prohibitive. Results from a modified VA algorithm are compared to a peak detector and Wiener filter method showing that VA outperforms the other methods in terms of range error. The modification reduces the required computations.

3D surfaces are able to be characterized by a LADAR system capable of handling multiple returns in a single received signal [32]. The LADAR can measure range and obtain information about 3D structures at ranges from a few meters to several kilometers. The authors employ a Bayesian statistical approach based on reverse jump Markov chain Monte Carlo (RJMCMC) techniques to estimate the number, positions and amplitude of received signals. Two types of receivers are considered for ranging and depth measurement. The types are Time-Correlated Single Photon Counting (TCSPC) and Burst Illumination Laser (BIL) (e.g. range gating or repeated BIL). The analysis assumes a simplified case whereby each pixel is independent from other pixels. A Bayesian approach is employed because it accounts for uncertainties in the model and parameter values and it can incorporate prior knowledge if applicable. A modified version of RJMCMC incorporates a delayed rejection step permitting the Markov chain to mix better through different proposal distributions.

Based on their previous work [32], the authors modify an assumptions by changing the single independent pixel model to one that includes pixel spatial interdependencies [33]. The inter-pixel dependencies are asserted to arise naturally in imaging real world objects. Again, the number, positions and amplitudes of the received signals are estimated using RJMCMC incorporating either spatial mode jumping (change position of peak) or spatial birth/death process (creating a new peak, or removing a peak).

Two-dimensional range images are used to estimate the target location and range [36]. These estimates are attained by utilizing a three-dimensional distortion tolerant filter on a three-dimensional binary representation of the 2D range image. The distortion tolerant filter is derived by neglecting out-of-family correlations and minimizing the output energy of the input scene due to additive noise. The filter is considered distortion tolerant by using a reference target training data set to recognize the targets from various perspectives. In [35], the 3D distortion tolerant filter work is extended to include the effects of disjoint background noise.

In [58], the authors describe a 3D FLASH LADAR sensor architecture development with theoretical development centered around range processing and polarization discrimination with associated experimental results attaining range resolutions of 1 inch range resolution for occluded targets and 0.3 inches for non-occluded targets. The ranging algorithm is called “bin-balancing matched filter” or BBMFTM which uses the known pulse shape to find the range at which there is max correlation with the received pulse. A weakness of this algorithm is assuming the transmitted and received pulse shapes are matched. Sloped targets and range clipping makes this assumption less valid.

The authors in this paper use coherent detection LADAR data with the expectation-maximization algorithm to develop a method to fit a multi-resolution (wavelet) basis to LADAR range data in a maximum likelihood sense [26]. The Haar-wavelet basis is used resulting in a computationally efficient and robust algorithm. The wavelet basis is used for range anomaly suppression to decrease range error.

Referring to [4], a laser scanning LADAR and several ranging methods are described. These methods include: thresholding, bump-hunting, maximum likelihood (ML), and Reversible Jump Markov Chain Monte Carlo Processing (RJCMCMC). Bump-hunting and ML was found to be able to discern multiple targets from an apparent single return. During low light levels, RJCMCMC was shown to be the best performer in terms of range accuracy.

2.6.2.2 Other Processing Methods. Integration methods are described where 3D FLASH LADAR technology is integrated with inertial measurements to deter-

mine position and attitude of UAVs whether GPS is available or not [27]. The LADAR data is used to extract planar, line, or point features corresponding to walls or corners. These features are combined with IMU measurements to change platform attitude or velocity.

In [80], a 3D scanning LADAR is used to show the capability of 3D FLASH LADAR's penetration through camouflage and foliage. (The authors did not have access to a 3D FLASH LADAR at the time.) Waveform analysis is performed to show the multiple return detection capability important in FOPEN (FOliage PENetration). The Expectation-Maximization algorithm is used to detect the number of peaks in a given returned signal. With the returned signal assumed to be a sum of Gaussians, the mean (target location) and standard deviation were estimated. By using waveform processing, algorithms are described that exploit the multiple returns when the LADAR illuminates vegetation or camouflage. By deconvolution, hidden targets under obscuration are capable of being detected. Estimation of target location and waveform width is performed assuming a Gaussian pulse in a noiseless system, but no detail was provided as to the estimation method. The ability to see inside a dark van and buildings through Venetian blinds is shown. Vegetation removal to aid in FOPEN is considered a research priority for future work.

Using the AFRL 3D FLASH LADAR, an object retrieval algorithm is developed for a 3D FLASH LADAR system illuminating a bar target using a microscanning technique [1]. Microscanning is required in this system due undersampling in the spatial domain. The microscanning method forces the eventual data output to meet Nyquist sampling requirements by developing a super lattice of points similar to super-resolution techniques. The object retrieval algorithm was derived by maximizing the log-likelihood function with respect to a particular point in the remote scene (object) with the final result similar to the Richardson-Lucy algorithm. Cube registration (CR) is performed by computing the translational shifts between the data cubes in all three dimensions. Because the data cubes are sampled properly in the range dimension, cubes are shifted in the range dimension so that each cube represents a common range to the target. The average range to the target in the data cubes are calculated and then compared to produce a range so that each image frame within the data cube corresponds to the same distance. In the spatial domain, transverse

shifts between cubes are accomplished by the vector projection method by calculating the global shifts between corresponding frames in each data cube and then averaging the shifts across all frames in the cube. This averaged global shift is assumed the only shift for the cube considering the fast acquisition time of the sensor.

In [72], a scanning laser and passive electro-optical (EO) camera are used to create data sets enabling sophisticated data-processing methods to use for building 3D environments, data classification, bare earth extraction, 3D-reconstruction of buildings, and identification of single trees and estimation of their position, height, canopy size and species.

Processing methods are presented that convert raw 3D FLASH LADAR data to cleaned 3D data cubes enabling information to be generated, displayed, and analyzed in real time [12]. The processing methods include: “noise reduction, ground plane identification, detector response deconvolution and illumination pattern re-normalization.” Of most interest in this paper is the development of the APD response deconvolution. Ideally, each voxel would represent a single area of the remote scene. However, the APD detectors are not ideal and the voxel experience coupling between each other. Since the true APD detector response is tough to measure, the effects of the multiple-pixel coupling are mitigated by identifying the range tails within the array and moving the tail’s energy closer to the voxel of interest.

In [10], 3D FLASH LADAR data is used to collect lacunarity metrics which are used to measure and characterize forest canopy gaps. The goal is to establish the availability of sub-canopy collections and to characterize the imaging performance of different canopy and forest types.

Using a range-gated 3D LADAR, [79] describes the ability to process the data and characterize different targets such as forests, snow, human faces, and the ability to penetrate vegetation.

A Bayesian estimator is derived to perform deconvolution for object retrieval improving 3D FLASH LADAR system range resolution and probability of detection [7]. From the deconvolution, the system improves its ability to identify surfaces where the return pulse re-

flected thereby removing the range estimate ambiguity caused by the waveform pulsewidth. Of note, no form of the object is specified (i.e. transmitted pulse shape).

In [53], target detection is performed on 3D LADAR data by using a novel 3D volume correlation filter. The filter operates by finding the parameter value that maximizes the volume correlation between the data and either a 3D model or known 3D reference. Methods of perspective correction are also described such that objects are represented by their true relative size.

The limits of theoretical resolution in 3D LADAR systems are derived in [41]. While previous work focused on coherent detection LADARs, this paper extends their work to derive fundamental resolution limits in direct detection 3D scanning and FLASH LADARs. The “volume of resolution” is a constant metric allowing the LADAR designers to balance spatial and range resolution consistent with system goals.

Multiple post-processing methods for a 3D FLASH system are described in [35] including matched filtering, coordinate mapping, jitter removal, and registration. Although, no object retrieval methods are employed to improve results.

A super-resolution method is developed for 3D FLASH LADAR in [68]. Performance of the method using synthetic and real targets is shown to be better than upsampling and interpolating methods by using the Canny edge detection algorithm [11].

In [15], this paper develops an image deconvolution technique using regularized inversion followed by a denoising filter. Inversion refers to the ill-posed problem of removing the blur from the the imaging model. The inversion process can produce poor results in the presence of noise due to its uniform amplification across frequencies. Regularized inversion (such as Wiener filtering) can alleviate such problems. Also, assuming there are similar patches within a natural image, the de-noising filter is based on a block-matching and 3D (BM3D) filtering method. This work extends the regularized inversion, regularized wiener inversion, and BM3D work to handle colored noise. Of note, a regularization parameter that is determined empirically is used in the inversion process.

2.6.3 *Blind Deconvolution.* As part of the research effort, blind deconvolution techniques will eventually be employed given a laboratory or field test with a 3D FLASH LADAR remote sensing scenario. A review of the pertinent blind deconvolution literature is appropriate given this realistic situation. 2D passive electro-optical papers usually have one object and many different blurring functions due to relatively slow image acquisition times with corresponding atmospheric turbulence. Whereas, the 3D FLASH LADAR blind deconvolution scenario has many different objects with one blurring function regardless of atmospheric turbulence strength. Each data cube of 3D FLASH LADAR is considered to be blurred by one point spread function due to the rapid acquisition time for the range images.

Overall, there were *no* papers found that attempted to restore the object by performing blind deconvolution on any type of 3D LADAR system. The optical astronomy field dominates the image blind deconvolution publications. The main difference between this research versus the typical blind deconvolution is that this research endeavors to estimate the waveform parameters located within the object and a single point spread function while the typical 2D image blind deconvolution problem estimates the phase within the point spread function and a single object. In other words, rather than parameterize the point spread function, the object has been parameterized in this research.

Generally regarded as one of the founding blind deconvolution papers, [59] performs signal recovery for multiplied and convolved signals by using homomorphic filtering utilizing the complex cepstrum of the signals. Results of the filtering technique applied to deconvolution problems are shown in speech processing and echo removal.

The other founding paper concerning blind deconvolution recovers the original music from old-time vinyl records by homomorphic filtering or power spectrum estimation techniques [82]. The assumed mathematical model is audible music resulting from the original music convolved with a record players impulse response. They subsequently extend the theory to a simple imaging example whereby they look to remove the effects of image blur caused by camera motion, inaccurately focused lenses, and atmospheric turbulence.

In [42], general blind deconvolution methods are reviewed and classified into 2 classes which are (1) PSF estimation separate from the true image estimation and (2) simultaneous estimation of the PSF and true image. The first class uses a simple technique called *A Priori* Blur Identification methods. The second class incorporates several techniques including Zero Sheets Separation, Autoregressive Moving average (ARMA) Parameter Estimation, Nonparametric Deterministic Image Constraints Restoration, and Nonparametric Methods based on High order Statistics. In the follow-up paper [43], the authors discuss other blind image deconvolution methods that were omitted from their previous article which were projection-based blind deconvolution and maximum likelihood restoration.

Given the mathematical model in this research, the most germane article is from [71]. This paper develops a maximum-likelihood based blind deconvolution technique on images corrupted by photon noise without the need for a nearby reference point source which can converge to the solution faster (e.g. less required frames) than techniques that do require a point source. The blind deconvolution technique is called the Generalized Expectation Maximization (GEM) algorithm based on the seminal work by Dempster, *et al.* [16]. The GEM algorithm is advantageous due to its ability to reduce the maximization complexity and to uncouple the object and blurring function.

In [46], the blind deconvolution is performed by error minimization via conjugate gradient minimization where the error is a composite of deviations from image and Fourier space constraints. Also, blind deconvolution techniques are used with phase estimation methods for object retrieval on raw speckle images.

Using Kolmogorov statistics to model the turbulent atmosphere, blind deconvolution is performed on astronomical speckle images approximating the shot noise by a weighted Gaussian noise model [47]. The weighted Gaussian model is used because the author asserts that many imaging situations don't fit the usual Poisson or Gaussian noise statistics.

In [21], an iterative blind deconvolution algorithm based on the Richardson-Lucy algorithm is developed and compared with a Wiener filter blind deconvolution algorithm [50], [62]. The authors choose to develop a new algorithm based on the Richardson-Lucy algorithm

due to its proven robustness in the presence of high noise levels. They also perform a “semiblind” deconvolution by attempting improve the algorithm by adding *a priori* information by assuming a functional form of the PSF. By “parameterizing” the PSF, the number of unknowns of the PSF reduces drastically. Conclusions from this paper are that the Richardson-Lucy algorithm is more stable than other blind deconvolution algorithms and has a better noise tolerance than the Ayers-Dainty and Wiener filter algorithms. From [2], the Ayers-Dainty algorithm generalizes the Feinup phase retrieval algorithm by implementing an iterative technique based on Fourier transforms along with energy conservation, an image non-negativity constraint and Fourier domain constraints to estimate the object and PSF.

Another attempt to retrieve the object and PSF is accomplished by a maximum a posteriori (MAP) estimator on a 2D LADAR imaging system [52]. Although, in this case, it is the optical transfer function (OTF) that is estimated by parameterizing the OTF based on Fried’s seeing parameter. This paper also develops a MAP estimator for the speckle parameter in a negative binomial probability distribution modelling partially coherent light.

Considering the field of fluorescence microscopy, blind deconvolution is performed using an iterative expectation-maximization approach with some prior knowledge of the PSF characteristics and assuming Poisson noise statistics [34]. The characteristics include circular symmetry (general symmetry is also presented) and a band-limited nature. The symmetry argument is appropriate due to the symmetrical nature of most apertures. The band-limit constraint, which rules out the trivial solution, also is appropriate due to the low-pass filtering effect of optical systems. The trivial solution is the solution where an impulse is convolved with the degraded image. Using these constraints, the algorithm suitably reconstructs the original images.

In [87], image recovery is performed from noisy and blurred observations by implementing an adaptive finite impulse response filter. Coefficients of this filter are updated using a two-dimensional Constant-Modulus (CM) cost function similar to one-dimensional blind adaptive equalization found in the communications field.

Focusing on astronomical applications, this paper builds on the iterative blind deconvolution result from Ayers and Dainty [2] by utilizing methods that reduce edge effects, account for different convergence rates of the object and impulse response, shorten convergence time, and perform noise dampening [3]. The methods are valid when only constraining the data to be positive. A method of initializing the spatial impulse response is attained by using autocorrelations of the observed image.

Referring to [18], image reconstruction of a blurred and noisy optical system is performed using phase diversity, deconvolution (Richardson-Lucy based), and iterative blind deconvolution. All three methods satisfactorily reconstruct the image with similar accuracy, but deconvolution is fastest. Their work handles extended scenes or scenes in which the object either encompasses the FOV entirely or is larger than the FOV. Consequently, the edge effects cannot be ignored and must be accounted for in the algorithms.

In [61], blind object reconstruction is accomplished by reducing the 3D problem into a set of 2D problems. Along with imposing positivity and bandlimit constraints, new estimates of the 2D image and PSF are obtained by Wiener filtering the Fourier transform of the image or PSF respectively with the current estimate. There is an important result concerning 3D vs. 2D sampling requirements. As opposed to the 2D image scenario, 3D blind deconvolution has a unique solution even if the data is not Nyquist sampled.

2.6.4 CRB and Parameter Optimization. Compared to the convolution model contained in the present paper, previous work on bounding range performance in the LADAR topic area focused on single pixel (i.e. single target in a pixel) analysis. In [9], a CRB on range estimation is derived for a single pixel of a 3D FLASH LADAR. In support of the bound, the unknown waveform parameters (target range, target amplitude, and pixel bias) are estimated via a maximum likelihood estimation algorithm. Theoretical and simulation results show that centimeter level range accuracy is attainable. Closed form solutions for the CRB are provided in the follow-up work in [39].

Another paper developed a signal-to-noise (SNR) based method to determine range and spatial resolution limits of scanning and direct detection LADAR [41]. While account-

ing for the proper LADAR noise sources and operating parameters, the SNR-based method does not consider the performance of the algorithms required to estimate the resolution in the presence of noise.

Other literature has utilized the Gaussian function to describe the object. In [28], the object profile is defined by a Gaussian in one dimension corrupted by additive Gaussian noise. The CRB on a one target profile estimation is performed. In another paper, the object is a two-dimensional (2D) Gaussian describing the incident intensity on a charge-coupled device (CCD) array [89]. This 2D Gaussian is used to develop a two-dimensional CRB for any unbiased position estimator as well as a maximum-likelihood (ML) position optical estimator (position only, no range information or estimate).

The use of the CRB in parameter optimization or performance characterization has been done previously in fields such as heterodyne Light Detection and Ranging (LiDAR), RADAR, and positron emission tomography (PET) [20], [44], [48], [49], and [69]. In all the papers, the method was to pick the optimum condition based on CRB minimization either through physically-based analytic expressions or bound comparisons over different parameter choices. In [69], comparisons are made using the CRB concerning Doppler estimation in heterodyne and direct detection LiDAR given several different operating parameters. Also, methods are discussed that enable heterodyne Doppler estimation performance to approach that of the CRB. Concerning synthetic aperture RADAR (SAR) design in [49], the CRB developed in this paper showed that performance is enhanced by implementing a multi-dimensional aperture over a one-dimensional aperture. In [48], the CRB is used to validate the use of range compression in multi-input multi-output (MIMO) RADAR. Also, waveform optimization in MIMO RADAR is accomplished via several minimization techniques on the CRB matrix to include minimizing the trace, determinant and largest eigenvalue. Another paper uses the CRB to select an optimal RADAR beamspace transformation operator [20]. The optimality condition metric is physically-based using the analytical form for the beamspace transformation that minimizes the CRB function itself. Finally, the design parameters of avalanche photo diodes (APD) used in small animal PET are optimized by selecting those parameters from the search space that the minimize the CRB [44].

III. Laboratory Data Collection

In order to verify theory and simulation range estimation results, laboratory measurements were collected using an Advanced Scientific Concepts (ASC) Inc. three dimensional FLASH LAsER Detection And Ranging (3D FLASH LADAR) that illuminated a target corresponding to one used in simulation. The details behind the collection are the topic of this chapter.

Using the three bar target template, a laboratory experiment was conducted using 3D FLASH LADAR hardware consistent with parameters in Table 3.1. Experimental results presented in a later chapter show range estimation improvement after applying the object recovery techniques. However, modifications to the camera and raw data were necessary to enable a proper experiment and ensure that the data matches the model from Section 2.5. The system point-spread-function (PSF) is also determined experimentally using a step target which is done such that the PSF can be used in the object decoloration algorithm (Wiener filter) detailed in Section 5.1.1. Finally, the ability to use object recovery algorithms is contingent on using the incoherent light model described in Section 2.1. Thus, the speckle parameter of the partially coherent light distribution is estimated and compared against the incoherent model. While some speckle noise is evident in the data, the estimation results indicate that the incoherent model is a valid approximation.

The chapter is organized as follows: Section 3.1 provides details on the 3D FLASH LADAR hardware, Section 3.2 discusses the laboratory collection set-up used for experimental data processing in Section 5.3, Section 3.3 identifies the default hardware configuration as spatial aliased and describes the correction, Section 3.4 provides the steps required to pre-process the experimental data including gain variation equalization and photon scaling, Section 3.5 specifies how the system PSF was attained from a step target, and Section 3.6 derives a speckle parameter estimator and performs the estimation on the experimental data.

3.1 3D FLASH LADAR Hardware Description

A 3D FLASH LADAR is an active, pulsed system that is both an imaging and ranging sensor. It produces a time sequence of two-dimensional (2D) images due to a fast range

Table 3.1: 3D FLASH LADAR parameters

Parameter	Value
Detector Array	128×128
Aperture Diameter (D)	2 mm
Mean Wavelength	$1.55 \mu\text{m}$
Focal Length	0.30 m
Target Range	5.21 m
Transmit Energy	10 mJ
Pulse Standard Deviation (σ_w)	3 ns
Beam Divergence	0.009 radians
Detector Spacing	$100 \mu\text{m}$
Detector Array Fill Factor	100%
Detector Bandwidth	$0.5 \mu\text{m}$
Target Reflectivity	10%
Solar Irradiance	$10 \text{ Watts/m}^2/\mu\text{m}$
D/r_o Seeing Condition	1.43
Frame Rate	30 Hz
Time Samples	20
Sample Period	1.876 ns

gate resulting in a 3D data cube of spatial and range scene data with excellent range resolution [19], [81]. FLASH technology principally differs from scanning LADAR by being able to form a 3D representation of a remote scene in one laser pulse rather than rastering a 3D scene together using many pulses. This capability results in faster scene collection times with lighter weight, lower power, and reduced mechanical complexity as compared to the scanning systems. Operating in the eye-safe short-wave infrared region (SWIR) of the electromagnetic spectrum at 1570 nm, a representative system shown in Figure 3.1 is built by ASC, Inc. and has receiver electronics consisting of a 128×128 detector array and associated circuitry capable of producing twenty (20) 2D range slice images [66]. Detector pixel separation is 100 micrometers with nearly 100% fill factor due to a focusing micro-lens array in front of the detector pixel array. An extremely fast range sampling interval of 1.876 ns makes it nearly impervious to platform motion distortion for a single cube collection. Depending on the LADAR operating mode, each pixel could either have a distinct starting range dependent on received photon levels (“hit mode”) or have the same starting range (“sular mode”). Capable of “real-time” 3D movies, it produces a cube of spatial and

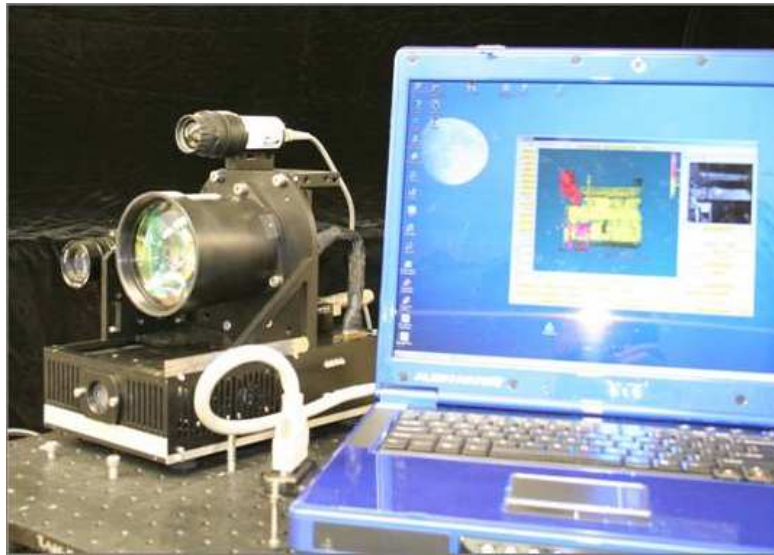


Figure 3.1: A picture of the Applied Scientific Concepts (ASC) Inc. 3D FLASH LADAR system including the laser, receiver optics and electronics, and laptop. ASC provides a laptop to operate the LADAR and view and process the received signals.

range scene data where each 2D range slice image contains the detected counts proportional to the incident photo-electrons upon each pixel in the detector array. Four dimensions of data are available to include the two spatial coordinates, range, and intensity.

As previously described, a 3D FLASH LADAR operates in one of two modes. The first mode is called “hit mode” where each pixel element (pixel) is independently triggered when its intensity reaches a preset threshold. This mode is advantageous when searching for a target where the range is not already known. However, truncated waveforms can occur leading to range estimation errors. The second mode is called “sular mode” where the pixels are triggered to start recording data together based on a preset range. Benefits of this mode include being able to successively capture fine details of the target and background. Drawbacks are that the target range must be known a priori and waveforms are truncated for targets near the end of the collect. An potential CONcept of OPERations (CONOP) is for “hit mode” to operate like a search RADAR and, once the target is acquired, “sular mode” would track and identify the target.

The breakthrough technology in the ASC 3D FLASH LADAR is the Laser RADAR Processor (LRP) which allowed for the fast range sampling and independent pixel control [63]. Due to advances in semiconductor technology, the LRP was originally a 32 x 32 detector array with 400 μm pixel separation which improved to a 128 x 128 array with 100 μm pixel separation using Indium Gallium Arsenide (InGaAs) avalanche photo-diodes (APD) as the detector material. APD detectors generate many electrons for a single incident photon and are useful in low-light situations. The fast range sampling is achieved by analog and digital circuitry independently located behind each of the pixels.

3.2 Data Collection Details

Located at Wright-Patterson AFB, OH, the Air Force Research Laboratory (AFRL) Sensors Directorate contains facilities acceptable for operation of the 3D FLASH LADAR. Ideally, the intent would be to operate the LADAR from the top floor of the building across a considerable distance (kilometers) right after dusk to experience atmospheric turbulence. However, due to the constraints of the aperture size (discussed in Section 3.3), the target range is shortened to meters to allow for a sufficient signal-to-noise ratio (SNR). The range to the first surface is 5.21 m and is set up to be 1.7 m into the range collections. Range to the second surface is 1.22 m from the first surface to give roughly four range samples between surfaces.

Receiver optics required some modifications from the default configuration [66], [9]. The optics are focused on the first surface which means that the successive range collects are slightly de-focused. The resulting data shows little effect from the lack of focus. Considering the short range distance, a one degree diffuser is put on the laser transmission optics to enable the entire target to be illuminated by the beam without lowering the SNR prohibitively. The focal length is set at 300 mm. Due to sampling issues covered in a later section, the aperture diameter is changed to 2 mm by using brown cardboard with a circular hole cut in the center placed in front of the supplied aperture (10 cm). Using similar triangles, each detector pixel field of view (FOV) x_p corresponds to 1.7 mm at the target

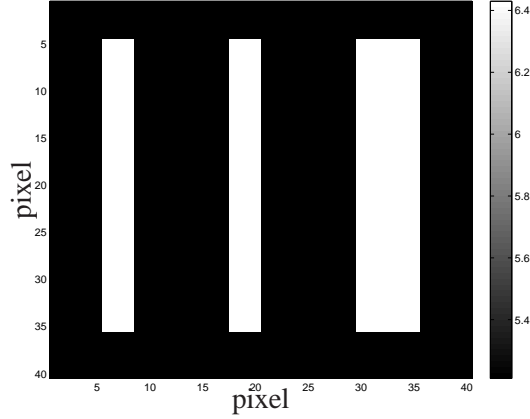


Figure 3.2: True ranges of the three-bar target with first surface at 5.21 m and second surface at 6.43 m with 1.22 m of separation in between surfaces.

location determined by the following calculation:

$$\begin{aligned}
 \frac{x_p}{x_t} &= \frac{x_d}{f_l} \\
 \frac{x_p}{5.21 \text{ m}} &= \frac{100 \mu\text{m}}{300 \text{ mm}} \\
 x_p &= 1.7 \text{ mm}
 \end{aligned} \tag{3.1}$$

where x_t is the target range, x_d is the pixel separation, and f_l is the focal length.

Referring to target template depicted in Figure 3.2, the first surface targets are constructed from white, flat cardboard with the bars cut out of one board (first surface) and the other board is left untouched (second surface). There are two slimmer rectangle targets and one larger rectangle target. The slimmer targets are 0.5 cm width by 5 cm length and the larger target is 1 cm width by 5 cm length. All three targets are individually separated by 1.5 cm (edge to edge).

3.3 Spatial Aliasing

Due to limits in current detector technology requiring a large footprint for the electronics behind each pixel, the receiver optics are spatially under-sampled which needs to be mitigated in order for the received data to be unaliased. The aliasing would cause uncertainty in the received data and violate the data model. The default configuration is aliased

because of the Nyquist sampling theory in which the sampling rate must be at least twice the highest frequency content in the signal. The optics are a natural low-pass filter with the highest frequency called the cut-off frequency. For incoherent imaging, the cut-off frequency is [25]

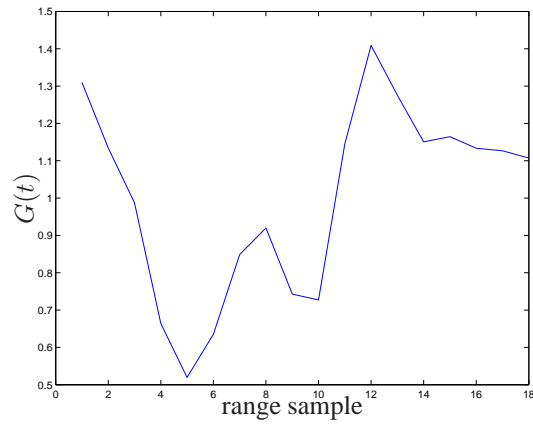
$$f_o = \frac{D}{\lambda z_i} \quad (3.2)$$

where D is the aperture (exit pupil) diameter, λ is the light wavelength, and z_i is the image distance. Therefore, the focal plane must sample at twice this spatial frequency or $2D/\lambda z_i$. The typical apertures for this camera are in the centimeters. For example, an aperture of 10 cm would equate to a spatial frequency sampling requirement at 4.3×10^5 cycles per meter. At 100 μm spacing, the detector array does not meet this requirement. If the aperture is reduced to 2 mm, then the spatial frequency sampling requirement is now at 8.6×10^3 cycles per meter which the detector array can meet. However, the aperture reduction comes at the expense of reduced light gathering and shortened range in which the LADAR can be operated. Thus, the target range is placed at 5.21 meters (near the minimum ranging distance of the sensor) to obtain high enough signal to noise ratio (SNR) in the collected data.

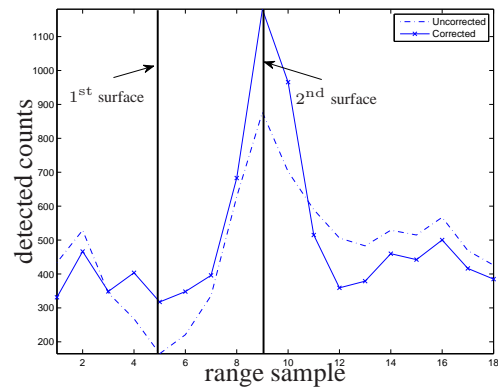
3.4 Data Pre-processing

The data observations from the 3D FLASH LADAR hardware need pre-processing steps to be suitable for insertion into the Wiener filter and GEM algorithms. In simulation, the noisy and blurry data are well-controlled and therefore, well-behaved. While the experimental 3D FLASH LADAR data exhibits expected pixel waveform shapes (i.e. Gaussian-like) and spatial blur, the data is ill-behaved to a degree due to inherent features of the hardware performance.

Referring to [38] and [73], the experimental hardware experiences a gain phenomenon whereby a pixel's gain drops when laser energy is incident upon a large area of another part of the detector array. With the three bar target, the laser energy is incident on the front surface first which causes second surface pixels to experience a gain drop. Figure 3.3(b)



(a)



(b)

Figure 3.3: (a) Gain profile correction resulting from executing Equation (3.7). By looking at background pixels, the hardware gain dip is clearly evident at the first surface (near range sample five) and the second surface (near range sample nine). The first surface gain drop is larger than the second surface gain drop due to the larger number of pixels illuminated (i.e. larger surface area). Amount of gain drop is proportional to received intensity level and quantity of pixels illuminated.

(b) Investigating Pixel(19,32) from experimental three bar target, the pixel waveform benefits from the gain variation correction by removing the gain drop near range sample four. After correction, the pixel waveform looks more like the intended pulse model, but with unwanted noise artifacts.

shows the gain drop for a second surface pixel. The method for correcting the gain is to calculate an average gain profile by looking at background pixels (i.e. returned laser energy not incident on these pixels).

Assuming the system noise follows the Poisson distribution and the gain is constant between pixels, the data model for an arbitrary pixel is

$$d(t) = G(t) [I_S(t) + I_B(t)] \quad (3.3)$$

where $G(t)$ is the unitless, time-varying gain, $I_S(t)$ is the laser signal in units of photons, and $I_B(t)$ is the background signal. A new variable $\hat{d}(t)$ is determined by

$$\hat{d}(t) = \frac{d(t)}{\bar{i}_B(t)} \quad (3.4)$$

where $\bar{i}_B(t) = G(t) \bar{I}_B(t)$ is a known average background signal with gain and $\bar{I}_B(t)$ is the mean background signal without gain. The variable $\bar{i}_B(t)$ is separately calculated in the laboratory by averaging the detected background signal for selected voxels across many data cubes. Looking at the background pixels only, $\hat{d}(t)$ is

$$\hat{d}(t) = \frac{G(t) I_B(t)}{\bar{i}_B(t)} = \frac{G(t) I_B(t)}{G(t) \bar{I}_B(t)} = \frac{I_B(t)}{\bar{I}_B(t)}. \quad (3.5)$$

Taking the statistical variance results in

$$\begin{aligned} \text{var}(\hat{d}(t)) &= E \left[\left(\frac{I_B(t)}{\bar{I}_B(t)} - \frac{\bar{I}_B(t)}{\bar{I}_B(t)} \right)^2 \right] = \frac{1}{\bar{I}_B^2(t)} E \left[(I_B(t) - \bar{I}_B(t))^2 \right] \\ &= \frac{1}{\bar{I}_B^2(t)} \text{var}(I_B(t)) = \frac{\bar{I}_B(t)}{\bar{I}_B^2(t)} = \frac{1}{\bar{I}_B(t)}. \end{aligned} \quad (3.6)$$

Applying this result and using a sample variance of \hat{d} in place of the statistical variance ($s^2 \rightarrow \text{var}(\hat{d}(t))$), the gain is determined by

$$G(t) = \frac{\bar{i}_B(t)}{\bar{I}_B(t)} = \bar{i}_B(t) s^2. \quad (3.7)$$

and can be seen in Figure 3.3(a). This gain profile is used on each of the pixel's waveforms to correct for the hardware deficiencies and to more closely match the model. For example, Figure 3.3(b) shows the benefits of the gain correction for one second surface pixel. Also observed in the previous work, a side benefit of gain correction in both first and surface pixels is the waveform becomes more symmetrical. The emitted laser pulse shape is a hybrid of a Gaussian or negative parabolic shape with some asymmetry. Gain correction takes out some of the asymmetry.

The 3D FLASH LADAR is also not a photon-counting device where one digital count equals one photon. The receiver optics use Avalanche Photo Diodes (APD) where one photon equals many detected counts. Consequently, intensity scaling must be performed to condition the data to be consistent with the Poisson distribution. The conditioning is performed by using the statistics of the light and the detected mean and variance of the data. The detected mean of the data is $q\bar{K}$ where q is a scaling factor with units of detected counts per photon and \bar{K} is the true mean in units of photons. Since incoherent imaging is assumed, the detected variance becomes

$$q^2\sigma^2 = q^2\bar{K} \quad (3.8)$$

noting that the mean and variance of the Poisson distribution are the same. The data is scaled by solving for q and then converting the detected counts to photons by

$$d_{ph} = \frac{d_{dc}}{q} \quad (3.9)$$

where d_{ph} is the data in units of photons and d_{dc} is the data in units of detected counts.

3.5 *Experimental PSF*

The Wiener filter is used to provide a comparison to the GEM algorithm [55]. In order to implement the Wiener filter, the PSF must be known. Since the derivative of a system step response is the system impulse response, the PSF is determined by taking the derivative of a

experimental step target. Figure 3.4(a) shows a range image of the step target collected with the same hardware as the bar target data. Although, the entire range image does not meet the requirements of being a step target due to the non-uniform intensity on the left-hand-side (LHS). Therefore, a symmetric impulse response was assumed and the right-hand-side (RHS) of the impulse response was copied and flipped over to use as the LHS. Figure 3.4(b) exhibits the resulting profile with an outer product operation producing the two-dimensional PSF. Phase retrieval is then performed via the Gerchberg-Saxton algorithm to arrive at the PSF used by the Wiener filter [23]. This requirement to know the PSF is a shortcoming of the Wiener filter algorithm. Figures 3.4(c)-(d) show the optical transfer function (OTF) where the optics exhibit a nearly diffraction-limited performance.

3.6 Speckle Parameter Estimation – Incoherent Imaging

Both the negative binomial and Poisson distributions can be used to capture the non-negative, discrete nature of the laser light. The negative binomial distribution would be the most optimal in describing the illuminating partially coherent laser light, but blind deconvolution methods are cumbersome [24]. Whereas, blind deconvolution methods with the Poisson distribution (incoherent imaging) are more tractable and, thus, utilized in this research. Even if the speckle is severe, the benefit of modeling the speckle does not outweigh the cost of implementing a partially coherent blind deconvolution model for the 3D FLASH LADAR system. Previous research using the incoherent data model for a 3D FLASH LADAR has also experienced success [9], [39].

To gain more insight into this assumption, a simple approach is to estimate the amount of coherence contained within the 3D FLASH LADAR data by estimating the speckle parameter of the negative binomial distribution directly from the data [24]. Capturing both temporal and spatial coherence, if the speckle parameter estimate is high enough, the negative binomial distribution will look Poisson-like allowing the data observations to be modeled as arising from an intensity convolution (incoherent imaging). Including speckle and photon noise effects, the negative binomial probability mass function (PMF) describes the photon distribution of a partially coherent imaging system for a single pixel

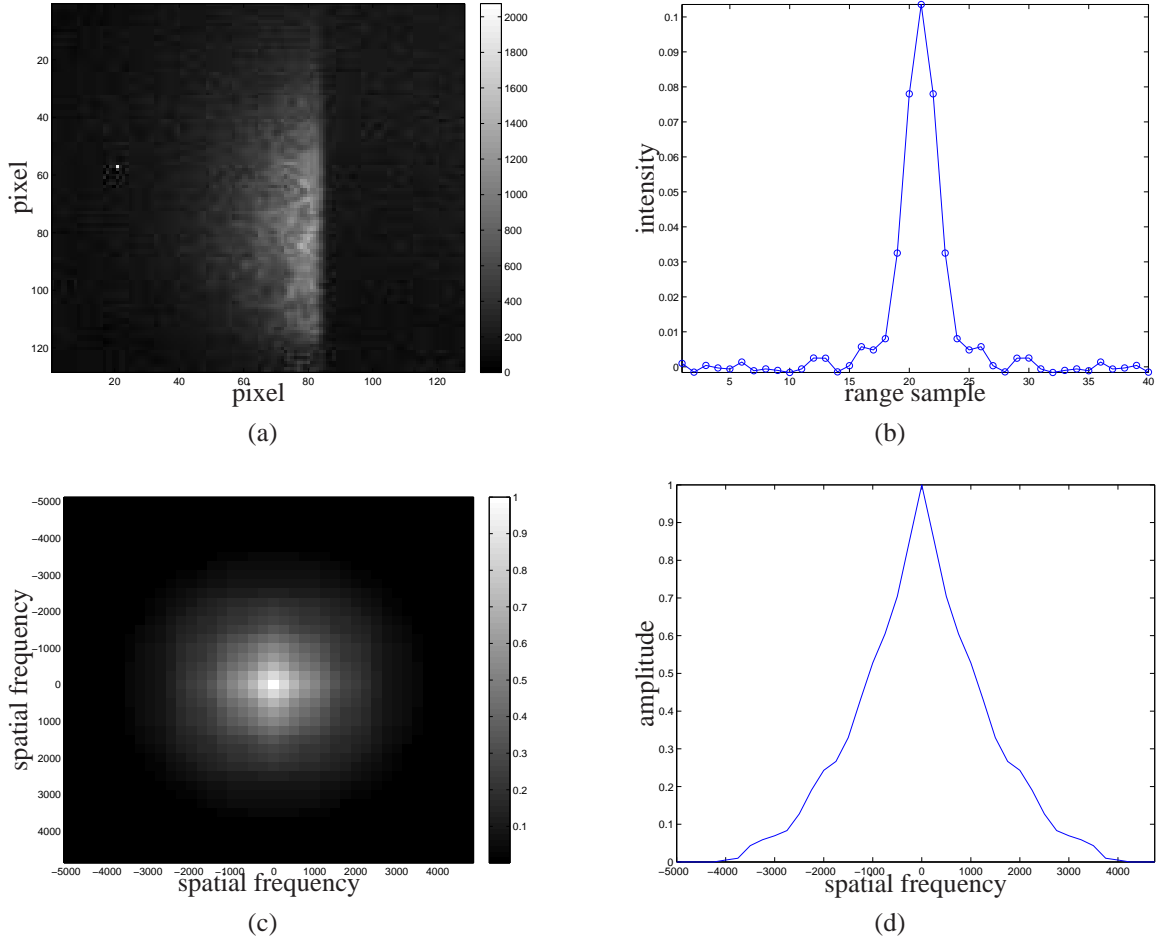


Figure 3.4: (a) One range image of the step target data cube. Although the board edge is clearly visible, the variable intensity across it causes an issue with the impulse response calculation. The step response definition requires a constant amplitude at all spatial positions. The target board portion of the step response does not meet this requirement, but the non-target area (right-hand-side) does exhibit a constant amplitude. The portion of the step response function where it turns off is this non-target area. Performing the step response derivative only on this non-target area solves the problem of variable target board amplitude.

(b) 1D cut-out of the resulting PSF. Assuming circular symmetry, an outer product operation is used to find the corresponding 2D PSF.

(c) Optical transfer function (OTF). The OTF is found by taking the Fourier Transform of the experimental PSF [25].

(d) 1D cut-out (zero spatial frequency) of the OTF. The profile shows nearly diffraction-limited optics with a cut-off frequency at 4050 cycles per meter.

or [24]

$$P(K) = \frac{\Gamma(K + \mathcal{M})}{\Gamma(K + 1)\Gamma(\mathcal{M})} \left[1 + \frac{\mathcal{M}}{\bar{K}}\right]^{-K} \left[1 + \frac{\bar{K}}{\mathcal{M}}\right]^{-\mathcal{M}} \quad (3.10)$$

where \mathcal{M} is the speckle parameter and \bar{K} is the pixel's average photon count. Changing the distribution for a 3D FLASH LADAR, the illuminating laser light statistics for a particular volume element (voxel) (x, y, k remain constant) across many data cubes is

$$P(D_{jk}(x, y) = d_{jk}(x, y) \forall j \in (1, 2, \dots, J)) = \prod_{j=1}^J \frac{\Gamma(d_{jk}(x, y) + \mathcal{M})}{\Gamma(d_{jk}(x, y) + 1)\Gamma(\mathcal{M})} \left[1 + \frac{\mathcal{M}}{\bar{K}}\right]^{-d_{jk}(x, y)} \left[1 + \frac{\bar{K}}{\mathcal{M}}\right]^{-\mathcal{M}} \quad (3.11)$$

where j represents the data cubes, k is the range image (i.e. time variable) within a data cube, (x, y) are the coordinates in the image plane, and $d_{jk}(x, y)$ is the data observation. The voxels are assumed statistically independent from each other because of the discrete nature of photons and the detected photons do not affect future detected photons. The maximum likelihood solution for the average voxel intensity is determined by

$$\bar{K} = \frac{1}{J} \sum_{j=1}^J d_{jk}(x, y). \quad (3.12)$$

Taking the natural log of Equation (3.11) yields

$$\begin{aligned} \ln [P(D_{jk}(x, y) = d_{jk}(x, y) \forall j \in (1, 2, \dots, J))] = \\ \sum_{j=1}^J \ln \left[\frac{\Gamma(d_{jk}(x, y) + \mathcal{M})}{\Gamma(d_{jk}(x, y) + 1)\Gamma(\mathcal{M})} \right] - d_{jk}(x, y) \ln \left[1 + \frac{\mathcal{M}}{\bar{K}} \right] \\ - \mathcal{M} \ln \left[1 + \frac{\bar{K}}{\mathcal{M}} \right] \end{aligned} \quad (3.13)$$

where graphical methods are employed to find the speckle parameter that maximizes this log-likelihood. Using the same experimental data as in the range estimation efforts, a collection of voxels with the strongest laser light is chosen to estimate the speckle parameter. Figure 3.5 shows the similarities between the negative binomial and Poisson distribution using an average of the estimated speckle parameter.

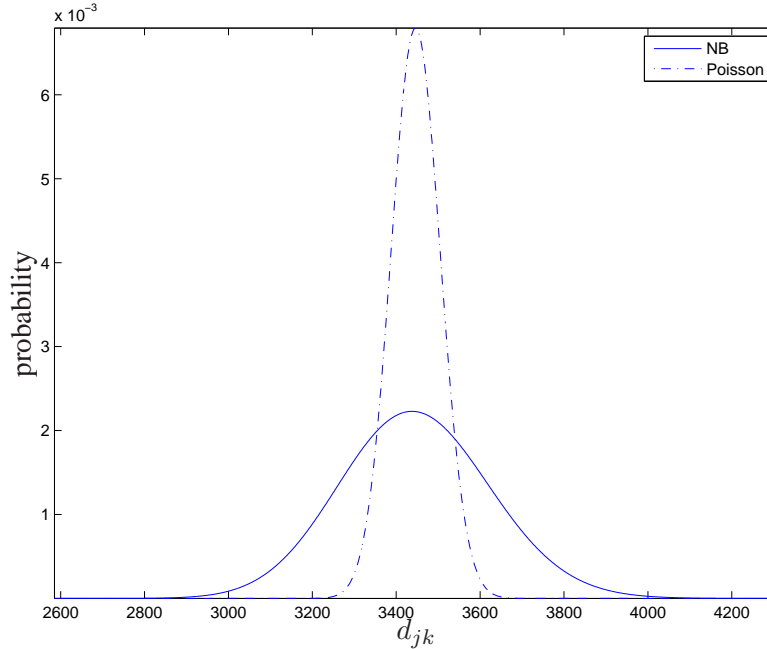


Figure 3.5: This plot shows the negative binomial (NB) using an estimated average speckle parameter ($M = 414$) versus the Poisson distribution with the same mean ($\bar{K} = 3447$). While not identical, the negative binomial distribution compares well enough to the Poisson distribution to assume incoherent imaging.

Even without considering speckle parameter estimation results, the argument can be made for incoherent imaging due to the Poisson distribution's ability to model the non-negativity and discrete nature of light [9], [39]. This argument is solidified by the speckle parameter estimation results indicating that the speckle noise appears low enough for the incoherent imaging model to be used with confidence.

IV. Range Estimation

Range estimation in three dimensional FLASH LAsER Detection And Ranging (3D FLASH LADAR) has been limited thus far to statistical methods that operated on data models that did not incorporate the blurring effect of the spatial impulse response. In other words, there was a one-to-one mapping between the object plane and image plane points. Considering a the 3D FLASH LADAR system as a linear, space-invariant process, the relationship between the object and image plane is fully described by a convolution between the object plane intensity and the intensity point spread function (spatial impulse response). Consequently, the simple models ignore the pixel-to-pixel coupling that could significantly degrade range estimation results. Referring to Chapter II, whether using a simplified model or a higher fidelity model, the method of ranging is exactly the same in that each pixel in the detector array is ranged independently.

This chapter details several pixel-based ranging algorithms include: Section 4.1 – peak detection, Section 4.2 – maximum likelihood [55], Section 4.3 – normalized cross-correlation [56], Section 4.4 – two point target estimator, and Section 4.5 – two surface estimator. The two-point target estimator is a novel contribution that is able to spatially and temporally estimate two point targets in a scene.

4.1 Peak Detection

A very simple ranging algorithm is peak detection. This algorithm selects the range sample $D(x, y)$ based on where the peak sample count occurs or

$$D(x, y) = \arg \max_k d_k(x, y). \quad (4.1)$$

where $d_k(x, y)$ is the received waveform, k is the range sample variable, and (x, y) are the pixel dimensions. Theoretically, if the received waveform was sampled continuously, one could perform peak detection and not encounter any interpolation or quantization error. However, real systems have a sampling period which creates some ambiguity when peak detection is used. Therefore, more capable methods are sought that enable estimation to be sub-sample. Some of the errors though could be mitigated by interpolation. The effects

of spatial coupling and shot noise would further degrade the waveform of a sub-sample target in addition to the deformation already encountered by its sub-sample range position. These effects would make obtaining accurate estimates from standard peak detection very difficult.

4.2 Maximum Likelihood

Based on [55], this section reviews the development of a maximum likelihood method to estimate range to the target at a single pixel given a transmitted Gaussian pulse with additive Gaussian noise. Maximum likelihood is chosen because of its relation to the Generalized Expectation Maximization (GEM) algorithm used in a subsequent chapter where an iterative technique possibly leads to the maximum likelihood solution. From [84], the maximum likelihood estimator is the parameter estimate where the maximum of the *a posteriori* density occurs. Using Gaussian statistics to describe the incoming noise, this *a posteriori* density for an arbitrary pixel (x, y) and range sample k is

$$P [D_k(x, y) = d_k(x, y)] = \frac{1}{\sqrt{2\pi}\sigma} e^{-\frac{(d_k(x, y) - i_k(x, y))^2}{2\sigma^2}} \quad (4.2)$$

where σ is the Gaussian noise standard deviation. The remaining derivation assumes dependence on (x, y) and drops the notation. Since there are N time samples and assuming the time samples are statistically independent of each other, the total distribution across all time samples is the product of the individual distributions:

$$P [D_k = d_k; \forall k \in [1, \dots, K]] = \prod_{k=1}^K \frac{1}{\sqrt{2\pi}\sigma} e^{-\frac{(d_k - i_k)^2}{2\sigma^2}}. \quad (4.3)$$

Given that maximizing the natural log of a function is the same as maximizing the function itself, taking the natural log of Equation (4.3), $L = \ln(P(d(t_k)))$, results in the advantageous

form

$$\begin{aligned}
L &= \sum_{k=1}^K \left[\frac{-(d_k - i_k)^2}{2\sigma^2} + \ln \left(\frac{1}{\sqrt{2\pi}\sigma} \right) \right] \\
&= \sum_{k=1}^K \left[\frac{-(d_k - Ap_k(R) - B)^2}{2\sigma^2} + \ln \left(\frac{1}{\sqrt{2\pi}\sigma} \right) \right]
\end{aligned} \tag{4.4}$$

Because the range and amplitude are both unknown parameters, the estimation process must estimate the amplitude first and is found by [84]

$$\hat{a}_{ml}(R) = \arg \max_A L. \tag{4.5}$$

Taking the derivative with respect to A in Equation (4.4) and setting it equal to zero results in

$$\sum_{k=1}^K \left[\frac{2(d_k - Ap_k(R) - B)}{2\sigma^2} \right] p_k(R) = 0 \tag{4.6}$$

where the term that doesn't depend on A has been dropped. Grouping terms and canceling σ^2 gives

$$\sum_{k=1}^K ([d_k - B]p_k(R) - Ap_k^2(R)) = 0 \tag{4.7}$$

Solving for the amplitude of the received waveform, A , results in

$$\hat{a}_{ml}(R) = \frac{\sum_{k=1}^K [d_k - B]p_k(R)}{\sum_{k=1}^K p_k^2(R)}. \tag{4.8}$$

One important observation of the Equation (4.8) is its dependence on range. For each pixel, the amplitude estimation process consists of selecting a candidate range R in p_k and stepping through each time sample to determine the maximum likelihood solution for A . Using this amplitude estimate, the only other unknown for a given pixel is the target range. Finding a similar closed form solution for a range estimate is troublesome due to the range term residing in the exponential. Hence, finding the maximum of the distribution with

respect to range by

$$\hat{r}_{ml} = \arg \max_R L \quad (4.9)$$

is mathematically equivalent to using the amplitude estimate to calculate the values for L in Equation (4.4) for each candidate range and selecting the range that corresponds to the largest L value. This range serves as the estimated range for that pixel. The algorithm for estimating the range in each pixel is thus:

- 1) Select pixel location (x, y)
- 2) Select candidate range
- 3) Estimate waveform amplitude, A
- 4) Using the candidate range and amplitude estimate, calculate L
- 5) Repeat Steps 2-4 until all candidate ranges have been tested
- 6) Select the range that corresponds to the maximum L value
- 7) Go back to Step 1 for all pixels in detector array.

4.3 Normalized Cross-Correlation

In order to mitigate inter-sample targets, scaling, and waveform truncation issues, sub-sample ranging is performed on a pixel's pulse-shape $p_k(m, n)$ (e.g. Equation (2.72) or (2.73)) by using a normalized cross-correlation (NCC) method based on the Pearson product-moment correlation coefficient. Using this coefficient forces each pixel's waveform to be zero mean and unit standard deviation. A symmetrical waveform is assumed for notation simplicity. However, an asymmetrical waveform method could be implemented. The correlation matrix would then be increased by one dimension due to breaking up the pulse-width standard deviation into two variables: leading and trailing.

Analogous to a cross-correlation range estimator in [63], the normalized cross-correlation method is constructed as follows: The range vector of samples within a cube is represented by

$$R(k) = z_{\min} + z_{\text{inc}}(k) \quad (4.10)$$

where $k \in [0, \dots, K - 1]$, K is total number of samples (same K as defined in the data model in Section 2.5), z_{\min} is the range of the first sample, and z_{inc} is the range increment per sample. Another range vector, K_r is constructed with the same maximum and minimum extents as R , but with a smaller range increment per sample defined by the following equation:

$$K_r(q) = z_{\min} + z_f(q) \quad (4.11)$$

where $q \in [0, K' - 1]$, K' is the number of samples in K_r , and z_f is the range increment. Since the extents of K_r match R , the following inequalities hold: $K' > K$ and $z_f < z_{\text{inc}}$. A 2D reference Gaussian waveform matrix is used with the K_r vector as the reference target location or

$$r_k(q) = \exp \left\{ \frac{-(t_k - 2K_r(q)/c)^2}{2\sigma_w^2} \right\} \quad (4.12)$$

where $t_k = 2R(k)/c$ and is the time vector, $R(k)$ is the range vector from Equation (4.10), c is the speed of light in vacuum, and σ_w is the transmitted pulse standard deviation. The zero mean and unit variance version of r_k for all $k \in [1, \dots, K]$ and $q \in [1, \dots, K']$ is

$$S_2(k, q) = \frac{r_k(q) - \bar{r}_k(q)}{\sigma_r^2(q)} \quad (4.13)$$

where σ_r^2 and \bar{r}_k are the variance and average of r_k in the time dimension. Considering the range estimate for the $(m, n)^{\text{th}}$ pixel, the zero mean and unit variance version of the pulse-shape of interest $p_k(m, n)$ for all $k \in [1, \dots, K]$ is

$$S_1(k) = \frac{p_k(m, n) - \frac{\sum_{k=1}^K p_k(m, n)}{K}}{\sigma_p^2(m, n)} \quad (4.14)$$

where σ_p^2 is the variance of $p_k(m, n)$ in the time dimension respectively. With S_1 and S_2 determined, the normalized cross correlation denoted by \star is performed by

$$C_{K_r} = \frac{S_2 \star S_1}{K'}. \quad (4.15)$$

The cross correlation \star operation is carried out using a matrix multiply given by

$$S_2 \star S_1 = (S_2)^T \times S_1 \quad (4.16)$$

where S_2 and S_1 have dimensions $[K, K']$ and $[K]$ respectively, “ T ” is the transpose operator, and \times is a matrix multiply. The result of the matrix multiply is a vector of values C_{K_r} with dimension $[K']$ that correspond to the strength of the similarity between the reference waveform S_2 at different target ranges and the data waveform S_1 . Finding the range estimate is accomplished by peak detection (i.e. selecting the target range with the highest value from the matrix multiply) on C_{K_r} or

$$\hat{R}(m, n) = \arg \max_{z_{min} + z_r(q)} C_{K_r}(q). \quad (4.17)$$

The NCC method is used exclusively in Chapter V.

4.4 Two Point Target Range and Spatial Separation Estimator

With FOliage PENetration (FOPEN) applications, this section develops a range separation estimator by using a least squares approach adapted from previous work that only considered two targets within a single pixel in a non-blurry environment [5]. While no noise source is specified in the subsequent development, estimator results in a shot-noise limited environment are given in Section 6.2.

4.4.1 Two Point Target Data Model. The mean of the observations in units of photons of a two point target scene interrogated by a 3D FLASH LADAR are defined by a convolution between the object and the system point-spread-function (PSF) added to a pixel bias or [25], [37]

$$i_k(x, y) = \sum_{m=1}^M \sum_{n=1}^N o_k(m, n) h((x - m, y - n) + B(x, y)) \quad (4.18)$$

where (x, y) are the pixel plane coordinates with $x \in [1, X]$ and $y \in [1, Y]$, k is the range dimension coordinate, and (m, n) are the object plane coordinates with $m \in [1, M]$ and $n \in [1, N]$. The integer range dimension variable $k \in [0, K - 1]$ corresponds to a range distance r_k in units of meters according to

$$r_k = K_s + \left(\frac{k \cdot t_s \cdot c}{2} \right) \quad (4.19)$$

with K_s being the initial/starting range of the data cube, t_s as the range sampling interval in seconds, and c being the speed of light in meters per second.

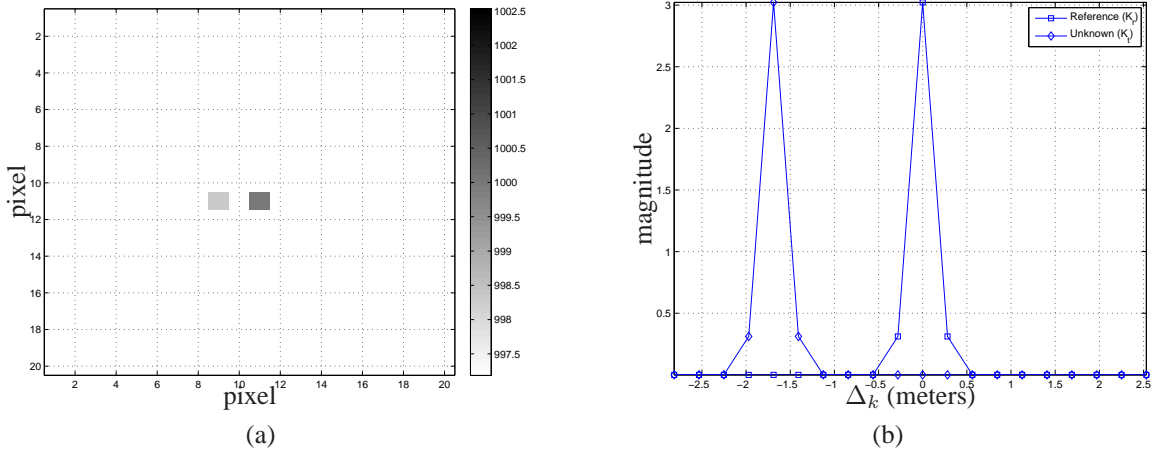


Figure 4.1: (a) For illustrative purposes, this figure is a range image of the truth data where the reference target is in the center of the array at 1000 meters with the unknown target placed at $\Delta_m = 2$ pixels and $\Delta_k = 1.7$ meters. (b) Defined by Equation (4.22), this shows the ideal waveforms of the unknown $p(r_k - K_t)$ and reference target $p(r_k - K_r)$ from Figure 4.1(a) with a pulse-width standard deviation $\sigma_{pt} = 0.88$ ns.

Considering both range and spatial dimensions, the two point target scene consists of one target at a known position and one target at an unknown position. The targets are constructed this way since the paper's focus is on range separation between the targets and not absolute range. This assumption keeps the parameter of interest (range separation) intact while simplifying the data model by preventing an additional unknown parameter. The targets are considered point targets spatially, but do provide a returned waveform. Considering the two point target scene illustrated by Figures 4.1(a) and (b), the object $o_k(x, y)$ is

defined by

$$o_k(m, n) = A_t p(r_k - (K_r - \Delta_k)) \delta(m - \Delta_m, n) + A_r p(r_k - K_r) \delta(m, n). \quad (4.20)$$

where A_t and A_r are the point target amplitudes, $p(r_k - (K_r - \Delta_k))$ and $p(r_k - K_r)$ are the received pulse shapes with K_r as the known reference target and Δ_k as the range separation between the known and unknown target (K_t) or $\Delta_k = K_r - K_t$. While the range sampling capability r_k of the LADAR is fixed by the receiver electronics, the unknown target K_t could occur anywhere within the range gate to include ranges between samples. Also, the spatial point targets are defined by Kronecker delta functions $\delta(m - \Delta_m, n)$ and $\delta(m, n)$ and $h(x, y)$ is the known system PSF. The final term is the pixel bias $B(x, y)$ and is intended to account for any ambient light, dark current, electron noise, and pixel-to-pixel impulse response variations. This bias is assumed known and to be governed by the Poisson distribution due to the discrete, random nature of these noise sources. Concerning the validity of the assuming a known pixel bias, it is target independent and can be separately determined during LADAR operation by a calibration step where the data is collected without activating the laser.

Performing the convolution in Equation (4.18) results in the simplified form

$$i_k(x, y) = A_t p(r_k - (K_r - \Delta_k)) h(x - \Delta_m, y) + A_r p(r_k - K_r) h(x, y) + B(x, y) \quad (4.21)$$

where the received pulse shapes are assumed symmetric Gaussian and defined by

$$p(r_k) = \frac{1}{\sqrt{2\pi}\sigma_{pd}} \exp\left\{\frac{-(r_k)^2}{2\sigma_{pd}^2}\right\} \quad (4.22)$$

with σ_{pd} as the pulse-width standard deviation in units of meters and defined as $\sigma_{pd} = c\sigma_{pt}/2$ where σ_{pt} is the pulse-width standard deviation in units of seconds. Gaussian-shaped pulses are a valid approximation for the pulse shapes transmitted from 3D FLASH LADAR hardware [39]. After analysis on experimental data, it was also found that the received pulse-shapes display an inherent asymmetry. In other words, the pulse-shape

definition is changed such that there are two pulse-shape standard deviations concerning Equation (4.22): one for the leading edge (pre-target) and another for the trailing edge (post-target). Although the effects of asymmetrical pulses on the CRB and range separation estimation is a source of additional research, the symmetry or lack thereof in the received pulses does not change the conclusion that an optimal pulse exists given the range resolution metric. Symmetrical pulse-shapes are assumed for simplicity and are simply a subset of asymmetrical pulse-shapes.

Furthermore, a spatially, invariant 2D Gaussian PSF is chosen because its differentiation is straight-forward while still providing a function to sufficiently blur a target scene. This type of impulse response has been used previously to describe blurring due to atmospheric turbulence [37]. The PSF is defined as

$$h(x, y) = \frac{1}{2\pi\sigma_h^2} \exp\left\{\frac{-(x^2 + y^2)}{2\sigma_h^2}\right\} \quad (4.23)$$

where $\sigma_h > 0$ is the PSF standard deviation (measured in units of pixels) and is affected by light diffraction effects, receiver optic's quality, and atmospheric turbulence.

4.4.2 Estimator Derivation. Given the variable definitions from Equations (4.18)-(4.23), the sum squared error term is the sum of the square of the difference between the observed data and the estimate or

$$E(\Delta_k) = \sum_k \sum_x \sum_y (d_k(x, y) - i_k(x, y))^2 \quad (4.24)$$

where the dependence on Δ_k will subsequently be dropped for conciseness. There are four unknowns including the two amplitudes, range separation, and spatial separation. The procedure to find the range and spatial separation estimates is to iteratively step through each possible combination of range and spatial separation values (these values are known a priori) and then determine the amplitudes that minimize the error. After an exhaustive search of combinations of range and spatial separations, the combination that results in the least sum square error is chosen as the estimates.

For a particular amplitude A_i , the approach is to take the derivative of the error (Equation (4.24)) with respect to that amplitude, set the result equal to zero, $\partial E/\partial A_i = 0$, and solve for the amplitude term. This method gives the amplitude value that minimizes the error term due to the positivity of the second derivative. Since there are two amplitudes, a well-posed system of equations is set up by performing $\partial E/\partial A_t = 0$ and $\partial E/\partial A_r = 0$ and solving for A_t and A_r respectively resulting in two equations and two unknowns shown by

$$\begin{aligned} C_{11}A_t + C_{12}A_r &= D_1 \\ C_{21}A_t + C_{22}A_r &= D_2 \end{aligned} \quad (4.25)$$

where

$$\begin{aligned} C_{11} &= \sum_k \sum_x \sum_y - [p(k - (K_r - \Delta_k)) h(x - \Delta_m, y)]^2 \\ C_{12} &= C_{21} = \sum_k \sum_x \sum_y -p(k - (K_r - \Delta_k)) h(x - \Delta_m, y) p(k - K_r) h(x, y) \\ C_{22} &= \sum_k \sum_x \sum_y - [p(k - K_r) h(x, y)]^2 \\ D_1 &= \sum_k \sum_x \sum_y (B(x, y) - d_k(x, y)) p(k - (K_r - \Delta_k)) h(x - \Delta_m, y) \\ D_2 &= \sum_k \sum_x \sum_y (B(x, y) - d_k(x, y)) p(k - K_r) h(x, y). \end{aligned} \quad (4.26)$$

The amplitudes are then determined by solving the system of equations.

The following provides the estimation steps:

1. Select a range separation, Δ_k
2. Select a spatial separation, Δ_m
3. Determine the estimates for amplitudes, A_t and A_r , via the system of equations in (4.25)
4. Calculate error term using Equation (4.24)
5. Repeat steps 1-4 until all range and spatial separations have been selected

6. Select range and spatial separation corresponding to the smallest error

4.5 Pixel-Dependent Two Surface Range Separation Estimator

The purpose of this estimator is to be able to estimate the range to two surfaces within a single pixel. Similar to [5], this scenario differs in that the first surface in range is known while the second surface, further in range, is unknown. Further, unlike the previous section where the data model includes all pixels and range samples, this estimator operates on one pixel at a time. Section 6.3.2 uses this estimator against a complex, two surface target to find the optimal pulse-width with respect to range resolution.

The data model for an arbitrary pixel is

$$d_k = i_k + n_k \quad (4.27)$$

where d_k is the observed data, i_k is the blurry, non-noisy data, and n_k is the noise. Since a pixel can follow more than one data model, hypothesis testing is performed to decide whether there is one or two surfaces in the pixel. In a two surface target scene, a particular pixel might contain one or two surfaces. Therefore, the blurry, non-noisy data is hypothesized to be either a “two surface pixel” by

$$i_k = A_t p(k - K_t) + A_r p(k - K_r) + B \quad (4.28)$$

or “one surface pixel” by

$$i_k = A_g p(k - K_g) + B. \quad (4.29)$$

where A_t and A_r are the received target amplitudes (includes convolution effects), $p(k)$ is the received pulse with K_t as the unknown, second-surface target range and K_r as the known, first-surface target range, and B as the pixel bias term. Note, either the first OR second surface can be represented by the “one surface pixel” (Equation (4.29)) case where A_g and K_g are generic variables representing either surfaces particular amplitude and range respectively. The unknown target range K_t can also be defined by a range separation Δ_k

from the known target K_r by $K_t = K_r - \Delta_k$. The terms that must be estimated (i.e. the unknowns) are A_t , A_r (if “two surface pixel”), and Δ_k .

Regardless of the number of surfaces in the pixel, the sum squared error metric is the same ($E_1(\Delta_k)$ and $E_2(\Delta_k)$ for a “one surface pixel” or a “two surface pixel” respectively) and is defined as

$$E(\Delta_k) = \sum_k (d_k - i_k)^2 \quad (4.30)$$

which is similar to the previous previous section with the exception that the pixel detector dimensions are dropped. The procedure to estimate the unknown parameter of interest, range separation Δ_k , is to estimate the range separation using both “one surface pixel” and “two surface pixel” data models and choose the “one surface pixel” case and corresponding range separation estimate if

$$\frac{E_1^{\min}}{E_2^{\min}} < \gamma \quad (4.31)$$

where γ is a threshold, $E_1^{\min} = \arg \max_{\Delta_k} E_1(\Delta_k)$, and $E_2^{\min} = \arg \max_{\Delta_k} E_2(\Delta_k)$. If the inequality in Equation (4.31) is not true, then choose the “two surface pixel” case and its range separation estimate.

The amplitude and range estimate on the “one surface” data model are attained by selecting a candidate range separation and then taking $\partial E_1 / \partial A_t = 0$ and then solving for A_t given by

$$A_t = \frac{\sum_{k=1}^K \{d_k p(k - K_t) - B p(k - K_t)\}}{\sum_{k=1}^K p(k - K_t)^2}. \quad (4.32)$$

The “two surface” amplitude estimates are determined in the same manner as the previous sections using Equations (4.25) and (4.26) and dropping the pixel dimension (x and y) summations.

The steps of the estimator are:

1. Select a range separation, Δ_k

2. Determine the amplitude estimates for the “two surface pixel” case via Equations (4.25) and (4.26)
3. Determine the amplitude estimate for the “one surface pixel” case via Equation (4.32).
4. Calculate error terms E_1 and E_2 using Equation (4.30)
5. Repeat steps 1-4 until all range separations have been selected
6. Using the hypothesis test from Equation (4.31), select the range separation corresponding to the smallest error. The range separation for the pixel may be zero if the “one surface pixel” case is chosen and if the pixel is a “first surface pixel” as well with a known range of K_r .

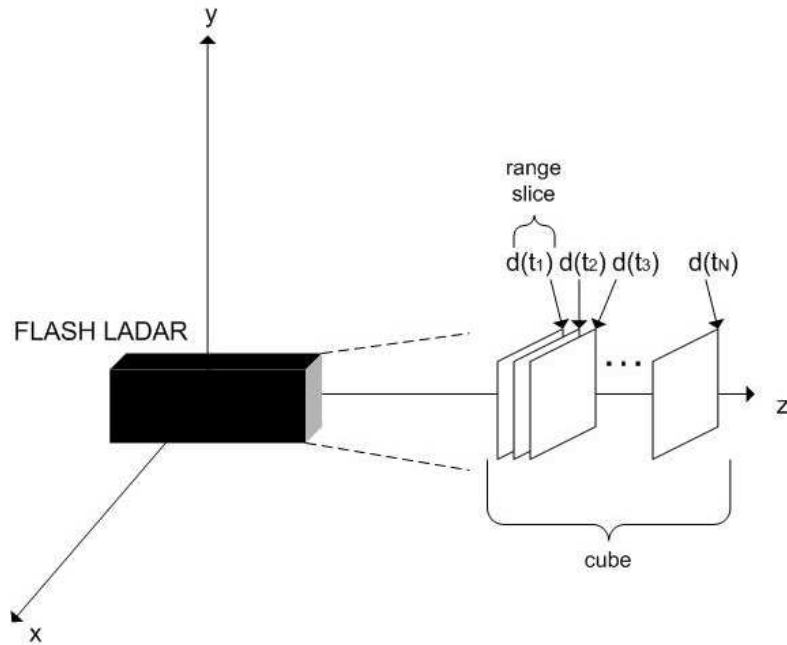
V. Improving 3D FLASH LADAR Range Estimation via Object Recovery

The motivation in this chapter is to provide a means of improving range estimation by object recovery (i.e. spatially deblurring data) from three dimensional FLASH LAsER Detection And Ranging (3D FLASH LADAR) observations. Referring to Figure 5.1(a), the idea is to process the data in the spatial dimensions (x, y) while improving ranging performance in the time dimension (k) . Taken exclusively from [56], this chapter covers novel material including amplitude, pulse-shape, system impulse response, and pixel bias estimation. Original efforts also include object, system impulse response, and pixel bias estimation.

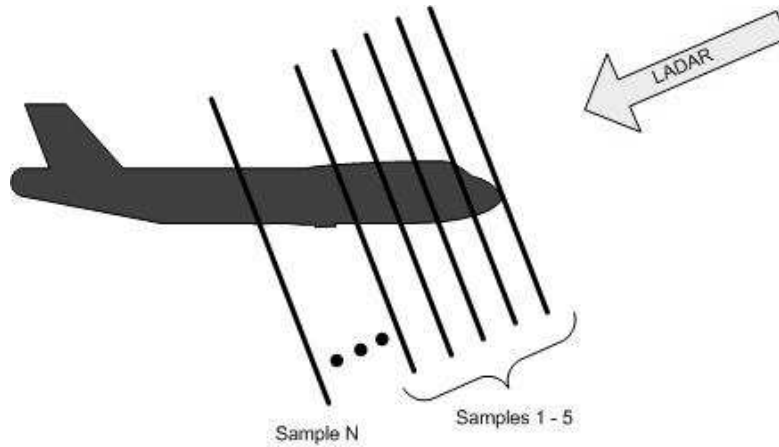
Building on material presented in Chapters II and III, a method to model the 3D FLASH LADAR data operating in “sular mode” is that the 2D range images are formed via a convolution between the object at a particular time and the spatial impulse response. In Figure 5.1(a), a range image $d(t_k)$ is one of the 2D slices of the data cube. Considering the laser illuminating a target, one collect from a 3D FLASH LADAR sensor results in a data cube consisting of a series of range images (N from Figure 5.1) representing detected photons. (NOTE: Figure 5.1 is shown again for convenience.)

Attempts at 3D FLASH LADAR range estimation of a remote scene can result in errors due to several factors including the optical spatial impulse response, detector blurring, photon noise, timing jitter, and readout noise. These factors either cause the scene’s intensity to spread across pixels or add unwanted and disruptive noise effects. The intensity spreading and noise corrupt the correct pixel intensities by mixing intensities with neighboring pixels thereby providing false intensity values and therefore incorrect photon counts to the range estimator. Without blur and noise compensation, the range estimates would be inaccurate to a degree depending on the blur and noise severity.

The theoretical development of the range estimator algorithm is covered first and then verified using simulation and experimental results. The algorithm is a variation on the Expectation Maximization (EM) algorithm called Generalized Expectation Maximization (GEM) and is desirable due to its iterative likelihood maximization, convergence proper-



(a)



(b)

Figure 5.1: (a) 3D view of LADAR system model in Cartesian coordinates with each data cube having dimensions of pixel \times pixel \times time sample. The variable $d(t_k)$ corresponds to the k^{th} receiver detected range image with $k \in [1, N]$. (b) Another view of the 3D FLASH LADAR operation. Each range image's full field of view (FOV) is 128×128 pixels with a range gate near 2 nanoseconds corresponding to the 3D FLASH LADAR system used for experimental collects.

ties, and ability to decouple terms [54]. The GEM algorithm is powerful in that it can perform blind deconvolution in situations with severe defocus or other aberrations including atmospheric turbulence. To account for different scenarios, two versions of the GEM algorithm are derived that either recover the *pulse-shape* or the *object*. The primary difference between the two involves data required and accuracy. *Pulse-shape* estimation requires less data, but is less accurate than *object* estimation. Additional details of the differences are presented in Sections 5.1.2 and 5.1.3. Both pulse-shape and object GEM algorithms are novel contributions to the research area.

In addition to the GEM algorithms, a Wiener filter method is used to attempt range estimation improvement via object recovery from 3D FLASH LADAR observations [37], [55]. Requiring spatial impulse response knowledge a priori, this method can only perform deconvolution unlike the blind deconvolution ability of the GEM. The purpose for adding this other method is to show that the GEM outperforms a competing algorithm that already knows part of the answer (spatial impulse response).

This chapter is organized as follows: Section 5.1 describes the Wiener filter theory and derives the pulse and object iterative estimators via the GEM algorithm, Section 5.2 presents results from simulated data showing improvement in range estimation after object recovery, Section 5.3 details the results from an experimental collection and processing also showing an improvement in range estimation after object recovery, and Section 5.4 provides conclusions based on observed results.

5.1 Theoretical Development

This section details the object recovery methods used on simulated and experimental data. Even though the laser light is partially coherent, the argument is made that the detected light is able to be modeled as fully incoherent. The incoherent light model still captures the discrete, non-negative nature of the received photons that the partially coherent model exhibits. In addition, experimental data processing from Section 3.6 showed that the speckle parameter estimation results tend towards the incoherent model. Consequently, this incoherent light model assumption allows for the returns to be a result of a linear,

spatially invariant (LSI) system involving an intensity convolution (instead of amplitude convolution) between the intensity point spread function and the remote scene. Linearity is a consequence of electromagnetic wave propagation theory, and spatial invariance results from remaining with the isoplanatic angle [25]. Utilizing this LSI convolution model, two GEM blind deconvolution algorithms are derived that enable improved range estimation. All references to the scenario or data model refer to material presented in Section 2.5.

The unknown parameters in this scenario are the object (target amplitude and target range) PSF, and bias. The variable of interest in this paper is the range term residing in Equation (2.72) or (2.73). Direct estimation of the range term is problematic because of its location either in an exponential or in a squared term. Therefore, the approach to range estimation is to retrieve the range from the estimated pulse-shape or object. This methodology relies on the knowledge that the target produces the waveform peak in the detected returns. Concerning the PSF, blind deconvolution techniques must be employed since the PSF is unknown. Blind deconvolution has a rich heritage in astronomical imaging providing a bevy of literature attempting blind deconvolution. Although, blind deconvolution in astronomical cases consists of trying to recover one object and one PSF (or many PSFs if using multiple frames). In trying to recover the target range from one 3D FLASH LADAR data collect, this problem consists of many objects with one PSF. There are many objects due to the transmitted waveform causing each range slice to contain different intensities corresponding to where the waveform is incident on the object. Therefore, these incident points become distinct objects in the blind deconvolution framework. If multiple cubes are necessary, the atmosphere is changing with each cube resulting in multiple PSFs that must be estimated resulting in a “multi-frame” or “multi-cube” scenario. If no atmospheric turbulence exists or is non-volatile, the PSF is consistent throughout the cubes and the j subscript can be dropped.

5.1.1 Object Deconvolution. As noted previously, the goal of this research effort is to improve range estimation of a target illuminated by a 3D FLASH LADAR. Deconvolution is necessary due to the imaging nature of the 3D LADAR producing blurred return

pulses. A solution is to use image restoration techniques to attempt to restore the original range slice images thereby improving the range estimation. The image restoration algorithm applies a 2-D filter to the a pixel detector array at each time sample (i.e. range slice image, etc.) resulting in a “de-blurred” data cube. The “de-blurred” data cube’s pixels now more closely mimic the unblurred return pulse from Equation (2.72) and result in improved range estimation.

A standard linear filter that can perform the image restoration is the pseudo-inverse Wiener filter. From [37], the definition of the pseudo-inverse Wiener filter, $G_W(f_x, f_y)$, is

$$G_W(f_x, f_y) = \frac{H^*(f_x, f_y)}{|H(f_x, f_y)|^2 + \frac{1}{SNR}} \quad (5.1)$$

where $H(f_x, f_y)$ is the overall optical transfer function (OTF), $*$ is the conjugate operator, and SNR is the signal-to-noise ratio in the image. One image processing definition of the SNR is to set it equal to the image mean divided by the image standard deviation [70]. Given that the signal is dominated by shot noise, the SNR is defined at particular range sample k to be the mean of the detected range image μ_d divided by the detected range image standard deviation $\sqrt{\mu_d}$ or

$$SNR = \sqrt{\mu_d}. \quad (5.2)$$

Using the pseudo-inverse Wiener filter, the deblurred image at a particular range sample k is

$$\hat{I}_k(x, y) = F^{-1} \{G_W(f_x, f_y) D_k(f_x, f_y)\} \quad (5.3)$$

with F^{-1} as the inverse Fourier transform and $D_k(f_x, f_y)$ is the Fourier transform of the detected range image $d_k(x, y)$. After the cube has been filtered, the normalized cross-correlation (NCC) range estimator method uses the filtered data to determine the range estimate using Equation (4.17). The waveform variable $p_k(m, n)$ in Equation (4.14) is replaced by $\hat{I}_k(x, y)$ during the NCC implementation.

5.1.2 Pulse-Shape Blind Deconvolution via the GEM Algorithm. The previous section assumed a known PSF. This section covers the blind deconvolution case where the

PSF is unknown. Blind object recovery is accomplished using two approaches concerning the pulse-shape and object variables from Equation (2.72). The pulse-shape estimation is very powerful in that the estimator only needs *one* data cube (one-shot, one-kill). However, if the best accuracy is required and the 3D data cubes are properly registered, the multi-cube object estimation provides lower error.

Referring to the GEM theory from Section 2.4 and the data model from Section 2.5, the model is reformed to consider pulse-shape recovery with one cube required for processing (with $j = 1$). Consistent with the GEM algorithm, the original data $d_k(x, y)$ is called the incomplete data and is defined by [54]

$$d_k(x, y) = \sum_{m=1}^M \sum_{n=1}^N \tilde{d}_k(x, y|m, n) + \tilde{q}_k(x, y) \quad (5.4)$$

where two new variables, $\tilde{d}_k(x, y|m, n)$ and $\tilde{q}_k(x, y)$, are called complete data. This formulation provides two sets of complete data that account for the photon noise/image formation and pixel bias respectively. The formation of the complete data highlights the powerful nature of the GEM algorithm. In this application, complete data can also be called unobserved data and carries no explicit physical meaning. It is used to directly benefit the EM algorithm. Consistent with [71], careful definition of the complete data allows decoupling of unknown variables while preserving physical meaning in the expected value of the incomplete data.

The expected value of the complete data sets is given by

$$E \left[\tilde{d}_k(x, y|m, n) \right] = A(m, n) p_k(m, n) h(x - m, y - n). \quad (5.5)$$

and

$$E [\tilde{q}_k(x, y)] = B(x, y) \quad (5.6)$$

where $B(x, y)$ is the constant pixel bias. The expected value of the incomplete data is thus

$$E [d_k(x, y)] = i_k(x, y) + B(x, y) \quad (5.7)$$

which is consistent with the data observations depicted in the high fidelity model (i.e. convolution model) of Figure 2.4. Adding the pixel bias to the model covers non-modeled noise effects and pixel-to-pixel impulse response variations. The pixel bias is assumed to be governed by the Poisson distribution due to the discrete random nature of dark current and electron noise. Physically, the pixel bias is added to the photons incident upon the detector and is part of the detected photon counts. The PMF for the photon noise is

$$P\left(\tilde{d}_k(x, y|m, n)\right) = \frac{[A(m, n) p_k(m, n) h(x - m, y - n)]^{\tilde{d}_k(x, y)} e^{-[A(m, n) p_k(m, n) h(x - m, y - n)]}}{\tilde{d}_k(x, y)!} \quad (5.8)$$

while the PMF for the pixel bias is

$$P\left(\tilde{q}_k(x, y)\right) = \frac{B(x, y)^{\tilde{q}_k(x, y)} e^{-B(x, y)}}{\tilde{q}_k(x, y)!}. \quad (5.9)$$

Assuming statistical independence between all the pixels and between the photon noise and pixel bias noise, the complete data log-likelihood function considering all random variables is

$$L_{CD}(p_k, A, h, B) = \ln \left[\prod_{k, x, y, m, n} P\left(\tilde{d}_k(x, y|m, n)\right) P\left(\tilde{q}_k(x, y)\right) \right] \quad (5.10)$$

or (NOTE: summations wrap around unless otherwise stated)

$$L_{CD}(p_k, A, h, B) = \sum_{k, x, y, m, n} \tilde{d}_k(x, y|m, n) \ln [A(m, n) p_k(m, n) h(x - m, y - n)] - [A(m, n) p_k(m, n) h(x - m, y - n)] + \tilde{q}_k(x, y) \ln [B(x, y)] - B(x, y). \quad (5.11)$$

Referring to Equation (2.64), the Q function then becomes

$$Q(p_k, A, h, B) = E \left[L_{CD}(p_k, A, h, B) | d_k(x, y), p_k^{old}, A^{old}, h^{old}, B^{old} \right] \quad (5.12)$$

where the estimates for the amplitude, pulse-shape, PSF, and bias are considered maximum-likelihood estimates. Taking the conditional expectation of Equation (5.12) results in

$$\begin{aligned}
Q(p_k, A, h, B) = & \\
& \sum_{k,x,y,m,n} \mu_{\tilde{d}_k}^{old}(x, y, m, n; A^{old}, p_k^{old}, h^{old}) \ln [A(m, n) p_k(m, n) h(x - m, y - n)] \\
& - [A(m, n) p_k(m, n) h(x - m, y - n)] + \mu_{\tilde{q}}^{old}(x, y; B^{old}) \ln [B(x, y)] \\
& - B(x, y)
\end{aligned} \tag{5.13}$$

where

$$\mu_{\tilde{d}_k}^{old}(x, y, m, n; p_k^{old}, A^{old}, h^{old}) = E \left[\tilde{d}_k(x, y | m, n) | d_k(x, y), p_k^{old}, A^{old}, h^{old} \right] \tag{5.14}$$

and

$$\mu_{\tilde{q}_k}^{old}(x, y; B^{old}) = E \left[\tilde{q}_k(x, y) | d_k(x, y), B^{old} \right]. \tag{5.15}$$

Equations (5.14) and (5.15) represent the expected value of one set of complete data given the incomplete data. For Poisson random variables, these expectations turn out to be ratios of the data times one expected value of the complete data divided by the all sets of expected values of the complete data [75]. For the first set of complete data, $\tilde{d}_k(x, y)$, the conditional expectation is

$$\mu_{\tilde{d}_k}^{old}(x, y, m, n; p_k^{old}, A^{old}, h^{old}) = \frac{d_k(x, y) A^{old}(m, n) p_k^{old}(m, n) h^{old}(x - m, y - n)}{i_k^{old}(x, y) + B^{old}(x, y)}, \tag{5.16}$$

while the second set of complete data concerning the pixel bias $\tilde{q}_k(x, y)$, has a conditional expectation equal to

$$\mu_{\tilde{q}_k}^{old}(x, y; B^{old}) = \frac{d_k(x, y) B^{old}(x, y)}{i_k^{old}(x, y) + B^{old}(x, y)}. \tag{5.17}$$

The maximization of the Q function for all parameter unknowns (target amplitude, target pulse shape, PSF, and pixel bias) is theoretically intractable due to coupling. It is required

to break apart the Q function into separate components such that

$$Q = Q_p + Q_h + Q_A + Q_B \quad (5.18)$$

where each component of the Q function can be maximized independently. Thus, the GEM algorithm becomes

$$\begin{aligned} Q_p(p_k^{new}|p_k^{old}, A^{old}, h^{old}) &\geq Q_p(p_k^{old}|p_k^{old}, A^{old}, h^{old}) \\ Q_A(A^{new}|p_k^{old}, A^{old}, h^{old}) &\geq Q_A(A^{old}|p_k^{old}, A^{old}, h^{old}) \\ Q_h(h^{new}|p_k^{old}, A^{old}, h^{old}) &\geq Q_h(h^{old}|p_k^{old}, A^{old}, h^{old}) \\ Q_B(B^{new}|B^{old}) &\geq Q_B(B^{old}|B^{old}) \end{aligned} \quad (5.19)$$

which, if these conditions are met, ensures that the likelihood is increased with each iteration [54]

$$L(p_k^{new}, A^{new}, h^{new}, B^{new}) \geq L(p_k^{old}, A^{old}, h^{old}, B^{old}) \quad (5.20)$$

resulting in a GEM sequence converging to a local maximum.

Beginning the estimation process of the separate Q functions starts with the target pulse shape, Q_p which is

$$Q_p = \sum_{k,x,y,m,n} \mu_{d_k}^{old}(x, y, m, n; p_k^{old}, A^{old}, h^{old}) \ln [p_k(m, n)] - \lambda(m, n) \left[\sum_{k=1}^K p_k(m, n) - 1 \right] \quad (5.21)$$

where a pixel-dependent Lagrange multiplier, $\lambda(m, n)$, is introduced to force the pulse shape to add to one for each pixel. This constraint is necessary to decouple the pulse shape from the target amplitude and PSF. Taking the derivative of Equation (5.21) with respect to a particular object plane point and range sample, setting the result equal to zero,

$\partial Q_p / \partial p_{k_o}(m_o, n_o) = 0$, and solving for the pulse shape, results in

$$p_{k_o}^{new}(m_o, n_o) = p_{k_o}^{old}(m_o, n_o) \left(\frac{A^{old}(m_o, n_o)}{\lambda(m_o, n_o)} \right) \sum_{x=1}^X \sum_{y=1}^Y \frac{d_{k_o}(x, y) h^{old}(x - m_o, y - n_o)}{i_{k_o}^{old}(x, y) + B^{old}(x, y)} \quad (5.22)$$

where

$$\lambda(m_o, n_o) = A^{old}(m_o, n_o) \sum_{k=1}^K p_k^{old}(m_o, n_o) \sum_{x=1}^X \sum_{y=1}^Y \frac{d_k(x, y) h^{old}(x - m_o, y - n_o)}{i_k^{old}(x, y) + B^{old}(x, y)} \quad (5.23)$$

and

$$i_{k_o}^{old}(x, y) = \sum_{m=1}^M \sum_{n=1}^N A^{old}(m, n) p_{k_o}^{old}(m, n) h^{old}(x - m, y - n). \quad (5.24)$$

Equation (5.22) is the iterative solution for the pulse shape per range sample. Next, the Q function is partitioned into its target amplitude components

$$Q_A = \sum_{k,x,y,m,n} \left\{ \mu_{\tilde{d}_k}^{old}(x, y, m, n; p_k^{old}, A^{old}, h^{old}) \ln [A(m, n)] \right\} - \sum_{m=1}^M \sum_{n=1}^N A(m, n) \quad (5.25)$$

where

$$\sum_{x=1}^X \sum_{y=1}^Y h(x, y) = 1 \quad (5.26)$$

$$\sum_{k=1}^K p_k(m, n) = 1 \quad (5.27)$$

have been utilized to decouple the pulse shape and PSF terms from the target amplitude. Maximizing Equation (5.25) by $\partial Q_A / \partial A(m_o, n_o) = 0$ and solving for the amplitude term results in the iterative solution for the target amplitude term

$$A^{new}(m_o, n_o) = A^{old}(m_o, n_o) \sum_{k=1}^K p_k^{old}(m_o, n_o) \sum_{x=1}^X \sum_{y=1}^Y \frac{d_k(x, y) h^{old}(x - m_o, y - n_o)}{i_k^{old}(x, y) + B^{old}(x, y)}. \quad (5.28)$$

The PSF is the final unknown parameter that uses the first set of complete data, $\tilde{d}_k(x, y)$.

The Q function for the PSF is

$$Q_h = \sum_{k,x,y,m,n} \mu_{\tilde{d}_k}^{old}(x, y, m, n; p_k^{old}, A^{old}, h^{old}) \ln [h(x - m, y - n)] - [A(m, n) p_k(m, n) h(x - m, y - n)], \quad (5.29)$$

which still has the target amplitude and pulse shape terms. Similar to [71], a change of variables is required to remove the dependence on the pulse shape and to allow for easier differentiation. Utilizing $\sum_{k=1}^K p_k(m, n) = 1$ and setting $m' = x - m$ and $n' = y - n$, Q_h then becomes

$$Q_h = \sum_{k,x,y,m',n'} \left\{ \mu_{\tilde{d}_k}^{old}(x, y, x - m', y - n'; p_k^{old}, A^{old}, h^{old}) \ln [h(m', n')] \right\} - \sum_{x,y,m',n'} A(x - m', y - n') h(m', n'). \quad (5.30)$$

Setting $\partial Q_h / \partial h(m'_o, n'_o) = 0$ and solving for the PSF produces the iterative solution

$$h^{new}(m'_o, n'_o) = h^{old}(m'_o, n'_o) \sum_{k,x,y} \frac{d_k(x, y) A^{old}(x - m'_o, y - n'_o) p_k^{old}(x - m'_o, y - n'_o)}{(i_k^{old}(x, y) + B^{old}(x, y)) \sum_{x=1}^X \sum_{y=1}^Y A^{new}(x - m'_o, y - n'_o)}. \quad (5.31)$$

Usually, the target amplitude term in the denominator would be an issue because it is considered the new estimate. However, Equation (5.28) is the new estimate and can replace the target amplitude in the denominator resulting in a consistent solution for the PSF. Finally, the pixel bias must be estimated. In order to estimate the pixel bias, the second set of complete data, $\tilde{q}_k(x, y)$, is utilized. The Q function for the pixel bias is

$$Q_B = \sum_{k=1}^K \sum_{x=1}^X \sum_{y=1}^Y \frac{d_k(x, y) B^{old}(x, y)}{i_k^{old}(x, y) + B^{old}(x, y)} \ln (B(x, y)) - B(x, y). \quad (5.32)$$

Setting $\partial Q_B / \partial B(x_o, y_o) = 0$ and solving for the pixel bias results in an iterative solution

$$B^{new}(x_o, y_o) = B^{old}(x_o, y_o) \sum_{k=1}^K \frac{d_k(x_o, y_o)}{(i_k^{old}(x_o, y_o) + B^{old}(x_o, y_o))} \quad (5.33)$$

corresponding to the pixel bias iteration.

After a pre-determined number of iterations on Equations (5.22), (5.28), (5.31), and (5.33), range estimate updates for each pixel are generated by using the NCC method between a reference waveform at sub-sample ranges and the the GEM estimate for the pulse shape, p_k^{new} . The range-dependent reference waveform that results in the highest correlation is chosen and the corresponding range is the new range estimate for that pixel. The new range estimate is fed back into the pulse-shape to generate a new p_k^{old} followed by another set of GEM iterations. The process (GEM iterations followed by range updates) repeats with the new range estimates used in calculating p_k^{old} using Equation (5.22) and ceases when the mean square error (MSE) between the data and non-noisy range images reaches the stopping criteria. All previous amplitude, PSF, and pixel bias estimates carry over from one range update to the next. More specifically, iterations cease when the MSE is lower than the average data variance or

$$\sum_{k=1}^K \sum_{x=1}^X \sum_{y=1}^Y (d_{jk}(x, y) - I_k^{est}(x, y) - B^{new}(x, y))^2 < \sum_{k=1}^K \sum_{x=1}^X \sum_{y=1}^Y V_k(x, y) \quad (5.34)$$

with

$$I_k^{est}(x, y) = \sum_{m=1}^M \sum_{n=1}^N A^{new}(m, n) p_k^{new}(m, n) h^{new}(x - m, y - n) \quad (5.35)$$

and

$$V_k(x, y) = \sum_{j=1}^J \left(d_{jk}(x, y) - \frac{\sum_{j_2=1}^J d_{j_2k}(x, y)}{J} \right)^2 \quad (5.36)$$

where V_k is the variance for the volume elements (voxels). In the experimental data, a specific distribution for the variance is not chosen in order to account for all noise sources. For the simulation data, the primary noise source is defined explicitly by the Poisson distribution. Therefore, data variance V_k is defined by the variance of the Poisson distribution (i.e. mean of the data).

In summary, the pulse-shape estimation algorithm steps are:

1. Initialize PSF, amplitude, and pixel bias
2. Determine initial ranges and define pulse-shape
3. Perform GEM iterations using Equations (5.22), (5.28), (5.31), and (5.33)
4. Use NCC to find new range estimates with Equation (4.17)
5. Generate new pulse-shapes based on new ranges
6. Determine MSE and compare to stopping criteria
7. Repeat Steps 3 through 6 until stopping criteria violated
8. Range estimates taken from last execution of Step 4

In step one, the PSF is initialized by the diffraction-limited PSF of the system with some defocus to allow the iterations the freedom to modify the estimate. The amplitudes and the pixel bias are initialized by a matrix of ones.

5.1.3 Object Blind Deconvolution via the GEM Algorithm. When multiple cubes are available and properly registered spatially and temporally, another method to perform range estimation is to relax the constraint on the pulse-shape and assume just an object in the data model. This change mitigates the issue in the hardware data where the pulse-shape is vaguely known. Therefore, estimation is performed on o_k rather than on p_k from Equation (2.71). The problem setup is similar to the pulse-shape estimation (now with more than one cube) by calling the original data, $d_{jk}(x, y)$, the incomplete data and specifying

$$d_{jk}(x, y) = \sum_{m=1}^M \sum_{n=1}^N \tilde{d}_{jk}(x, y|m, n) + \tilde{q}_{jk}(x, y) \quad (5.37)$$

where two new variables, $\tilde{d}_{jk}(x, y|m, n)$ and $\tilde{q}_{jk}(x, y)$, are defined and called complete data. This formulation provides two sets of complete data that account for the image formation and pixel bias respectively. The same PSF can be assumed for adjacent collections due to a typical data collection scenario where environments shouldn't be changing rapidly (ignore j). Thus, the expected values of the complete data sets are given by

$$E \left[\tilde{d}_{jk}(x, y|m, n) \right] = o_k(m, n) h(x - m, y - n) \quad (5.38)$$

and

$$E [\tilde{q}_{jk}(x, y)] = B(x, y) \quad (5.39)$$

where $B(x, y)$ is the constant pixel bias. The expected value of the incomplete data is thus

$$E [d_{jk}(x, y)] = i_k(x, y) + B(x, y). \quad (5.40)$$

The PMF for the photon noise is

$$P \left(\tilde{d}_{jk}(x, y|m, n) \right) = \frac{[o_k(m, n) h(x - m, y - n)]^{\tilde{d}_{jk}(x, y|m, n)} \exp \{ -o_k(m, n) h(x - m, y - n) \}}{\tilde{d}_{jk}(x, y|m, n)!} \quad (5.41)$$

while the pixel bias PMF is

$$P (\tilde{q}_{jk}(x, y)) = \frac{B(x, y)^{\tilde{q}_{jk}(x, y)} e^{-B(x, y)}}{\tilde{q}_{jk}(x, y)!}. \quad (5.42)$$

Assuming statistical independence between all the pixels and between the photon noise and pixel bias noise, the complete data log-likelihood is then

$$L_{CD}(o_k, h, B) = \ln \left[\prod_{j, k, x, y, m, n} P \left(\tilde{d}_{jk}(x, y|m, n) \right) P \left(\tilde{q}_{jk}(x, y) \right) \right] \quad (5.43)$$

or

$$L_{CD}(o_k, h, B) = \sum_{j,k,x,y,m,n} \tilde{d}_{jk}(x, y|m, n) \ln [o_k(m, n) h(x - m, y - n)] \\ - [o_k(m, n) h(x - m, y - n)] + \tilde{q}_{jk}(x, y) \ln [B(x, y)] - B(x, y). \quad (5.44)$$

Referring to [54], the Q function becomes the expected value of the complete data log-likelihood function with respect to the incomplete data and old parameter estimates

$$Q(o_k, h, B) = E [L_{CD}(o_k, h, B) | d_{jk}(x, y), o_k^{old}, h^{old}, B^{old}]. \quad (5.45)$$

Taking the conditional expectation from Equation (5.45) results in

$$Q(o_k, h, B) = \sum_{j,k,x,y,m,n} \mu_{\tilde{d}_{jk}}^{old}(x, y, m, n; o_k^{old}, h^{old}) \ln [o_k(m, n) h(x - m, y - n)] \\ - [o_k(m, n) h(x - m, y - n)] + \mu_{\tilde{q}}^{old}(x, y; B^{old}) \ln [B(x, y)] - B(x, y) \quad (5.46)$$

where

$$\mu_{\tilde{d}_{jk}}^{old}(x, y, m, n; o_k^{old}, h^{old}) = E [\tilde{d}_{jk}(x, y|m, n) | d_{jk}(x, y), o_k^{old}, h^{old}] \\ = \frac{d_{jk}(x, y) o_k^{old}(m, n) h^{old}(x - m, y - n)}{i_k^{old}(x, y) + B^{old}(x, y)} \quad (5.47)$$

and

$$\mu_{\tilde{q}_{jk}}^{old}(x, y; B^{old}) = E [\tilde{q}_{jk}(x, y) | d_{jk}(x, y), B^{old}] \\ = \frac{d_{jk}(x, y) B^{old}(x, y)}{i_k^{old}(x, y) + B^{old}(x, y)}. \quad (5.48)$$

Similar to the pulse-shape estimation, the maximization of the Q function for all parameter unknowns (object, PSF, and pixel bias) is theoretically intractable due to coupling. It is

required to break apart the Q function into separate components such that

$$Q = Q_o + Q_h + Q_B \quad (5.49)$$

where each component of the Q function can be maximized independently. Thus, the GEM algorithm becomes

$$\begin{aligned} Q_o(o_k^{new}|o_k^{old}, h^{old}) &\geq Q_o(o_k^{old}|o_k^{old}, h^{old}) \\ Q_h(h^{new}|o_k^{old}, h^{old}) &\geq Q_h(h^{old}|o_k^{old}, h^{old}) \\ Q_B(B^{new}|B^{old}) &\geq Q_B(B^{old}|B^{old}) \end{aligned} \quad (5.50)$$

ensuring that the likelihood is increased with each iteration [54]

$$L(o_k^{new}, h^{new}, B^{new}) \geq L(o_k^{old}, h^{old}, B^{old}) \quad (5.51)$$

resulting in a GEM sequence converging to a local minimum. The procedure to find the maxima of the Q functions is the same as in pulse-shape estimation. First, the object solution is found by specifying

$$Q_o = \sum_{j,k,x,y,m,n} \mu_{\tilde{d}_{jk}}^{old}(x, y, m, n; o_k^{old}, h^{old}) \ln [o_k(m, n)] - o_k(m, n) h(x - m, y - n). \quad (5.52)$$

In order to maximize Q_o , the derivative of Equation (5.52) with respect to a particular object plane point and range sample is set equal to zero, $\partial Q_o / \partial o_{k_o}(m_o, n_o) = 0$. Solving for the object results in

$$o_{k_o}^{new}(m_o, n_o) = \frac{o_{k_o}^{old}(m_o, n_o)}{J} \sum_{j=1}^J \sum_{x=1}^X \sum_{y=1}^Y \frac{d_{jk_o}(x, y) h^{old}(x - m_o, y - n_o)}{i_{k_o}^{old}(x, y) + B^{old}(x, y)} \quad (5.53)$$

with J as the number of cubes and utilizing

$$\sum_{x=1}^X \sum_{y=1}^Y h(x, y) = 1 \quad (5.54)$$

and where

$$i_k^{old}(x, y) = \sum_{m=1}^M \sum_{n=1}^N o_k^{old}(m, n) h^{old}(x - m, y - n). \quad (5.55)$$

Equation (5.53) is the iterative solution for the object per range sample. The PSF is the other unknown parameter that uses the first set of complete data, $\tilde{d}_{jk}(x, y)$. The Q function for the PSF is

$$Q_h = \sum_{j,k,x,y,m,n} \mu_{\tilde{d}_{jk}}^{old}(x, y, m, n; o_k^{old}, h^{old}) \ln [h(x - m, y - n)] - o_k(m, n) h(x - m, y - n). \quad (5.56)$$

Similar to [71], a change of variables is required to remove the dependence on the pulse shape and to allow for easier differentiation. Setting $m' = x - m$ and $n' = y - n$, Q_h then becomes

$$Q_h = \sum_{j,k,x,y,m',n'} \left\{ \mu_{\tilde{d}_{jk}}^{old}(x, y, x - m', y - n'; o_k^{old}, h^{old}) \ln [h(m', n')] \right\} - o_k(x - m', y - n') h(m', n'). \quad (5.57)$$

Setting $\partial Q_h / \partial h(m'_o, n'_o) = 0$ and solving for the PSF produces the solution

$$h^{new}(m'_o, n'_o) = \frac{h^{old}(m'_o, n'_o)}{J \left[\sum_{k,x,y} o_k^{new}(x - m'_o, y - n'_o) \right]} \sum_{j,k,x,y} \frac{d_{jk}(x, y) o_k^{old}(x - m'_o, y - n'_o)}{i_k^{old}(x, y) + B^{old}(x, y)} \quad (5.58)$$

The object term in the denominator is the new estimate from Equation (5.53). Since, there are phase aberrations across the aperture and the PSF needs to be constrained, phase retrieval is performed on Equation (5.58) by the Gerchberg-Saxton algorithm [23]. In the

pulse-shape estimation, it was the object (i.e. pulse-shape) that was constrained making the phase retrieval unnecessary. Constraints on the estimates are required to avoid the trivial solution where the object is the data itself and the PSF is a delta function. Finally, the pixel bias must be estimated. In order to estimate the pixel bias, the second set of complete data, $\tilde{q}_k(x, y)$, is utilized. The Q function for the pixel bias is

$$Q_B = \sum_{k=1}^K \sum_{x=1}^X \sum_{y=1}^Y \frac{d_{jk}(x, y) B^{old}(x, y)}{i_k^{old}(x, y) + B^{old}(x, y)} \ln(B(x, y)) - B(x, y). \quad (5.59)$$

Setting $\partial Q_B / \partial B(x_o, y_o) = 0$ and solving for the pixel bias results in

$$B^{new}(x_o, y_o) = \frac{B^{old}(x_o, y_o)}{JK} \sum_{j=1}^J \sum_{k=1}^K \left(\frac{d_{jk}(x_o, y_o)}{i_k^{old}(x_o, y_o) + B^{old}(x_o, y_o)} \right). \quad (5.60)$$

GEM iterations continue and cease when the mean-square error (MSE) violates the stopping criteria. Once the stopping criteria is reached, range estimates are determined by using the NCC method on the object estimate.

The object estimation steps are:

1. Initialize object, PSF, and pixel bias
2. Perform one GEM iteration using Equations (5.53), (5.58), and (5.60)
3. Determine MSE and compare to stopping criteria
4. Repeat Steps 2 and 3 until stopping criteria reached
5. Use NCC to find new range estimates with Equation (4.17)

The initial estimates in step one are the same as GEM_p with the exception that the object is initialized by a matrix of ones.

5.2 Simulation

In order to verify the theory, a simulation scenario was developed whereby targets are interrogated by a 3D FLASH LADAR defined by the parameters from Table 5.1. The goal

Table 5.1: 3D FLASH LADAR parameters

Parameter	Value
Detector Array	128 × 128
Aperture Diameter (D)	2 mm
Mean Wavelength	1.55 μm
Focal Length	0.30 m
Target Range	5.21 m
Transmit Energy	10 mJ
Pulse Standard Deviation (σ_w)	3 ns
Beam Divergence	0.009 radians
Detector Spacing	100 μm
Detector Array Fill Factor	100%
Detector Bandwidth	0.5 μm
Target Reflectivity	10%
Solar Irradiance	10 Watts/m ² / μm
D/r_o Seeing Condition	1.43
Frame Rate	30 Hz
Time Samples	20
Sample Period	1.876 ns

is to improve range estimation given the noisy, blurry data observations. Results show range estimation improvement by performing object recovery either via a Wiener filter method or GEM algorithms as outlined in Sections 5.1.2 and 5.1.3. Previous research has taken the approach to use a Wiener filter on each individual range slice and then use a pixel-based ranging method on the resulting “deblurred” data cube [55]. The PSF for the Wiener filter is set as the diffraction-limited PSF of the system. Performance will illustrate that the GEM algorithms provide increased error performance over the Wiener filter while, at the same time, being more robust. Again, the GEM algorithms are more robust in that they do not need to know the point spread function, unlike the Wiener filter technique.

Using a Gaussian transmitted pulse, a 3D FLASH LADAR imaging scenario is developed in simulation using various geometrical shapes as targets shown in Figure 5.2(a)-(f). One important clarification on the receiver optics is that the detector array has an effective fill factor of 100% by placing a micro-lens array in front of the pixels to focus the light onto the pixel. Also, the data includes effects from an average atmospheric turbulence to enable blind deconvolution. Range estimates are also determined without processing to enable

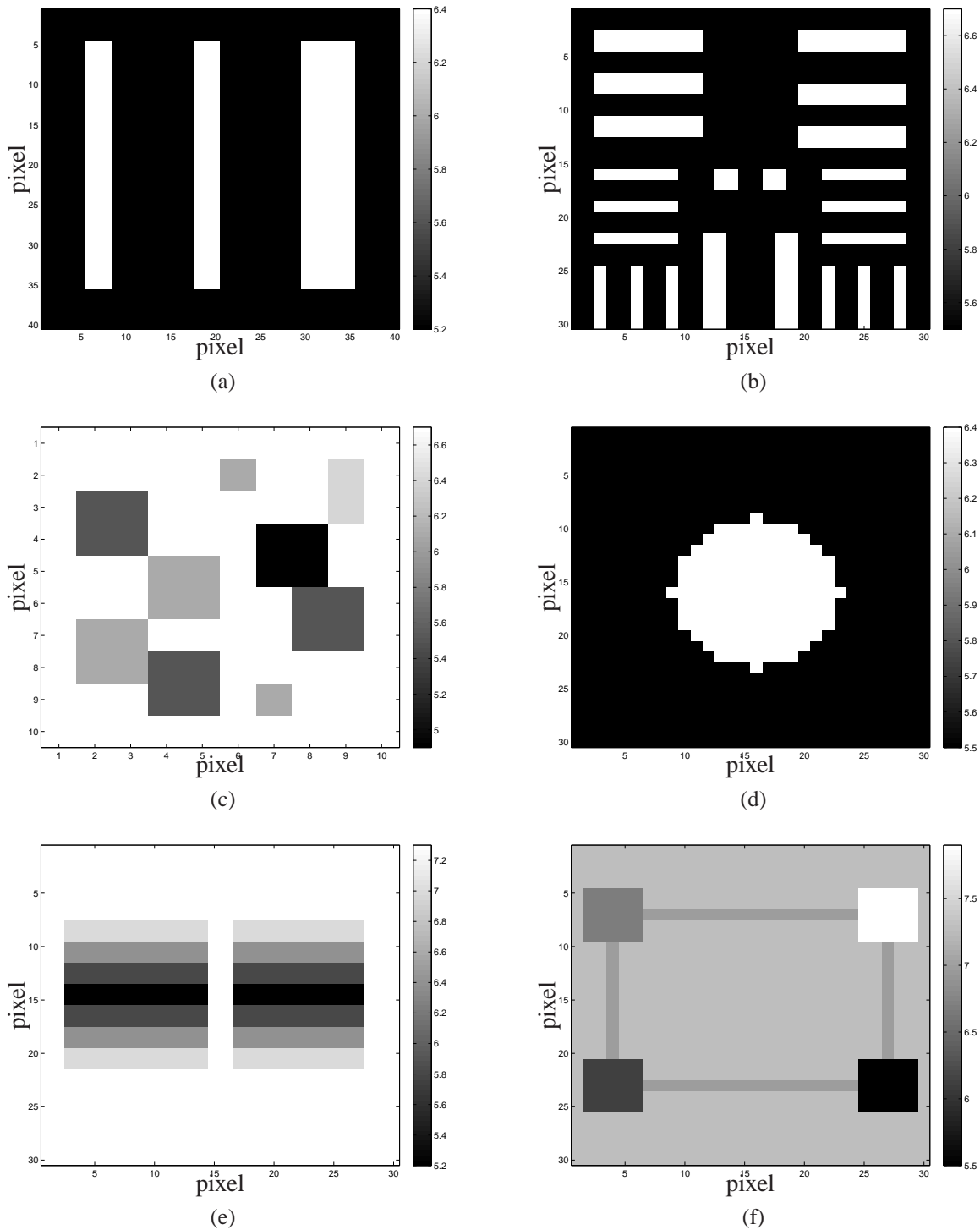


Figure 5.2: True ranges for simulation targets: (a) three bars, (b) Many bars, (c) Various blocks, (d) Cylinder, (e) Slanted boards, and (f) Connected blocks. The target names in this caption correspond to the targets in Table 5.2. The three bar target is also the experimental data target. Other targets illustrate the robustness of the estimation algorithms.

further comparison between no processing and object recovery attempts. Results for all the targets and methods with error metrics are summarized in Table 5.2. The numbers in bold indicate the best performer for the data set.

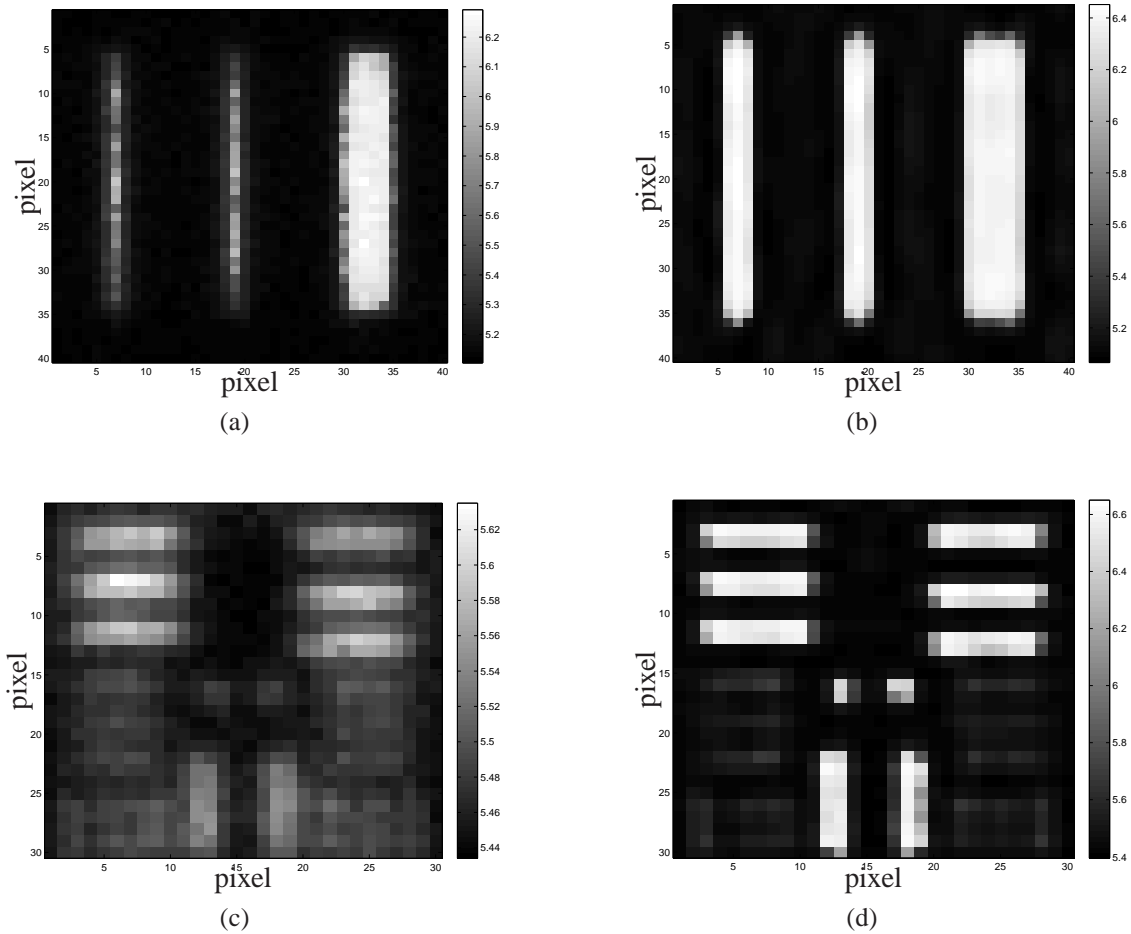


Figure 5.3: Estimated ranges for simulation targets: (a) No processing - three bars, (b) GEM_o processing - three bars, (c) No processing - Many bars, and (d) GEM_o processing - Many bars. Utilizing the GEM_o algorithm, simulation results show the image quality improvement and improved range estimation (RMSE improves 75% for 3 bar target).

Table 5.2 clarifications: “RMSE” is root mean square error (RMSE) in meters between the true ranges and estimated ranges of a target and is calculated by

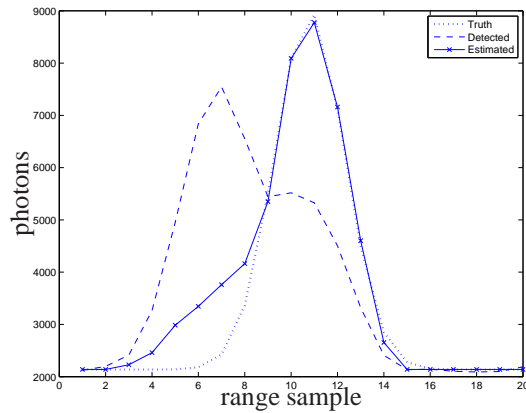
$$\text{RMSE} = \sqrt{\frac{\sum_{m=1}^M \sum_{n=1}^N \left(R(m, n) - \hat{R}(m, n) \right)^2}{MN}} \quad (5.61)$$

where $R(m, n)$ are the true ranges and $\hat{R}(m, n)$ (Equation (4.17)) are the estimated ranges. “Corr” is an image quality metric referring to the correlation coefficient between the true range image and estimated range image signifying linear relationship strength (not to be confused with the NCC method) and mathematically give by

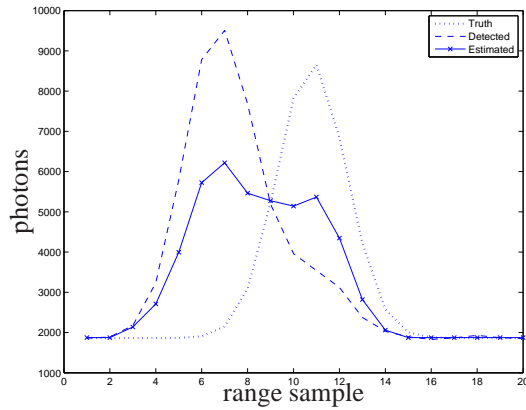
$$\text{Corr} = \frac{\sum_{m=1}^M \sum_{n=1}^N \left\{ (R(m, n) - \mu_R) (\hat{R}(m, n) - \mu_{\hat{R}}) \right\}}{\sigma_R \sigma_{\hat{R}}} \quad (5.62)$$

where μ_R and σ_R are the mean and standard deviation of the true range image respectively and $\mu_{\hat{R}}$ and $\sigma_{\hat{R}}$ are the mean and standard deviation of the estimate range image respectively. “OD” refers to the original data (OD) with no deblurring and ranges estimated by the NCC method, “WF” relates to range estimation using a Wiener Filter technique with NCC [55], “GEM_p” is the pulse-shape estimation GEM algorithm, and “GEM_o” is the object estimation GEM algorithm.

The targets of primary interest are the three bar target and the multiple bar target because the three bar target is also the experimental target and the multiple bar target is most sensitive to spatial blurring of all the targets. The bar targets are constructed in simulation consisting of two flat, perpendicular optically rough surfaces at different ranges. Referring to Figures 5.2(a) and (b), the first surface in range has rectangular cut-out shapes while the second surface contains no cutouts. This type of target was chosen to highlight not only the coupling/blurring effects of the pixels along the edges of the rectangles, but also the decoupling and ranging capability of the GEM algorithm. The other targets are built in similar manner. Bar target shapes were used because the distances and shape dimensions can be physically measured in a laboratory environment to show range estimation improvement.



(a)



(b)

Figure 5.4: (a) Using the data from Figure 5.3(c)-(d), investigating pixel (8,23) shows the estimated waveform (object plus pixel bias) closely matching the true waveform while the detected waveform does not. The estimated range is 6.6 m while the true range is 6.7 m. The algorithm also implicitly estimates the pixel bias term accurately. (b) Again, using the data from Figure 5.3(c)-(d), investigating pixel (17,14) shows the estimated waveform improving upon the detected waveform, but not able to match the true waveform as well as the previous pixel. The estimated range is 5.7 m while the true range is 6.7 m. Incorrect range estimation after the GEM_o algorithm relates to blurring severity (edges of cut-outs in first surface) and/or a particularly noisy realization from the Poisson distribution.

Table 5.2: Range estimation results for simulation data

Data set	Metric	OD	WF	GEM _p	GEM _o
Three bars	RMSE (m)	0.402	0.346	0.163	0.100
	Corr	0.767	0.830	0.963	0.984
Many bars	RMSE (m)	0.596	0.561	0.346	0.365
	Corr	0.687	0.664	0.786	0.794
Slanted boards	RMSE (m)	0.225	0.171	0.161	0.131
	Corr	0.945	0.971	0.967	0.983
Cylinder	RMSE (m)	0.184	0.153	0.160	0.153
	Corr	0.877	0.925	0.945	0.962
Various blocks	RMSE (m)	0.473	0.209	0.344	0.175
	Corr	0.595	0.931	0.725	0.955
Connected blocks	RMSE (m)	0.208	0.133	0.158	0.112
	Corr	0.853	0.955	0.918	0.970

Table 5.2 and the range images from Figures 5.2 and 5.3 show the negative effects of the blurring on range estimation juxtaposed with the positive effects from attempting to recover the original object through Wiener filtering or the GEM algorithms. Figure 5.4(a) shows pixel waveforms successfully recovered while Figure 5.4(b) exhibits a situation where the recovery was not as successful. Implicit in the results is the ability to accurately estimate the pixel bias. Without it, the object model falls apart and range error becomes extremely large.

An additional concern is assessing the computational times for the object retrieval methods (WF, GEM_p, and GEM_o). Although, it should be noted again that the WF method requires the PSF to be known a priori. The computational times were analyzed using operations counting. For example, this counting means that an addition, divide, or multiplication count as one operation each. Also, the Fast Fourier Transform (FFT) is utilized to accomplish convolution and correlation and counts as $N \log_2(N)$ operations where N is the number of points [13]. The number of operations required in the WF method (Section 5.1.1) are 6×10^5 . Implementing steps 2-7 from Section 5.1.2 until the stopping criteria is reached, the GEM_p algorithm uses 1.8×10^7 operations per iteration. Finally, the GEM_o algorithm has a computation burden of 1.9×10^6 operations per iteration while performing Step 2-4 (until stopping criteria violation) from Section 5.1.3. The numbers computed for all the

methods correspond to a pixel area of 40×40 with 18 range samples. One cube was used for the WF and GEM_p methods while two cubes was used for GEM_o . The additional burden on GEM_p is from the inner iterations which include 100 GEM iterations followed by an update on the pulse-shape and a repeat of the process. While the increase in computation time is substantial compared to the WF method, the GEM_p and GEM_o algorithms represent a significant increase in capability with respect to range accuracy and to required a priori information.

Through simulation, the model and object recovery attempts have been verified. The final step is to use experimental data to validate simulation results.

5.3 *Experimental Results*

Using the pre-processed experimental data described in Chapter III, Table 5.3 and Figure 5.5 illustrate the range estimation benefits of object retrieval. The bold numbers in the table indicate the best performing method for the data set. The pulse-shape and object estimation give an RMSE improvement of 25% and 34% respectively over the original data. Additionally, the pulse-shape and object estimation give an RMSE improvement of 7% and 18% respectively over the Wiener filter algorithm. Figure 5.5(c) shows the image quality improvement over the original data range image in Figure 5.5(b). Pixel waveforms provide additional information on the object recovery abilities. Figure 5.5(d) demonstrates this ability on a second surface pixel, (32,18), where the raw waveform results in an incorrect range determination. In contrast, the object recovery algorithm (GEM_o) yields an improved range estimate by sufficiently estimating the true waveform. Additionally, attempts were also made to use asymmetrical pulses in the NCC method. However, range estimation error did not significantly change. This result is partly due to the gain correction where the waveform becomes more symmetrical after correction. Since the exact pulse emitted by the laser is unknown, the pulse-shape estimation used the best approximation based on the observed data.

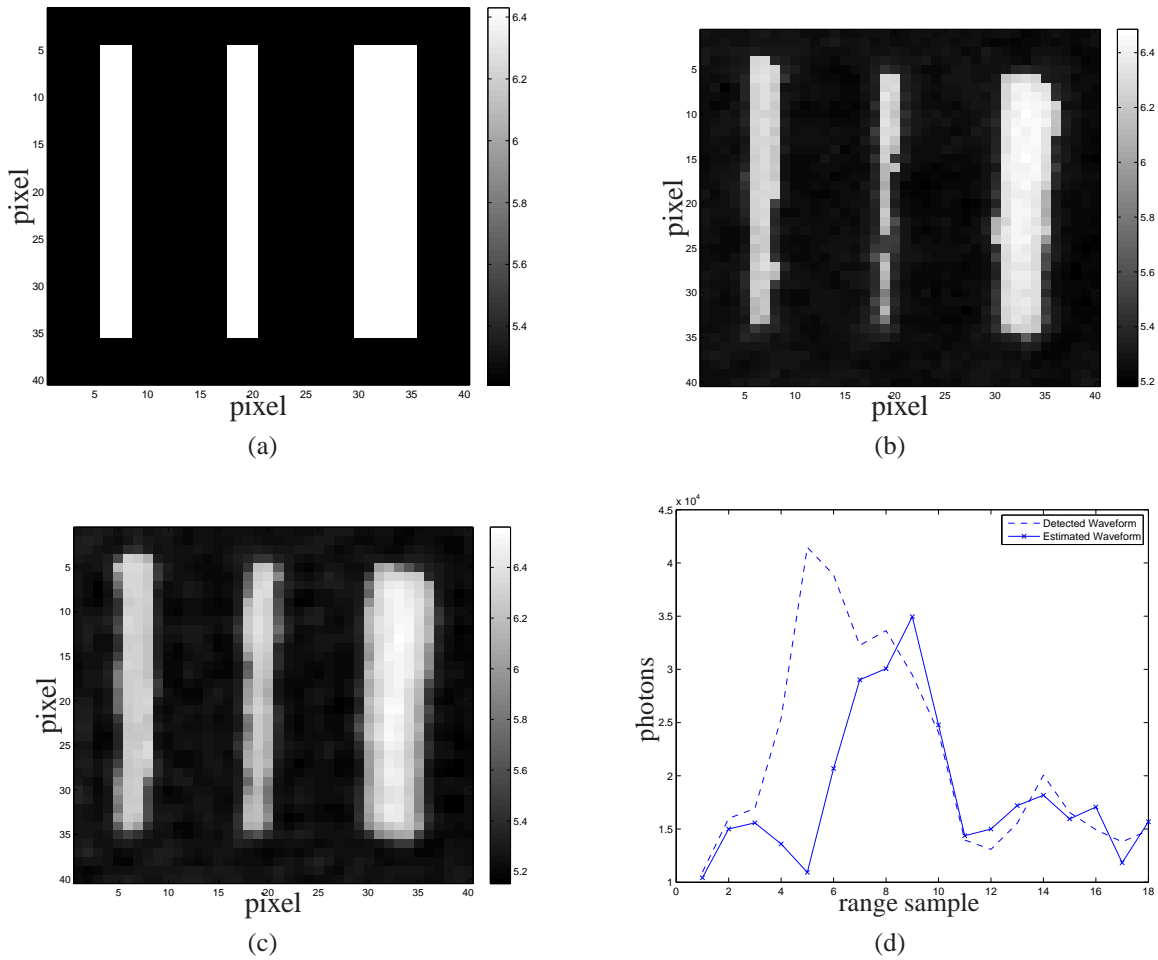


Figure 5.5: Experimental target : (a) True ranges with first surface at 5.21 m and second surface at 6.43 m with 1.22 m of separation in between surfaces, (b) Ranges using NCC without using object recovery (c) Estimated ranges using GEM_o algorithm followed by NCC (d) Considering pixel (32,18), its estimated waveform (object plus pixel bias) shows similar results from the simulated data. The estimated waveform more closely resembles the true waveform with the range close to range sample 9. Also, the algorithm correctly estimates the pixel bias confirming that the bias must arise from a noise source following the Poisson distribution (i.e. dark current).

Table 5.3: Range estimation results for experimental data

Data set	Metric	OD	WF	GEM_p	GEM_o
3 bars	RMSE (m)	0.301	0.243	0.226	0.198
	Corr	0.818	0.883	0.900	0.924

5.4 Conclusions

Utilizing waveform sampling capability, the positive effects of object recovery in 3D FLASH LADAR range estimation is clearly evident. The innovative 3D FLASH LADAR sensor provides both an imaging and ranging ability enabling established theory to be applied to a novel manner. Given simulation and experimental results, it is clear the chosen model and noise sources are an appropriate choice for 3D FLASH LADAR data operating under certain conditions (“sular mode” meeting spatial sampling requirements). The raw data coming off the sensor does not fit the model, but straight-forward pre-processing steps convert the data to an acceptable form for the algorithms.

In mild spatial blurring conditions, simulation results predict that the GEM algorithms increase range estimation performance substantially over no-processing and the Wiener filter method. Again, the Wiener filter even has an unfair advantage because it is provided with the exact (or estimated) PSF function used in generating the data while the GEM algorithms have to estimate the PSF. Considering the experimental data, its performance is nearly diffraction-limited as evidenced by the experimental PSF and OTF. However, the GEM algorithms still increase range estimation performance over the Wiener filter. Supported by simulation results, it is appropriate to say that the GEM algorithm would show even better range estimation performance versus the Wiener filter in severe isoplanatic atmospheric blurring conditions or with sub-optimal optics.

A trade-off exists for Wiener filter and object recovery algorithms between computation cost and range accuracy. The Wiener filter is the least computationally taxing object recovery algorithm, but is the least accurate and requires a priori knowledge of the PSF. The GEM algorithms are computationally expensive, but provide the best range performance and can perform blind deconvolution. Considering the GEM algorithms, the pulse-shape estimator is extremely valuable in that it can perform range estimation on a single cube thereby removing potential for any registration or timing errors. If multiple cubes are available and properly registered, object estimation is undoubtedly the best algorithm to use. Although, experimentally, none of the algorithms were able to match the success found

in simulation. Any residual error in the experimental results can be attributed to system noise, the detected light containing residual laser speckle, residual gain error, and detector blurring.

There are prospective avenues for continued investigation and improvement. The pulse-shape estimation is very dependent on the selected waveform model. Improvements in the range estimation would be realized if a true waveform model for the transmitted laser pulse was derived or calculated experimentally. Errors in the experimental data result from assuming a generalized shape that is corrupted by distorting effects (spatial blur, pixel blur, and noise). In addition, the variable of interest (range term) would ideally be directly estimated. The maximum likelihood solution for the range term could be achieved if another model was discovered. The algorithm in this paper extracts the range from the maximum likelihood solution for the pulse-shape. Also, even after the pre-processing steps, the experimental data exhibits noisy behavior. A more thorough characterization of the 3D FLASH LADAR noise sources would augment or verify the chosen noise sources. Finally, isoplanatic imaging is valid for the experimental set-up in the laboratory. However, object recovery from 3D FLASH LADAR observations subject to heavy anisoplanatic turbulence would provide an ability to improve range estimation in a variety of field or operational situations.

VI. Range Separation Performance and Optimal Pulse-Width

Prediction of a 3D FLASH LADAR using the Cramer-Rao Bound

The purpose of this chapter is to use established estimator variance theory applied to a three dimensional FLASH LAsER Detection And Ranging (3D FLASH LADAR) sensor in order to bound estimator performance and enable prediction of optimal resolution performance. The theory in this chapter supports “hit mode” and “sular mode” of 3D FLASH LADAR operation. Additionally, pixel spatial and temporal integration is a common concern for photo-detectors. For this paper, the pixel spatial response is assumed to be ideal while the temporal integration is assumed to be less than half of the range interval. Supplemental simulations were completed that investigated integration effects. The results show that these effects have a negligible effect on the blurring severity and received pulses. The entire chapter contains novel and original efforts: CRB derivation on range and spatial separation as well as target amplitudes, optimal pulse-width determination given simple and complex targets, and optimal pulse-width determination given a normalized pulse definition.

The Cramer-Rao Bound (CRB) is an important theoretical result in estimation theory that can be applied to numerous fields in science and engineering [84]. Pertaining to a two point target scene illuminated by a 3D FLASH LADAR (Section 4.4.1), the CRB is utilized to bound the range separation estimation variance. The simple scene is adopted to allow for closed-form results and to allow conclusions to be drawn about the effects of range separation on the bound. Once the range separation CRB is derived, an unbiased range separation estimator is developed to enable comparisons to the CRB. The expected results are shown in an example comparing the estimator variance and the bound across possible range separations.

Additionally, the CRB is used to predict system performance which could aid in the LADAR development process. Per conventional RADAR theory, range resolution improves (i.e. becomes smaller) as the effective pulse-width is shortened [76]. Although, the RADAR engineer must be concerned about other factors as well to include the high peak power requirements of a narrow pulse. In the case of 3D FLASH LADAR, there is the abil-

ity to produce ultra-short laser pulses in the femtoseconds (10^{-15}) compared to the laser pulse in the nanoseconds (10^{-9}) used in this research [66], [88]. Along with benefits to target ranging and identification, one would expect that the increase in the range resolution would be improved by several orders of magnitude with an ultra-short laser pulse. However, similar to the RADAR engineer concerns about high peak power for short pulses, the LADAR engineer has to be concerned that the receiver electronics can sufficiently sample the returned pulse. With the laser pulse-width lasting in the tens of nanoseconds, the current receiver technology can only generate a finite amount of samples due to the complicated design that is required to sample the pulse every couple of nanoseconds [19]. Recognizing the design issues, CRB theory is employed to analyze the trade-off between laser pulse-width and range sampling interval. CRB theory and subsequent simulation determine that there is an optimal pulse-width that produces an optimal range resolution for a particular range sampling capability.

The chapter is organized as follows: Section 6.1 derives the range separation CRB for a two point target scene, Section 6.2 discusses the results of the unbiased range separation estimator and compares it to the CRB, and Section 6.3 uses CRB and simulation to find an optimal pulse-width for several different range sampling scenarios for the two target case. This section also finds an optimal pulse-width considering more complex targets. Additionally, an optimal pulse-width for the two-target scene is found using a normalized pulse that is independent of range sampling. Finally, Section 6.4 draws conclusions based on the observed results.

6.1 CRB on Range Separation Estimation

In this section, the CRB for range separation Δ_k is derived using the two-point target data model from Section 4.4.1. Other bounds are determined as well including spatial separation and the target amplitudes. For a particular imaging scenario, the range separation CRB is shown in a figure across the possible range separations.

For multiple unknowns, the CRB is defined by the diagonals of the Fisher Information Matrix (FIM) inverse and provide a lower bound on the variance of any unbiased estimator

which is shown for a general, multiple unknown parameter case by [84]

$$\text{var} \left[\hat{\theta}_i (\mathbf{D}) - \theta_i \right] \geq [J^{-1}]_{ii} \quad (6.1)$$

where “var” is the variance, $\hat{\theta}_i (\mathbf{D})$ is the estimate of a particular unknown, non-random variable θ_i , \mathbf{D} is the observation space, and J is the FIM. The elements of the FIM are the negative expected value of the double derivative log-likelihood function and provides a measure of the amount of information of an unknown parameter contained in the random process. Mathematically, the FIM is defined by [84]

$$J_{ij} = -\text{E} \left[\frac{\partial^2 \ln P (d_k (x, y) = D_k (x, y) \forall k, x, y)}{\partial \theta_i \partial \theta_j} \right] \quad (6.2)$$

where E is the expected value operation, “ln” is the natural log, and P is the probability mass function (PMF) for all 3D FLASH LADAR observations with $d_k (x, y)$ as the realizations of the observations. Assuming statistical independence of each volume element (voxel), the PMF for the data model is defined by

$$P [d_k (x, y) = D_k (x, y) \forall k, x, y] = \prod_{k=1}^K \prod_{x=1}^X \prod_{y=1}^Y \frac{i_k (x, y)^{d_k (x, y)} \exp \{-i_k (x, y)\}}{d_k (x, y)!} \quad (6.3)$$

where the assumed dominant noise source is photon (shot) noise described by the Poisson distribution. While lasers exhibit partial coherence meaning the negative binomial distribution should be used for the light statistics, this photon noise assumption is valid when the operating environment produces a large enough speckle parameter so that the negative binomial distribution approaches the Poisson distribution [24]. Previous 3D FLASH LADAR work has shown the speckle parameter to be adequate to assume the Poisson distribution [9]. Additionally, the Poisson distribution CRB provides a lower bound to the negative binomial CRB considering the higher negative binomial variance [60]. This fact creates a true lower bound (most pessimistic) with the Poisson distribution CRB regardless of the imaging conditions.

After performing the required operations, the general solution for the FIM elements is determined to be [9], [39]

$$J_{ij} = \sum_{k=1}^K \sum_{x=1}^X \sum_{y=1}^Y \frac{1}{i_k(x, y)} \frac{\partial i_k(x, y)}{\partial \theta_i} \frac{\partial i_k(x, y)}{\partial \theta_j}. \quad (6.4)$$

Particular to this work, there are four non-random unknown variables in the data model, $\theta = [\Delta_m, \Delta_k, A_t, A_r]$, resulting in a 4x4 FIM with its elements determined to be

$$\begin{aligned} J_{11} &= \sum_{k=1}^K \sum_{x=1}^X \sum_{y=1}^Y \frac{1}{i_k(x, y)} \left[A_t p(r_k - (K_r - \Delta_k)) \frac{\partial}{\partial \Delta_m} h(x - \Delta_m, y) \right]^2 \\ J_{22} &= \sum_{k=1}^K \sum_{x=1}^X \sum_{y=1}^Y \frac{1}{i_k(x, y)} \left[A_t h(x - \Delta_m, y) \frac{\partial}{\partial \Delta_k} p(r_k - (K_r - \Delta_k)) \right]^2 \\ J_{33} &= \sum_{k=1}^K \sum_{x=1}^X \sum_{y=1}^Y \frac{1}{i_k(x, y)} [p(r_k - (K_r - \Delta_k)) h(x - \Delta_m, y)]^2 \\ J_{44} &= \sum_{k=1}^K \sum_{x=1}^X \sum_{y=1}^Y \frac{1}{i_k(x, y)} [p(r_k - K_r) h(x, y)]^2 \\ J_{12} &= \sum_{k=1}^K \sum_{x=1}^X \sum_{y=1}^Y \frac{1}{i_k(x, y)} (A_t)^2 p(r_k - (K_r - \Delta_k)) h(x - \Delta_m, y) \frac{\partial}{\partial \Delta_k} p(r_k - (K_r - \Delta_k)) \dots \\ &\quad \times \frac{\partial}{\partial \Delta_m} h(x - \Delta_m, y) \\ J_{13} &= \sum_{k=1}^K \sum_{x=1}^X \sum_{y=1}^Y \frac{1}{i_k(x, y)} A_t [p(r_k - (K_r - \Delta_k))]^2 h(x - \Delta_m, y) \frac{\partial}{\partial \Delta_m} h(x - \Delta_m, y) \\ J_{14} &= \sum_{k=1}^K \sum_{x=1}^X \sum_{y=1}^Y \frac{1}{i_k(x, y)} A_t p(r_k - K_r) p(r_k - (K_r - \Delta_k)) h(x, y) \frac{\partial}{\partial \Delta_m} h(x - \Delta_m, y) \\ J_{23} &= \sum_{k=1}^K \sum_{x=1}^X \sum_{y=1}^Y \frac{1}{i_k(x, y)} A_t p(r_k - (K_r - \Delta_k)) [h(x - \Delta_m, y)]^2 \frac{\partial}{\partial \Delta_k} p(r_k - (K_r - \Delta_k)) \\ J_{24} &= \sum_{k=1}^K \sum_{x=1}^X \sum_{y=1}^Y \frac{1}{i_k(x, y)} A_t p(r_k - K_r) h(x, y) h(x - \Delta_m, y) \frac{\partial}{\partial \Delta_k} p(r_k - (K_r - \Delta_k)) \\ J_{34} &= \sum_{k=1}^K \sum_{x=1}^X \sum_{y=1}^Y \frac{1}{i_k(x, y)} p(r_k - K_r) p(r_k - (K_r - \Delta_k)) h(x, y) h(x - \Delta_m, y) \end{aligned} \quad (6.5)$$

where

$$\begin{aligned}
\frac{\partial i_k(x, y)}{\partial \Delta_m} &= A_t p(r_k - (K_r - \Delta_k)) \frac{\partial}{\partial \Delta_m} h(x - \Delta_m, y) \\
\frac{\partial i_k(x, y)}{\partial \Delta_k} &= A_t h(x - \Delta_m, y) \frac{\partial}{\partial \Delta_k} p(r_k - (K_r - \Delta_k)) \\
\frac{\partial i_k(x, y)}{\partial A_t} &= p(r_k - (K_r - \Delta_k)) h(x - \Delta_m, y) \\
\frac{\partial i_k(x, y)}{\partial A_r} &= p(r_k - K_r) h(x, y) \\
\frac{\partial}{\partial \Delta_m} h(x - \Delta_m, y) &= \frac{(x - \Delta_m)}{2\pi\sigma_h^4} \exp\left\{-\frac{((x - \Delta_m)^2 + y^2)}{2\sigma_h^2}\right\} \\
\frac{\partial}{\partial \Delta_k} p(r_k - (K_r - \Delta_k)) &= \frac{-(r_k - (K_r - \Delta_k))}{\sqrt{2\pi}\sigma_{pd}^3} \exp\left\{-\frac{(r_k - (K_r - \Delta_k))^2}{2\sigma_{pd}^2}\right\}. \quad (6.6)
\end{aligned}$$

NOTE: The “ \times ” in J_{12} is a multiply operation. The FIM is inverted and the CRB for each of the unknowns is on the diagonal of the inverted FIM matrix with the range separation CRB at $[J^{-1}]_{22}$. The purpose behind supplying the FIM element expressions was to provide enough information to enable the work to be reproduced. Although an example plot is given later in the section, the range separation CRB expression itself is not shown due to its length and complexity.

Besides the four non-random unknown parameters, the CRB also depends on non-random known parameters to include σ_{pt} , σ_h , and t_s . In order to view a useful plot, all other unknown and known factors are held constant while the Δ_k is stepped from the beginning to the end of the range extents. Following this procedure, Figure 6.1 shows the range separation bound for a specific scenario with $\Delta_m = 1$ pixel, $\sigma_h = 3$ pixels, $\sigma_{pt} = 3$ ns, $A_t = 0.5 \times 10^4$ photons, $A_r = 2 \times 10^5$ photons, $B(x, y) \sim N(750, 38)$ in units of photons, and range sampling $t_s = 1.876$ ns. These values were chosen to represent a scenario where the 3D FLASH LADAR interrogates adjacent targets with different reflectivities while experiencing significant turbulence in the atmosphere. Furthermore, the bias definition is consistent with estimation results from experimental data.

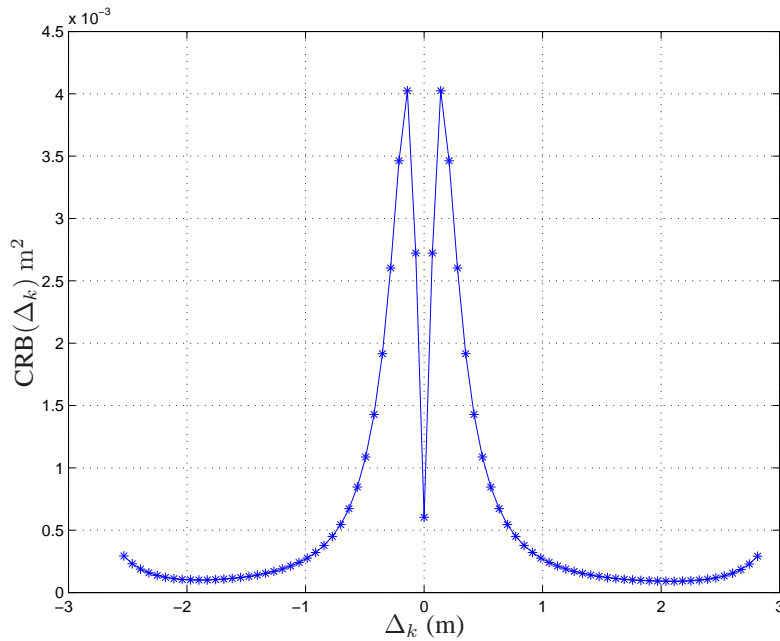


Figure 6.1: This plot shows an example CRB with $\Delta_m = 1$ pixel, $\sigma_h = 3$ pixels, $\sigma_{pt} = 3$ ns, $A_t = 0.5 \times 10^4$ photons, and $A_r = 2 \times 10^5$ photons. The bound behaves appropriately considering the variance goes up as the separation becomes smaller corresponding to the notion that close-in targets are tougher to resolve. The peak of the bound occurs when the range and spatial coupling are at their maximum. Further, when the range separation near zero, the range coupling is diminished, but the bound doesn't go to exactly zero because the spatial coupling is still present.

The shape of the curve in Figure 6.1 reflects the negative effects of the range and spatial blurring as the targets become closer. Although, the effects of range blurring are minimized when the targets are at nearly identical ranges and the bound primarily depends on the spatial blurring. Additionally, the increase in the bound past ± 2 meters of range separation is due to the truncation of the pulse at those ranges. An assumption in the bound derivation is a fully contained pulse within the range extents. The impact is negligible considering the eventual application of the CRB towards range resolution. Targets with ± 2 meters of range separation would be easily resolved. Changes in these values affect the bound in a predictive manner. For example, increasing σ_h and σ_{pt} doesn't affect the general shape of the range separation CRB, but it does increase the bound's magnitude due to increased spatial and range blurring hampering range separation estimation.

More specifically, Figure 6.2 shows several examples of how the range separation CRB is affected by changing parameters in the model including target amplitude, blurring severity, and spatial separation. Each individual figure holds all other parameters constant and plots the CRB while changing one parameter. For example, Figure 6.2(a) changes the unknown target amplitude A_t while keeping all other parameters constant. Unless otherwise noted, the standard values for the parameters are : $\sigma_{pt} = 3$ ns, $\delta_m = 1$ pixel, $\sigma_h = 3$ pixels, $t_s = 1.876$ ns, $A_t = 0.5 \times 10^4$ photons, and $A_r = 2 \times 10^5$ photons. The next few paragraphs detail how the changing parameters effect the range separation CRB. The parameter changes affect only the bound values, but not the general shape of the bound.

Figure 6.2(a) - A_t effects. As the unknown target's amplitude is increased, the bound decreases meaning that higher SNR values of the unknown target aids in range separation estimation efforts. (Inversely proportional to bound)

Figure 6.2(b) - A_r effects. Changing the known target's amplitude has the opposite effect of A_t . As the A_r amplitude is increased, the bound also increases meaning that range separation estimation becomes more difficult due to the increased blurring between the targets. In other words, estimating the range separation becomes very difficult when

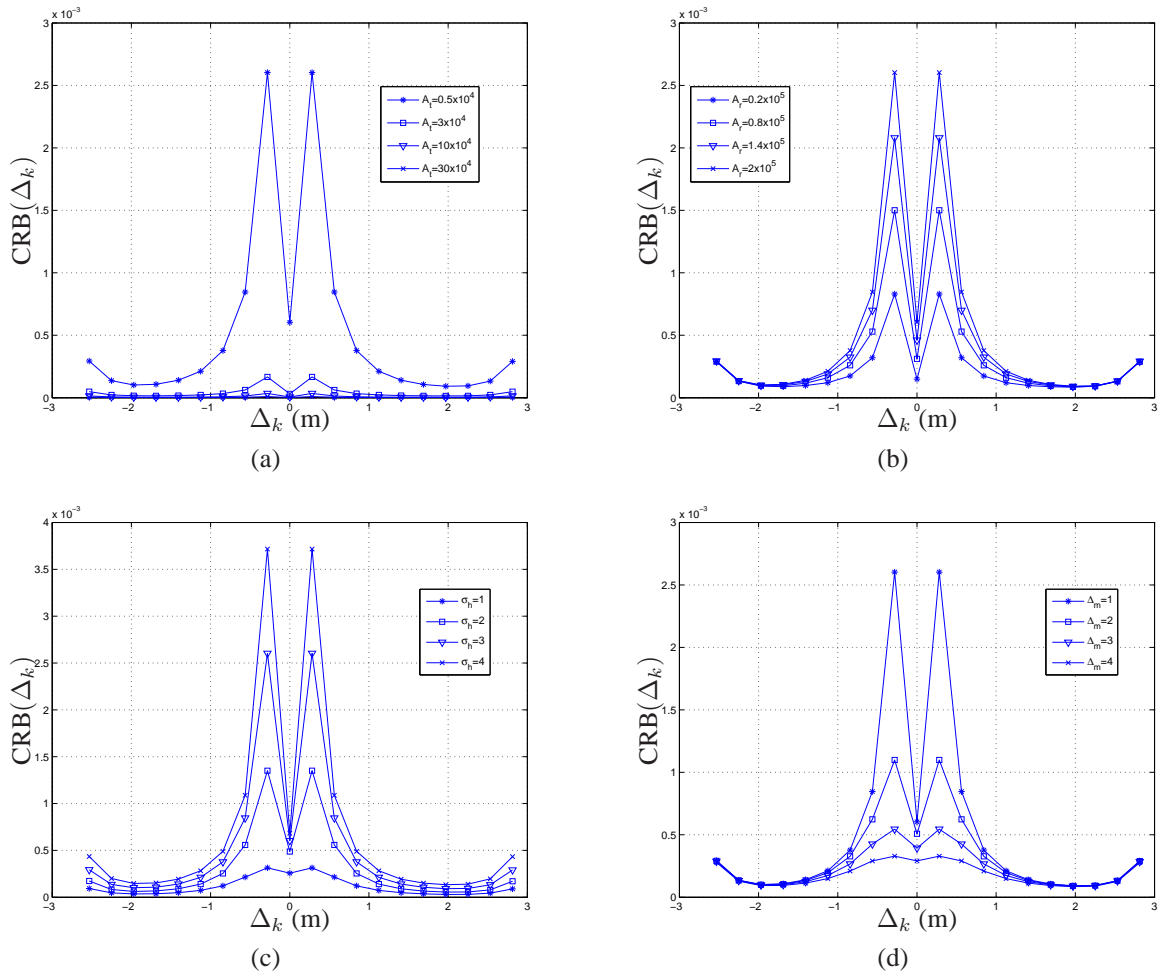


Figure 6.2: Effects on $\text{CRB}(\Delta_k)$ when changing several parameters in the model including target amplitude, blurring severity, and spatial separation.

- (a) A_t - inversely proportional to bound
- (b) A_r - proportional to bound
- (c) σ_h - proportional to bound
- (d) Δ_m - inversely proportional to bound

considering a very bright known target next to a much dimmer unknown target and vice versa. (Proportional to bound)

Figure 6.2(c) - σ_h effects. As the blurring severity increases, the bound also increases meaning that more blurring (i.e. more coupling between the targets) hinders range separation estimation performance. (Inversely proportional to bound)

Figure 6.2(d) - Δ_m effects. Finally, as the spatial separation increases, there is a logical corresponding range separation estimation performance improvement due to decrease in coupling between the targets. (Inversely proportional to bound)

6.2 Range Separation Estimation Results

Using the model governed by Equation (6.3) and the standard parameter values from the previous section, an unbiased range separation estimator from Section 4.4.2 is applied to enable comparisons of the range separation estimator variance to the CRB. Other pixel-based range estimators are available including peak detection, matched filtering, and normalized cross-correlation. However, in this two-target scenario, these estimators are all biased because they assume that there's only one target per pixel. While one may try to deblur the data, the operation will not be totally successful and some bias will still result. The estimator used in the subsequent sections is different in that it is defined as having two targets per pixel thus eliminating the bias.

Prior to comparison, the estimator must first be determined to be unbiased. An estimator of an unknown parameter is unbiased if the expected value of the estimator is the unknown parameter itself (i.e., on average, one expects the estimator to choose the true value of the parameter to be estimated) [84]. In terms of this simulation, the estimator is considered to be unbiased if the bias squared contribution to the mean square error (MSE) is small compared to the range variance contribution. This relationship results from the fact that MSE equals the range variance plus bias squared. Analytical methods to determine the bias are available, but graphical nature of the algorithm prohibits such undertakings requir-

ing the generation of statistics based on many instantiations of the observed data through simulation.

Therefore, a two point target simulation is constructed reflecting the observation model defined in Equation (6.3). Shown in Figure 6.3, the simulation results include MSE, bias and range separation variance. As expected, Figure 6.3(c) shows the bias decrease as the iterations increase with a small bias left after the last iteration. Referring to Figures 6.3(a), (b), and (c), the range variance dominates the MSE and the two point target estimator is determined to be unbiased.

With the estimator established as unbiased, the range separation variance is compared to the CRB to observe how each is affected given changes in the range separation. Figures 6.1 and 6.3(b) show the CRB and range separation variance respectively. Although, in order to gain more insight and show trends, Figure 6.4 compares the CRB and range variance in the same plot where the similar behavior is now evident. In fact, the estimator range variance is such that it approaches equality with the bound. This equality would make the estimator efficient [84]. The definition of an efficient estimator relates to the CRB. CRB theory states that any unbiased estimator must a variance equal to or greater than the bound. An efficient estimator is an unbiased estimator whose variance equals that of the bound. Although this estimator was shown to be unbiased, it is not theoretically guaranteed to be efficient. In addition, toward the edges of the range separation ± 1.5 m, the bound should theoretically go to zero like the variance does, but it doesn't because the Gaussian pulse never goes to zero. This non-zero bound can be ignored since estimation is easily performed at those range separations and can also be mitigated by using other pulse models such as a negative parabolic that equals zero until the pulse is received [63].

6.3 *Optimal Pulse-width Investigation*

Referring to Equation (4.22), σ_{pt} controls the pulse-width of the received signal. Pulse interactions with the target cannot be controlled, but the transmitted pulse-width can be factored into the design of the LADAR system. Figure 4.1(b) shows an example of a pulse with $\sigma_{pt} = 0.88$ ns. Following standard RADAR theory, a smaller effective pulse-

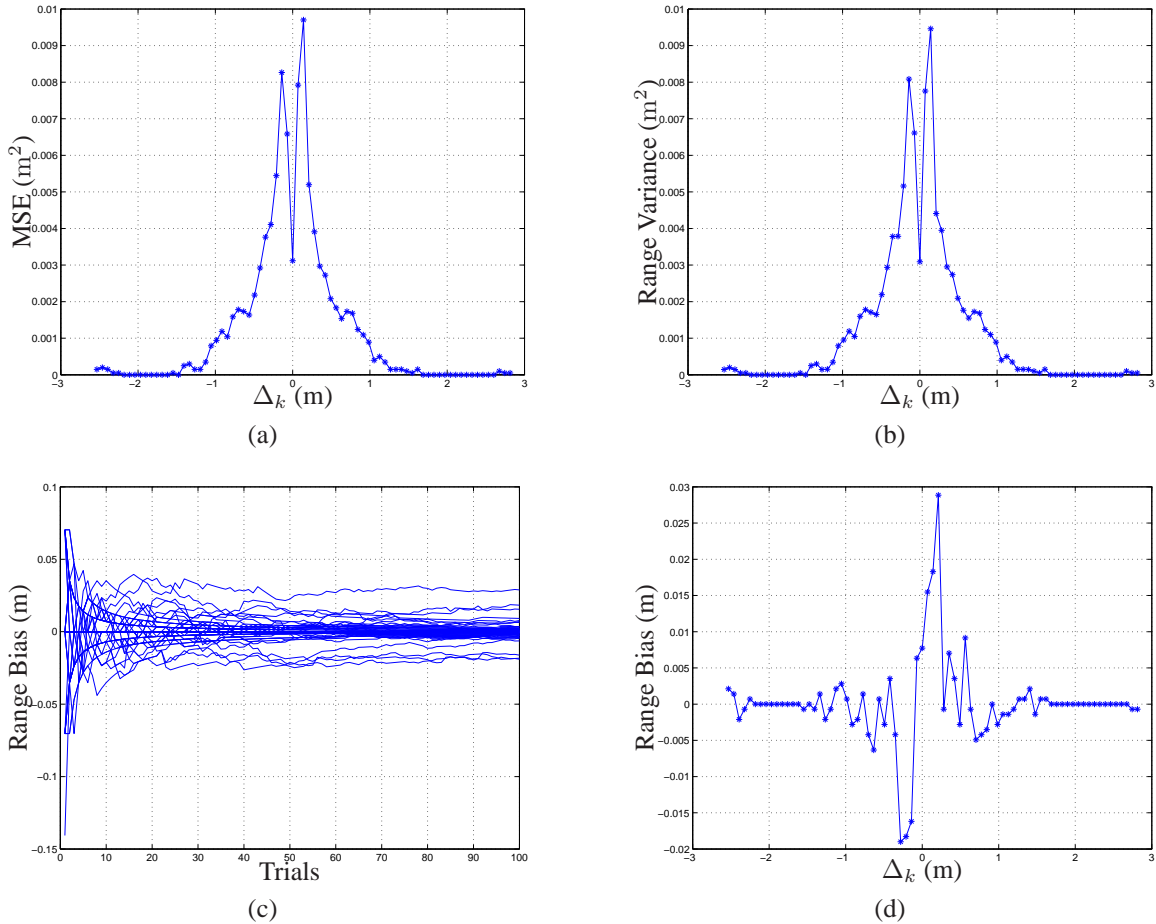


Figure 6.3: These plots show the range separation estimation results of a two point target data model simulation.

(a) Mean square error (MSE) between the truth data and the estimate.

(b) Range separation estimate variance.

(c) Each curve is a bias calculation for a different Δ_k over many trials. At each trial, the estimated range is an average of the previous estimated ranges (i.e. a running average).

(d) Bias results taken from the last trial from (c). Comparing (a), (b), and (c), it can be seen that estimator is unbiased due to the variance dominating the MSE.

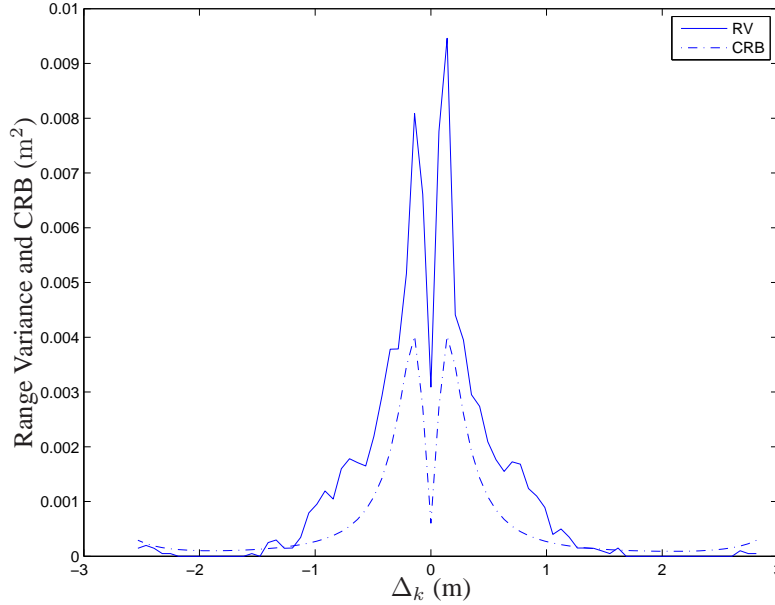


Figure 6.4: Taking the results from Figures 6.1 and 6.3(b), this plot compares the CRB and the simulated range variance showing agreement both in the Cramer-Rao inequality and in the curve shapes.

width is desirable due to its ability to resolve targets closer together. However, given the discrete nature of digital sampling employed by the electronic receivers (denoted by t_s from Equation (4.19)), a smaller pulse-width may actually degrade performance due to aliasing.

Therefore, the CRB is used to predict an optimal pulse-width using a range resolution metric. Subsequently, a simulation is accomplished to validate the CRB results. Due to their separate and distinct methods, agreement on the optimal pulse-widths between the CRB and simulation lends confidence to the results. The range-resolution metric is defined by comparing the square root of the CRB (or range separation variance in simulation) with the actual range separation, Δ_k . Referring to Figure 6.5, the location where the values equal is defined as the range-resolution of the system. In other words, if the actual range separation is within one standard deviation of the range separation estimate, then targets would not be resolvable due to the estimation uncertainty. This definition implies that, on average, the estimator would be able to resolve targets separated further while targets closer together than that value are not resolvable. After searching over many pulse-widths, the pulse-width that provides the best range resolution (i.e. lowest value) is selected as optimal.

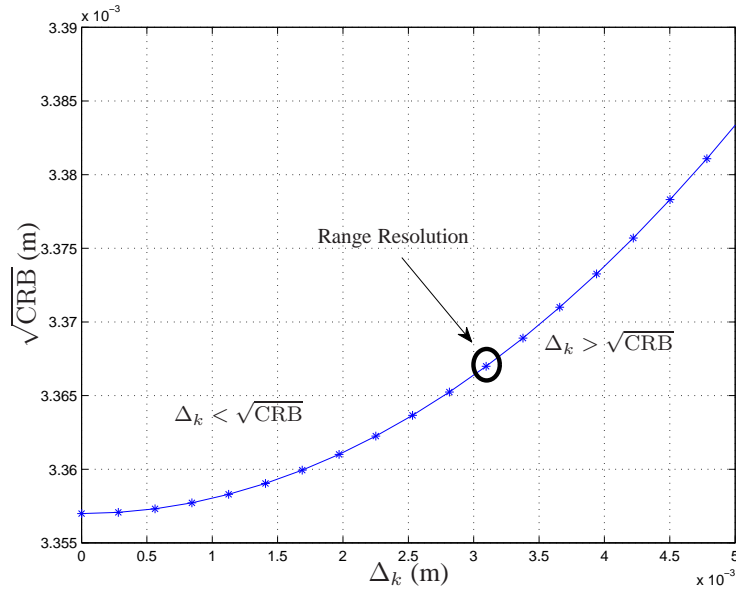


Figure 6.5: This figure shows an example plot of how the range resolution metric is determined. The circled value is the range resolution and corresponds to the location where the square root of the CRB is equal to the range separation. At smaller range separations, the square of the CRB is greater than the separation and vice versa.

Table 6.1: Optimal pulse-width results - two point target

Range Sampling (t_s)	CRB, σ_{pt} (ns)	Simulation, σ_{pt} (ns)
$0.6t_{so}$ (1.126 ns)	0.52	0.52
$0.8t_{so}$ (1.500 ns)	0.70	0.70
t_{so} (1.876 ns)	0.88	0.88
$1.2t_{so}$ (2.251 ns)	1.06	1.04
$1.4t_{so}$ (2.626 ns)	1.22	1.16

6.3.1 Optimal Pulse for Two Point Target. Considering the two point target scenario, Table 6.1 summarizes the optimal pulse-width σ_{pt} CRB and simulation results for several range sampling cases varying from faster ($0.6t_{so}$) to slower ($1.4t_{so}$) electronics. Figure 6.6 shows the data points for each range sampling case. For a particular t_s , changing the pulse to be either narrower or wider than the optimal results in an increase in the bound or variance and deterioration in the range resolution. The minimum value of each curve corresponds to the reported optimal pulse-width.

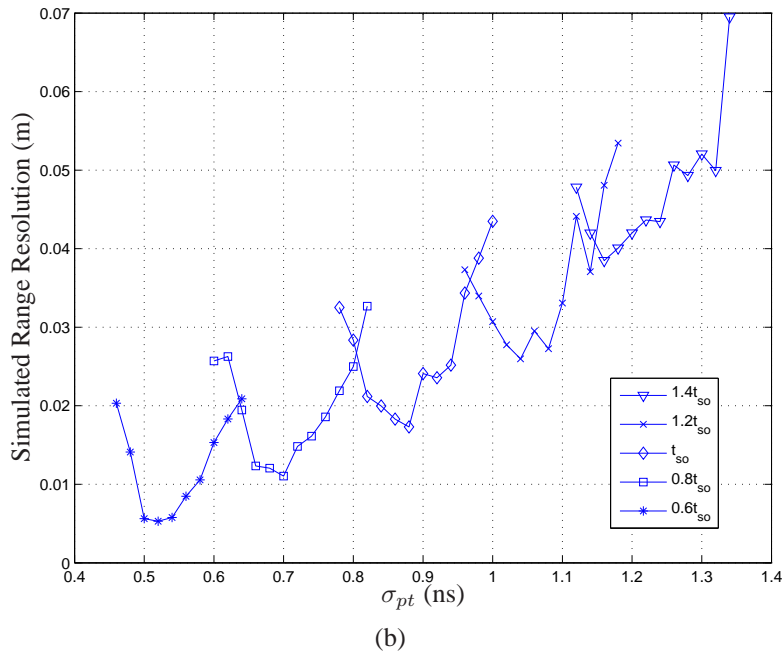
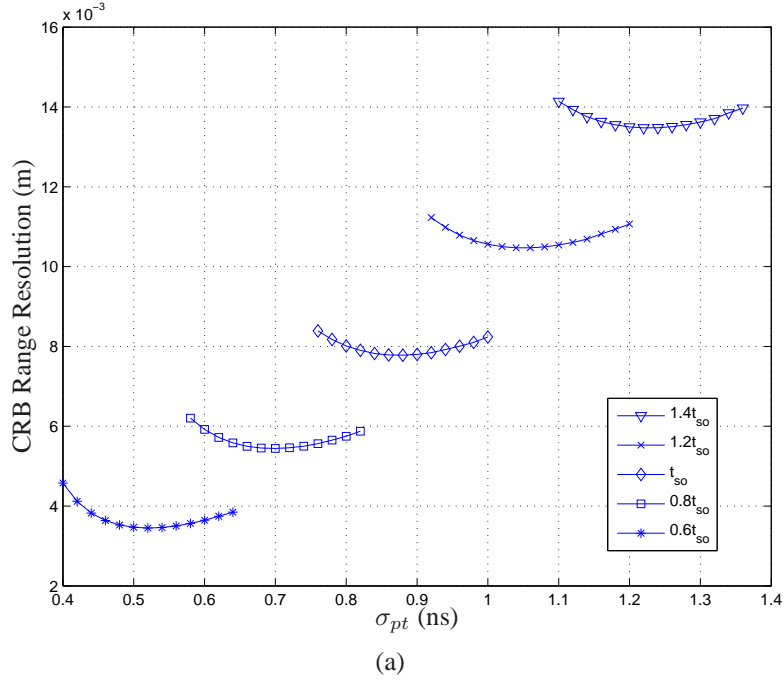


Figure 6.6: (a) For differing range sampling cases, the range resolution derived from the CRB is plotted versus the pulse-width. As the range sampling t_s becomes either faster ($0.6t_{so}$ and $0.8t_{so}$) or slower ($1.2t_{so}$ and $1.4t_{so}$), the optimal pulse-width respectively becomes narrower or wider with a corresponding improvement or degradation in the range resolution. (b) The simulation range resolution determined from the range separation variance is plotted versus the pulse-width. As expected, the resolution values are larger than those predicted by CRB theory. Also, the optimal pulse-width trends in a similar manner as the CRB results.

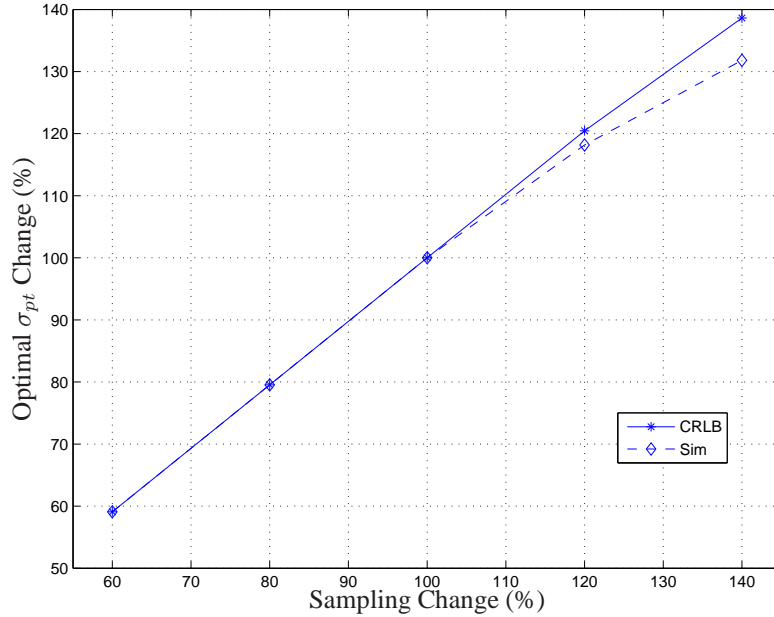


Figure 6.7: Utilizing the optimal σ_{pt} values from Table 6.1, this plot shows the near exact percentage change of the CRB and simulation optimal pulse-widths with respect to the percentage change in range sampling.

As can be seen in Figure 6.7, the optimal pulse-width scales in a similar manner as the range sampling. For example, if the range sampling was reduced by 80%, then the optimal pulse-width also changed by approximately 80% for both the CRB and simulation results.

6.3.2 Optimal Pulse for Complex Targets. The goal of this section is to show through simulation that the optimal pulse-width theory holds for more complex, two surface targets. The CRB theory in Section 6.1 was developed for a simple, two point target and doesn't directly pertain to these new targets. However, since the bound and the ensuing simulation both predict an optimal pulse-width for the simple two point target, intuition dictates that an optimal pulse-width could also be found for more complex targets. Three additional targets are selected (Section 5.2): multi-bar, three-bar, and connected blocks. The first surface of all these targets is a flat, optically reflective board with shapes cut out. The second surface is also flat and optically reflective and is placed behind the first board at a specific range separation. This second surface has no cut-outs. Depending on the target

Table 6.2: Optimal pulse-width results - complex targets

Target	Simulation, σ_{pt} (ns)
Multi-bar	1.1
Three-bar	1.0
Connected blocks	1.0

geometry, blurring strength, and surface reflectivity, a given pixel might contain significant contributions from either one surface or two surfaces. For conciseness, the multi-bar target method and results are discussed in-depth while just the results are shown for the other two.

The method to determine the optimal pulse-width is the exactly the same as the previous section: vary the range separations and accumulate statistics at those separations and choose the pulse-width that produces the minimum range resolution. Particular to this scenario, the pixel-based two surface estimator from Section 4.5 is used to generate the estimates using a threshold of $\gamma = 0.97$. This threshold favors the “one surface pixel” model due to false peaks created by noisy realizations of the incident low-light levels. The first surface (in range) is fixed and assumed known while the second surface is placed at successively larger distances from the first surface. At each range separation, only the pixels classified as “two surface” are used in order to keep the model as close as possible to the simple two-point target CRB of Section 6.1. The estimation statistics collected include variance, mean square error, and bias. Due to the complexity of the target and inherent coupling between adjacent pixels, low light levels (15-30 received photons) were required to increase the effect of the variance on the observed data.

A simulation is set up where the complex targets are interrogated by a 3D FLASH LADAR. Results of the simulation are shown in Table 6.2 and Figures 6.8(b), 6.9(b), and 6.10(b) where the optimal pulse-width standard deviation of 1.0 or 1.1 ns show moderate agreement to the CRB results ($\sigma_{pt} = 0.88$ ns) from the simple, two point target. Again, there is no claim that the results have to match, but that fact that they are close for several different targets is encouraging.

From [5], it was shown that the two-surface estimator is unbiased given a simple scene. However, in order to justifiably compare to the optimal pulse-width predicted by

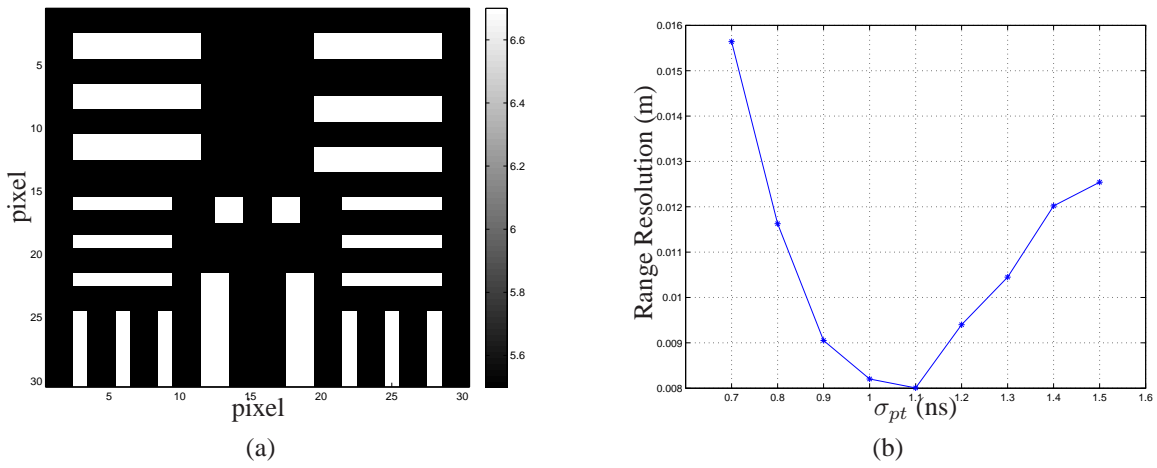


Figure 6.8: (a) True target scene.
 (b) Optimal pulse results using against a complex target with $t_s = t_{so}$.

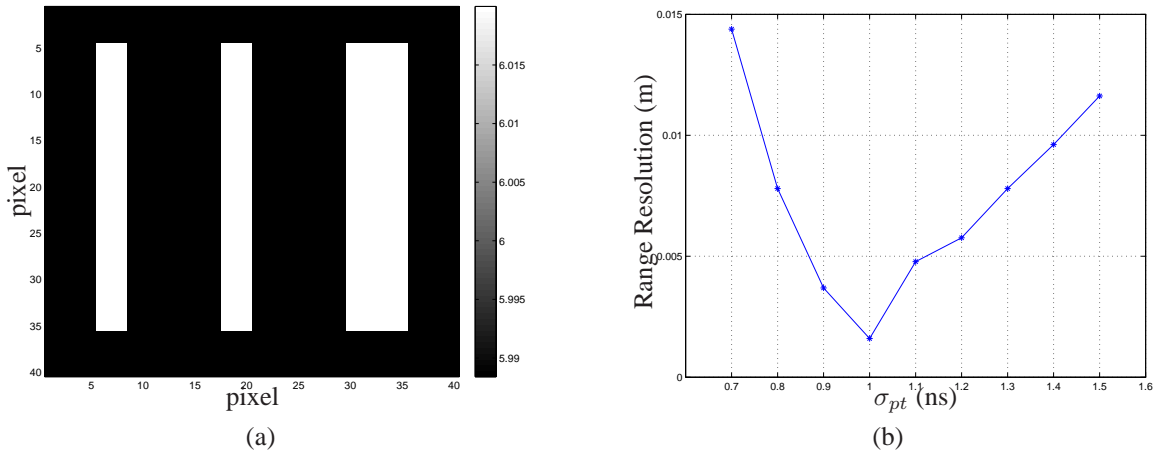


Figure 6.9: (a) True target scene.
 (b) This plot shows the optimal pulse results for a three-bar target with $t_s = t_{so}$.

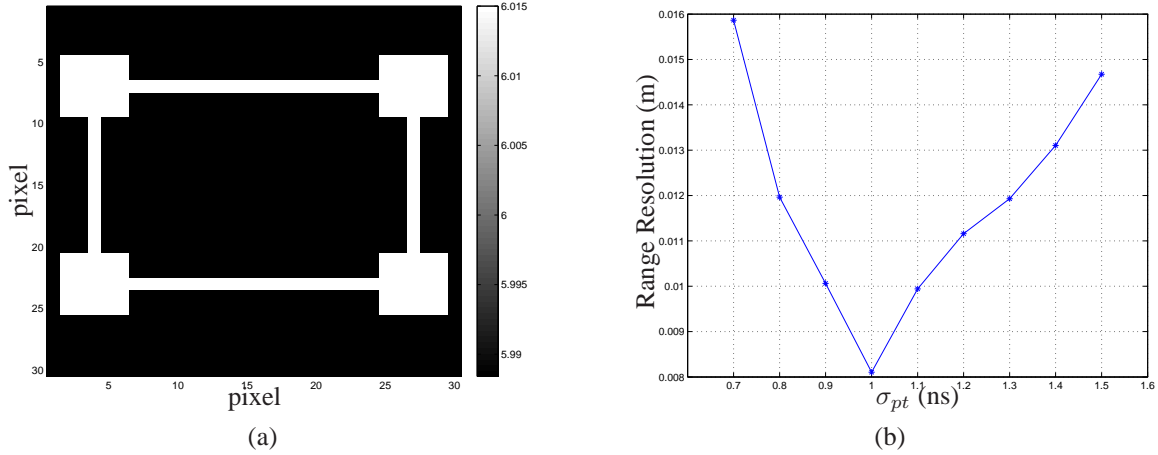
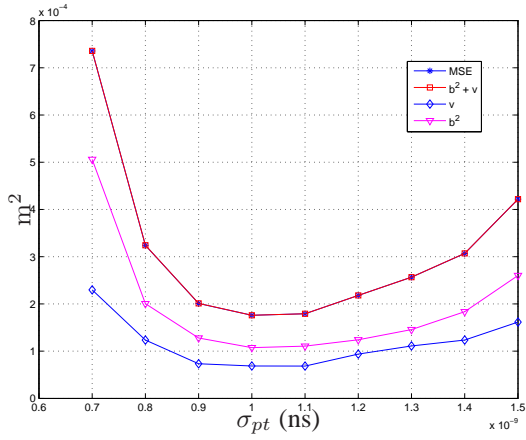


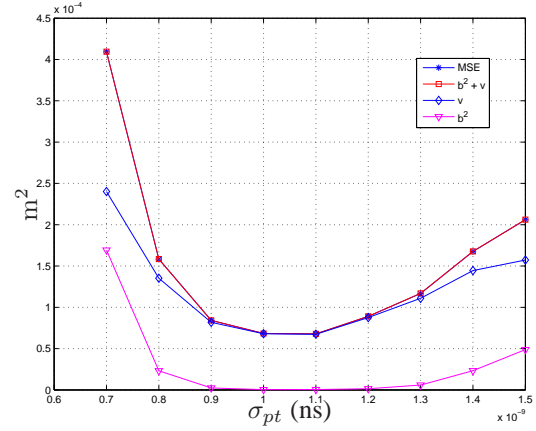
Figure 6.10: (a) True target scene.
 (b) The optimal pulse is shown for a connected blocks target with $t_s = t_{so}$.

the CRB in Section 6.3.3, the estimator must be shown to be unbiased given the complex scenes where the convolution effects introduce severe bias into estimates. Thus, the light levels had to be lowered to levels where the maximum peaks of the observed waveforms are between 15 and 30 photons. This low light level allows for variance to have a significant impact on observed photon counts.

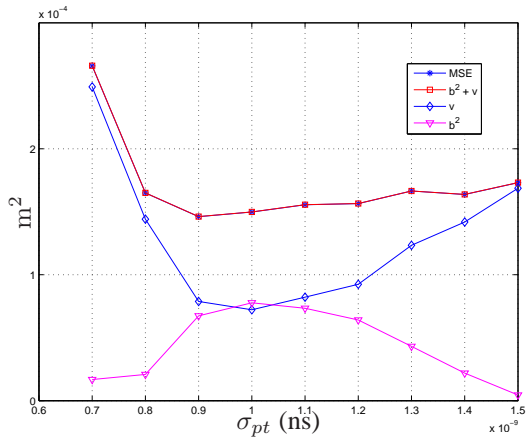
Figures 6.11(a)-(d) and 6.12(a)-(d) show the statistics for different range separations and pulse-widths respectively for the multi-bar target. The significant factor across the plots is that there is a relatively low or non-dominating bias in the region of range separation where the range resolution is selected. This region for best-performing pulse-widths from Figure 6.8(b) ($\sigma_{pt} = 0.9, 1.0, 1.1,$ and 1.2 ns) shows low bias and therefore variance dominance in the MSE near the selected range resolutions of 0.8 to 0.9 centimeters (referring to Figure 6.12(a)-(d)). These results indicate that some regions of the search space (range separation and pulse-width) are more biased than others. The areas that are of most interest tend to be less biased and, thus, permit a conditional comparison to the CRB results. Furthermore, the optimal pulse-width results for the three-bar and connect blocks targets show that their estimation statistics act in a similar manner. With the variance dominating in the areas of interest, the majority of the error lies within the variance allowing for the use of the range resolution metric and subsequent comparison to the CRB results.



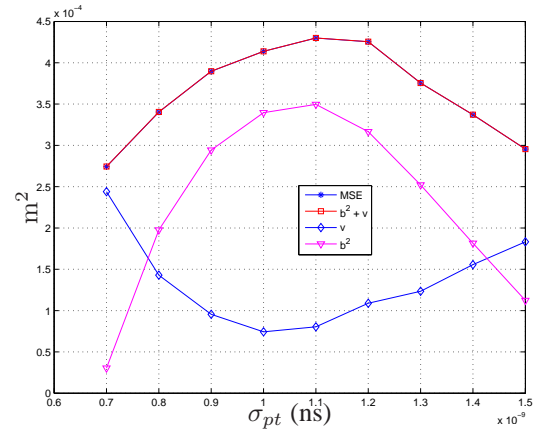
(a)



(b)

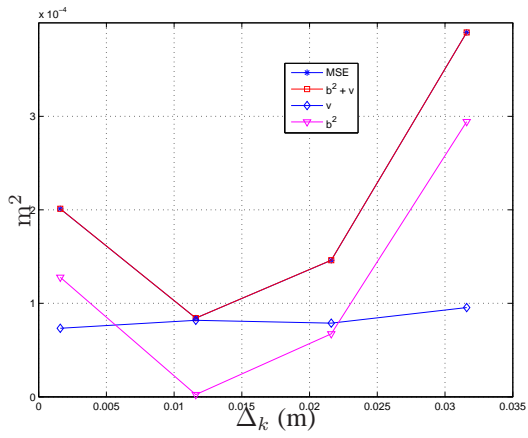


(c)

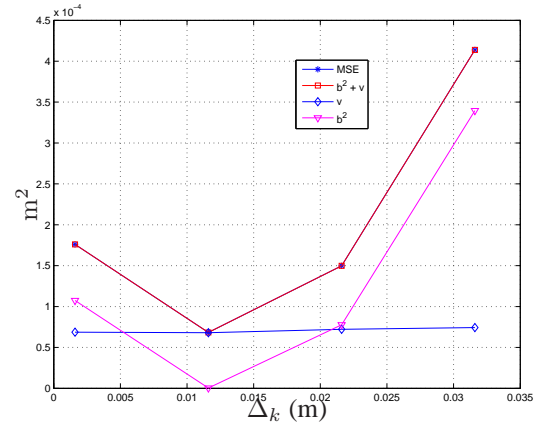


(d)

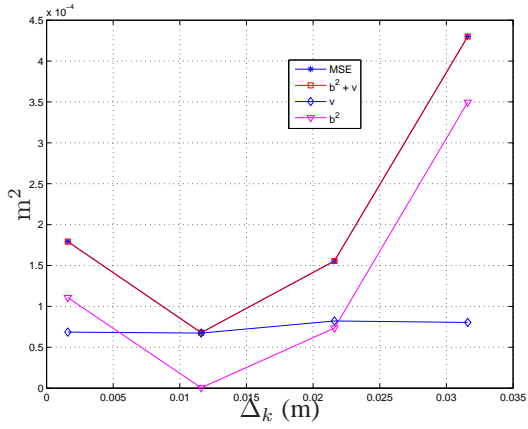
Figure 6.11: Statistics across pulse-widths for various range separations for the multi-bar target. The statistics include mean square error, bias, and range variance.
 (a) Range separation 1.6 mm.
 (b) Range separation 11.6 mm.
 (c) Range separation 21.6 mm.
 (d) Range separation 31.6 mm.



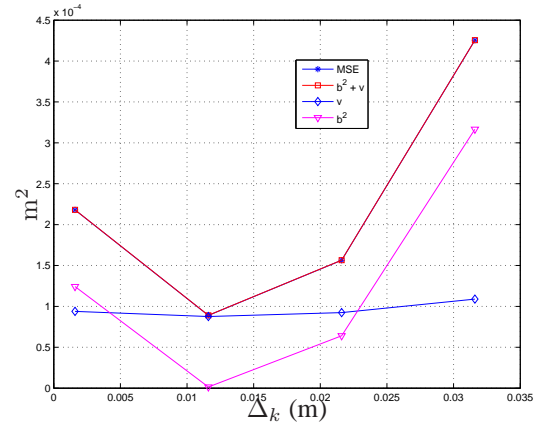
(a)



(b)



(c)



(d)

Figure 6.12: Statistics across range separations for various pulse-widths for the multi-bar target. The statistics include mean square error, bias, and range variance.
 (a) $\sigma_{pt} = 0.9$ ns.
 (b) $\sigma_{pt} = 1.0$ ns.
 (c) $\sigma_{pt} = 1.1$ ns.
 (d) $\sigma_{pt} = 1.2$ ns.

6.3.3 Optimal Pulse for a Two Point Target using Normalized Pulse Definition .

Another method to investigate the optimal pulse-width is to normalize the pulse with respect to the range sampling. Rather than define the width of the pulse by σ_{pt} in units of seconds, the pulse is defined by σ_n in units of samples given by

$$p(n) = \frac{1}{\sqrt{2\pi}\sigma_n} \exp\left\{-\frac{(n)^2}{2\sigma_n^2}\right\} \quad (6.7)$$

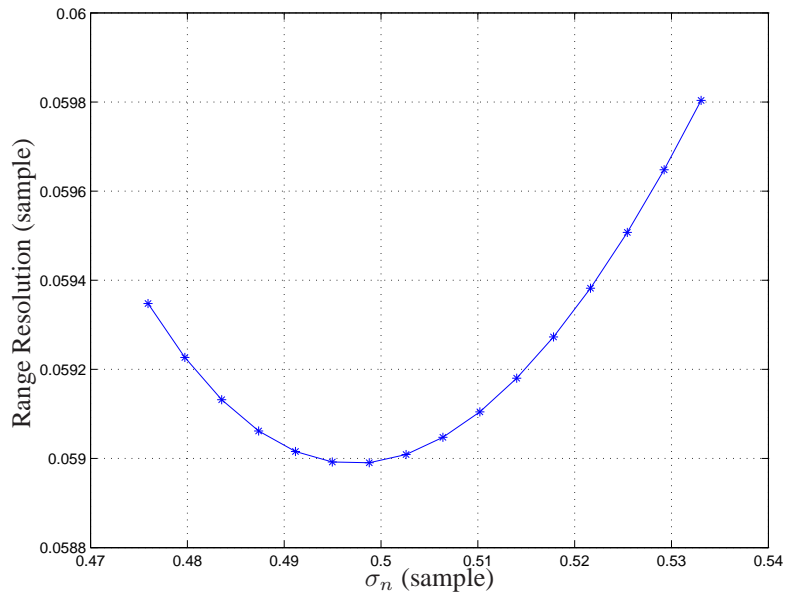
where $n \in [1, N]$ is an integer range sample and the standard deviation is

$$\sigma_n = \frac{\sigma_{pd}}{ct_s} = \frac{c\sigma_{pt}}{ct_s} = \frac{\sigma_{pt}}{t_s} \quad (6.8)$$

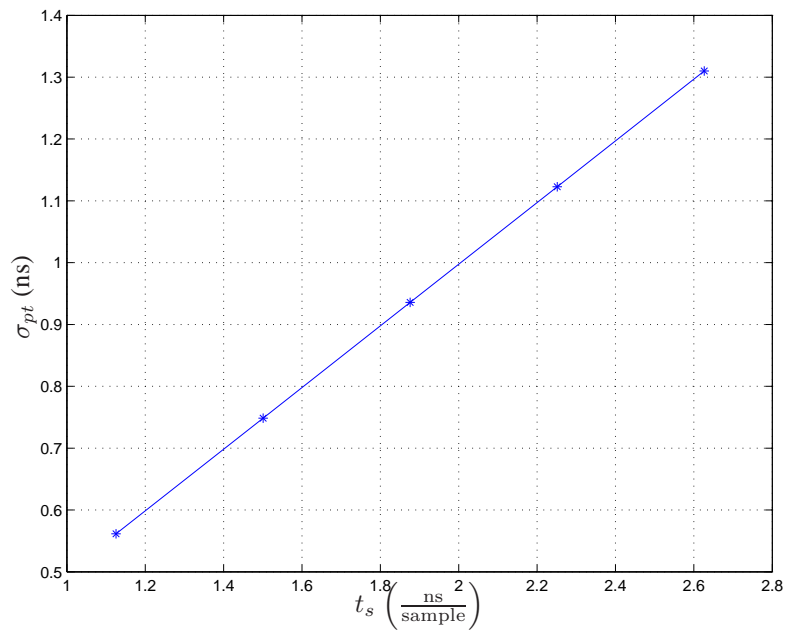
with σ_{pd} as the pulse standard deviation in units of meters, c is the speed of light in meters per seconds, t_s is the range sampling in seconds per sample, and σ_{pt} is the pulse standard deviation in units of seconds. The benefit of this definition is the ability to determine an optimal pulse-width independent of range sampling capability.

Pertaining to the range resolution metric, the optimal pulse standard deviation σ_n is found by using the same investigation procedures as the previous section. Figure 6.13(a) shows the optimal pulse shape in terms of a standard deviation measured in samples. Using Equation (6.8), the optimal standard deviation in seconds σ_{pt} can be found for a particular t_s as seen in Figure 6.13(b). These values for σ_{pt} are consistent with the values from the previous section.

Considering all the above optimal pulse-width studies, an important observation is the number of significant samples across the pulse for the optimal pulse-widths from Tables 6.1, Table 6.2, and the normalized pulse section. In each case, the number of significant samples across the optimal pulse is three. Referring to Figure 4.1(b), a significant sample is defined as a non-zero, sizable contributor ($\geq 2\%$ of pulse peak value) to the waveform. This consistent number of significant samples indicates that more samples (i.e. larger σ_{pt}) than the optimal harms the range resolution capability while fewer samples fails to provide the estimator with enough data and under-samples the received pulse causing the variance



(a)



(b)

Figure 6.13: (a) Using the normalized pulse model, this graph shows the CRB optimal pulse standard deviation referring to Equation (6.7).
 (b) CRB optimal pulse versus range sampling. The optimal pulse width changes proportionally as the sampling changes.

to increase. Even for a complex target whose estimation variance is not described by the CRB theory, the simulated optimal pulse-width still maintains the three significant samples.

6.4 Conclusions

The CRB is used to bound system performance by giving a measure of how well an unbiased estimator can perform. In this paper, the CRB bounds the performance on the ability to estimate the range separation of two spatial point targets. Using the point target estimator, the unbiased estimator variance is shown to be bounded by the CRB with both trending in a similar manner.

Additionally, the CRB can be used to not only predict performance, but to give a LADAR engineer the capability to predict critical LADAR performance without regard to the particulars of estimation. Considering the optimal pulse-width study, all the range sampling cases produced an optimal pulse-width with a similar number of significant samples across the pulse. Three significant samples across the pulse provides the best range resolution while not experiencing the ill-effects of under-sampling.

The overriding conclusion is that a shorter pulse-width in the femtoseconds does not always provide improved range resolution performance. There is a range resolution performance link between the electrical circuitry sampling capability and the width of the transmitted pulse. In conjunction with other performance goals and design limitations, the LADAR engineer concerned about range resolution should not just focus on a shorter pulse-width without making improvements in the receiver's capability to sample the detected return pulses.

VII. Summary

The contributions of this research increase the body of knowledge and the ultimate performance of three dimensional FLASH LAsER Detection And Ranging (3D FLASH LADAR). By decreasing ranging error, characterizing estimation performance, or optimizing system parameters, sensor capability has been enhanced. This increase is aided by an increase in the data model fidelity from previous contributions in the field which have all but ignored the spatial blurring effect of the image formation process. By incorporating these blurring effects, new problems and opportunities to exploit the data were formed. Solutions were subsequently found that took advantage of the “extra” information available.

Given 3D FLASH LADAR’s future in imaging, computer vision, guidance, navigation, and targeting, this work builds a basis of understanding concerning data models and data processing. The research has unique attributes that are rare considering other other signal processing research. The 3D FLASH LADAR is a powerful sensor combining RADAR principles, laser transmission, waveform processing, and electro-optical phenomena and requires equally powerful algorithms to estimate and characterize parameters of interest. The focus of this research centers around a particular parameter: target range. Although, other areas of research may be possible given that it is shown that a particular data model appropriately characterizes data from a 3D FLASH LADAR sensor.

This chapter summarizes the previous chapters in the document, reviews the significant research contributions, and outlines several avenues for future research.

7.1 Chapter Summary

Chapter II provided background theory related to imaging, coherence, deconvolution, maximum likelihood principles, and generalized expectation maximization. It also presented the data model used prevalently in this dissertation. Finally, previous research was summarized in the areas of 3D LADAR hardware and data processing, blind deconvolution, performance bounding, and parameter optimization.

Chapter III detailed the 3D FLASH LADAR hardware and laboratory settings used in experimental collects. This chapter also describes the procedures used to condition the data

for appropriate use for the selected mathematical model. Finally, it explains how the experimental point-spread-function is determined as well as the speckle parameter estimation which increases confidence with the chosen incoherent light model.

Chapter IV contained the pertinent range estimation algorithms to include peak detection, maximum likelihood, normalized cross-correlation (matched filtering), a two point target range and spatial separation estimator, and a two surface range separation estimator. The normalized cross-correlation is usually the method of choice due to its ability to perform intersample ranging and handle truncated waveforms. Although, it may encounter some bias depending on spatial blurring severity and/or the effectiveness of deblurring (deconvolution) algorithms.

Chapter V implemented object deconvolution and blind deconvolution on blurry, noisy data observations using simulation and experimental data showing that object recovery *improves* range estimation.

Chapter VI derived the CRB for range and spatial separation as well as amplitude estimation considering a two-point target scene. Considering several range sampling cases, the range separation CRB and estimator also predicted an optimal pulse-width that provides the best range resolution. Additionally, an optimal pulse-width is found using more complex targets and for a normalized pulse-definition.

7.2 *Summary of Contributions*

7.2.1 Improving Range Estimation by Spatial Processing. The benefits of spatial processing are evident when comparing range estimation before and after the object recovery algorithms. Simulation shows substantial increase in the image quality and decrease in the range estimation errors. The experimental data shows improvement, but not as dramatic due primarily to the excess speckle noise evident in the data. A favorable result is that the blind deconvolution methods outperformed deconvolution even when the deconvolution was given the exact form of the blurring function. The ability to process three-dimensional data in two dimensions and range in the third dimension was the innovative vision. This

contribution proves that this vision can be theoretically proven and demonstrated through simulation and experimentation.

7.2.2 Unbiased Two Point Target Temporal and Spatial Estimator. Using a two-point target scene, an unbiased spatial-temporal estimator is derived that is able to accurately estimate spatial and range separations and received amplitudes. Through simulation, its range separation estimator variance compares favorably to that predicted by the CRB. This estimator can even handle truncated waveforms which is not predicted or suitable handled by the bound. Without this unbiased estimator, the CRB results would have nothing to compare to and there would be less confidence its conclusions. The agreement between the CRB and simulation variance is exceptionally significant and vital since they arrive at virtually the same answer by different methods.

7.2.3 Lower Bound on Range Separation Estimation. Through the use of a two-point target scene, the CRB on range separation estimation is derived. The CRB on spatial separation and amplitude estimation is derived as well. Pertaining to range separation, the CRB shows that range separation does not severely affect estimation performance until the targets are close. When the range separation is identically zero, the bound does not go to zero due to the spatial blurring still present in the data (targets are still spatially separated). Additionally, the shape of the bound is remains constant independent of several parameters including spatial blurring strength, signal-to-noise ratio (SNR) of the reflectors, and spatial separation. The dependence between the bound and the parameters is the absolute level of the CRB. As the blurring strength increases, the bound also increases and vice versa. When the SNR of the unknown target reflector is either increased or decreased, the bound acts oppositely and decreases or increases respectively. These results should be intuitive where increased blurring would make estimation more difficult (i.e. variance would increase) and an increase in the unknown target SNR would enhance the estimation abilities (i.e. variance would decrease).

7.2.4 Optimal Pulse-Width based on Range Resolution. With this contribution, it is shown that the CRB can perform system parameter optimization with respect to a very important system characteristic and requirement – range resolution. Independent of estimator choice, the bound shows that an optimal pulse-width exists whereby the expected range resolution is minimized. After developing an unbiased estimator for the target scene, the optimal pulse-widths predicted by the CRB are verified through simulation. The agreement between CRB and simulation is very significant given that they arrive at range separation variance either through Fisher information theory or through repeated trials using a simulation.

Furthermore, the range sampling interval is both increased (slower electronics) and decreased (faster electronics) which shows the resultant optimal pulse-shape becoming wider and narrower respectively. In other words, faster electronics that sample the range dimension faster can incorporate a narrower pulse-width and achieve better range resolution. To lend confidence to the results, optimal pulse-widths are also found for more complex targets. Also, in terms of samples, an optimal pulse-width using the CRB is found using a normalized pulse model. This definition means that the results are independent of the range sampling interval. Finally, and perhaps most enlightening, all the optimal pulse-width results reflect that the received pulse needs to have three significant samples in the received data. Fewer significant samples caused by a narrower transmitted pulse or target interactions does not provide enough information to match the model pulse-shape and could even be entirely missed by the electronics. Following, while providing enough information, more significant samples would certainly be less optimal by degrading range resolution performance.

7.3 Future Research

There are numerous additional research avenues available with respect to 3D FLASH LADAR and data processing including the following:

7.3.1 Outlier Detection. To overcome speckle produced by coherent lasers and increase signal-to-noise ratio (SNR) because of low return signal levels due to low transmit energy, propagation distances, or target reflectance, 3D LADAR systems may need to average many cubes of scene data. In practice, certain cubes may be warped due to misregistration or atmospheric effects. Also, a particular pixel may be defective for a small amount of time resulting in an out-of-family pixel that is “warped” in a cube of data. If the warping is severe enough, the averaging process may be negatively affected by these particular cubes or pixels. It would be advantageous to system performance (i.e. object recovery, range estimation) to develop a means to intelligently remove these frames before the averaging process.

7.3.2 Foliage PENetration (FOPEN) Capability Investigation. A key military mission for any imaging or ranging sensor is the ability to recognize man-made targets under foliage that can either be man-made itself (camouflage) or natural (trees). Successful, experimental efforts have already been accomplished trying to ascertain the 3D FLASH LADAR’s FOPEN capability. However, a rigorous theoretical model has not been adopted yet. This model and subsequent simulation and experimental investigation would numerically characterize FOPEN potential in a myriad of environments including different camouflage configurations, look angles, weather conditions (e.g. wind velocity), and targets.

7.3.3 Pixel Impulse Response Deconvolution. As with any high-performance military hardware, characterization under environmental operational conditions is a mandatory exercise. The operator must know the limits where one would expect nominal performance. As part of the hardware characterization efforts, the pixel impulse response impact on the reflected pulse is important when developing accurate pulse models. The pixel’s impulse response is not ideal and does have some distortion effect on the returned waveforms. Using simulated and experimental data, the research effort would calculate the distortion severity and dependence on system parameters.

7.3.4 *Object blind deconvolution using partially coherent light model.* Described by the Poisson distribution, the incoherent light model used in this research is an approximation for the partially coherent model which is the most accurate portrayal of the detected laser light. Detected partially coherent light is statistically described by the negative binomial (NB) distribution. Blind deconvolution methods using the NB distribution are cumbersome and nearly intractable unless the point-spread-function can be parameterized. If an object estimation method can be found to use the Generalized Expectation Maximization (GEM) algorithm with the NB distribution, the resulting estimator would theoretically outperform the object estimator in this research due to the increase in noise model accuracy. The key issue in the derivation comes when taking the conditional expectation of the log of the complete data with respect to the incomplete data and the old estimates. A vital property of the Poisson distribution is that a sum of Poisson random variables is still Poisson. The same cannot be said for a sum of NB random variables. Consequently, a variation of the GEM or data model is necessary to complete the derivation.

Bibliography

1. Armstrong, Ernest and Richard Richmond. “The Application of Inverse Filters to 3D Microscanning of LADAR Imagery”. *IEEE Aerospace Conference*. 2006.
2. Ayers, G.R. and J.C. Dainty. “Iterative blind deconvolution method and its applications”. *Journal of the Optical Society of America*, 13(7), 1988.
3. Biggs, David and Mark Andrews. “Asymmetric iterative blind deconvolution of multiframe images”. *SPIE Conference on Advanced Signal Processing Algorithms, Architectures, and Implementations VIII*, volume 3461, 328–338. 1998.
4. Buller, G.S. and A.M. Wallace. “Ranging and Three-Dimensional Imaging Using Time-correlated Single-Photon Counting and Point-by-Point Acquisition”. *IEEE Journal of Selected Topics in Quantum Electronics*, 13(4), 2007.
5. Burris, Charles R. *An Estimation Theory Approach to Detection and Ranging of Obscured Targets in 3-D LADAR Data*. Master’s thesis, Air Force Institute of Technology, 2006. <http://handle.dtic.mil/100.2/ADA449928>.
6. Busck, Jens and Henning Heiselberg. “High accuracy 3-D laser radar”. *Proc. of SPIE*, 5412:257–263, 2004.
7. Cain, Stephen C. “Deconvolution of laser pulse profiles from 3D LADAR temporal returns”. *Proc. of SPIE*, 5558, 2004.
8. Cain, Stephen C. “EENG 680: Image Processing”. Course notes, Air Force Institute of Technology 2004.
9. Cain, Stephen C., Richard Richmond, and Ernest Armstrong. “Flash light detection and ranging accuracy limits for returns from single opaque surfaces via Cramer-Rao bounds”. *Applied Optics*, 45(24):6154–6162, August 2006.
10. Cannata, Richard, William Clifton, Steven Blask, and Richard M. Marinob. “Obscuration Measurements of Tree Canopy Structure Using a 3D Imaging Ladar System”. *Proc. of SPIE*, 5412, 2004.

11. Canny, J. "A computational approach to edge detection". *IEEE Trans. Pattern Anal. Mach. Intell.*, 8(6):679–698, 1986.
12. Cho, Peter, Hyrum Anderson, Robert Hatch, and Prem Ramaswami. "Real-Time 3D Ladar Imaging". *Proc. of SPIE*, 6325, 2006.
13. Cooley, James W. and John W. Tukey. "An Algorithm for the Machine Calculation of Complex Fourier Series". *Math. Comput.*, 19:297–301, 1965.
14. Craig, R., I. Gravseth, R. P. Earhart, J. Bladt, S. Barnhill, L. Ruppert, and C. Centamore. "Processing 3D Flash LADAR Point-Clouds in Real-time for Flight Applications". *Proc. of SPIE*, 6555, 2007.
15. Dabov, K., A. Foi, V. Katkovni, and K. Egiazarian. "Image restoration by sparse 3D transform-domain collaborative filtering". *Proc. of SPIE*, 6812, 2008.
16. Dempster, Arthur P., Nan M. Laird, and Donald B. Rubin. "Maximum likelihood from incomplete data via the EM algorithm". *Statistical Society*, 1977.
17. Dion, Bruno and Nick Bertone. "An overview of avalanche photodiodes and pulsed lasers as they are used in 3D laser radar type applications". *Proc. of SPIE*, 5435:187–195, 2004.
18. Dolne, J.J., D. Gerwe, , and M. Johnson. "Performance of Three Reconstruction Methods on Blurred and Noisy Images of Extended Scenes". *Proc. of SPIE*, 3815, 1999.
19. Dries, J. Christopher, Brian Miles, and Roger Stettner. "A 32 x 32 Pixel FLASH Laser Radar System Incorporating InGaAs PIN and APD Detectors". *Proc. of SPIE*, 5412.
20. Eriksson, Jonny and Mats Viberg. "On Cramer Rao Bounds and Optimal Beamspace Transformation in Radar Array Processing". *Phased Array Systems and Technology, 1996., IEEE International Symposium on*, 301 –306. 1996.
21. Fish, D.A., A.M. Brinicombe, and E.R. Pike. "Blind deconvolution by means of the Richardson-Lucy algorithm". *Optical Society of America*, 12, No.1, 1995.

22. Gelbart, Asher, Chris Weber, Shannon Bybee-Driscoll, Jonathan Freeman, Gregory J. Fetzer, Tom Seales, Karen A. McCarley, and Jim Wright. "FLASH lidar data collections in terrestrial and ocean environments". *Proc. of SPIE*, 5086:27–38, 2003.
23. Gerchberg, R.W. and W.O. Saxton. "A Practical Algorithm for the Determination of Phase from Image and Diffraction Plane Pictures". *Optik*, 35(2), 1971.
24. Goodman, Joseph W. *Statistical Optics*. McGraw-Hill, Inc., New York, NY, 1985.
25. Goodman, Joseph W. *Introduction to Fourier Optics*. Roberts & Company, Englewood, Colorado, 2005.
26. Greer, D.R., R. Fung, and J.H. Shapiro. "Maximum-Likelihood Multiresolution Laser Radar Range Imaging". *IEEE Transactions on Image Processing*, 6(1), 1997.
27. de Haag, Maarten Uijt, Don Venable, and Mark Smearcheck. "Use of 3D laser radar for navigation of unmanned aerial and ground vehicles in urban and indoor environments". *Proc. of SPIE*, 6550, 2007.
28. Hagen, Nathan, Matthew Kupinski, and Eustace L. Dereniak. "Gaussian profile estimation in one dimension". *Applied Optics*, 46(22):5374–5383, 2007.
29. Halmos, Maurice J. "Eyesafe 3-D FLASH LADAR for targets under obscuration". *Proc. of SPIE*, 5086:70–83, 2003.
30. Hecht, Eugene. *Optics*. Addison Wesley, New York, 4th edition, 2002.
31. Heinrichs, Richard, Brian Aull, Richard Marino, Daniel Fouche, and Alexander McIntosh. "Three-Dimensional Laser Radar with APD Arrays." *Proc. of SPIE*, 4377.
32. Hernandex-Marin, Sergio, Andrew Wallace, and Gavin Gibson. "Bayesian Analysis of Lidar Signals with Multiple Returns." *IEEE Transactions on Pattern Analysis and Machine Intelligence*, 2007.
33. Hernandex-Marin, Sergio, Andrew Wallace, and Gavin Gibson. "Multilayered 3D LiDAR Image Construction using Spatial Models in a Bayesian Framework." *IEEE Transactions on Pattern Analysis and Machine Intelligence*, 2008.

34. Holmes, T.J. “Blind deconvolution of quantum-limited incoherent imagery: maximum-likelihood approach”. *Journal of the Optical Society of America*, 9(7), 1992.
35. Hong, Seung-Hyun and Bahram Javidi. “Three-dimensional optimum filter for detecting distorted LADAR image in disjoint background noise”. *Proc. of SPIE*, 5243, 2003.
36. Hong, SeungHyun and Bahram Javidi. “Three-dimensional optimum nonlinear filter for detecting distorted target location and distance”. *Proc. of SPIE*, 4864, 2002.
37. Jain, Anil K. *Fundamentals of Digital Image Processing*. Prentice Hall, New Jersey, 1989.
38. Johnson, Steven. *Range precision of LADAR Systems*. Ph.D. thesis, Air Force Institute of Technology, 2008. <http://handle.dtic.mil/100.2/ADA488211>.
39. Johnson, Steven and Stephen C. Cain. “Bound on range precision for shot-noise limited ladar systems”. *Applied Optics*, 47(28):5147–5154, October 2008.
40. Jr., Robert D. Habbit, Robert O. Nellums, Aaron D. Niese, and Jose L. Rodriguez. “Utilization of Flash LADAR for Cooperative & Uncooperative Rendezvous and Capture”. *Proc. of SPIE*, 5088:146–157, 2003.
41. Khoury, J., C. L. Woods, J. Lorenzo, J. Kierstead, D. Pyburn, and S. K. Sengupta. “Resolution Limits in Imaging LADAR Systems”. *Proc. of SPIE*, 5437, 2004.
42. Kundur, Deepa and Dimitrio Hatzinakos. “Blind Image Deconvolution”. *IEEE Signal Processing Magazine*, May 1996.
43. Kundur, Deepa and Dimitrio Hatzinakos. “Blind Image Deconvolution Revisited”. *IEEE Signal Processing Magazine*, November 1996.
44. van der Laan, D. J., Marnix C. Maas, Dennis R. Schaart, Peter Bruyndonckx, Sophie Leonard, and Carel W. E. van Eijk. “Using CramerRao Theory Combined With Monte Carlo Simulations for the Optimization of Monolithic Scintillator PET Detectors”. *Nuclear Science, IEEE Transactions*, 53(3):1063–1070, 2006.

45. Lamoreux, James, James Siekierski, and J.P. Nick Carter. "Space Shuttle Thermal Protection System Inspection by 3D Imaging Laser Radar." *Proc. of SPIE*, 5412.
46. Lane, R.G. "Blind Deconvolution of Speckle Images". *Optical Society of America*, 1992.
47. Leung, W-Y.V. and R.G. Lane. "Blind deconvolution of images blurred by atmospheric speckle". *Proc. of SPIE*, 4123, 2000.
48. Li, Jian, Luzhou Xu, Petre Stoica, Keith Forsythe, and Daniel Bliss. "Range Compression and Waveform Optimization for MIMO Radar: A Cramer-Rao Bound Based Study". *Signal Processing, IEEE Transactions on*, 56(1):218–232, 2008. ISSN 1053-587X.
49. Linnehan, Robert, David Brady, John Schindler, Leonid Perlovsky, and Muralidhar Rangaswamy. "On the Design of SAR Apertures using the Cramer-Rao Bound". *Aerospace and Electronic Systems, IEEE Transactions on*, 43(1):334–355, 2007.
50. Lucy, L.B. "An iterative technique for the rectification of observed distributions". *The Astronomical Journal*, 1974.
51. MacDonald, Adam and Stephen Cain. "Derivation and Application of an Anisoplanatic Optical Transfer Function for Blind Deconvolution of Laser Radar Imagery". *Proc. of SPIE*, 5896, 2005.
52. MacDonald, Adam, Stephen C. Cain, and Ernest Armstrong. "Maximum a posteriori image and seeing condition estimation from partially coherent two-dimensional light detection and ranging images". *Optical Engineering*, 2006.
53. Mahalanobis, Abhijit and Alan J Van Nevel. "Performance of Multi-Dimensional Algorithms for Target Detection in LADAR Imagery". *Proc. of SPIE*, 4789, 2002.
54. McLachlan, Geoffrey J. and Thriyambakam Krishnan. *The EM Algorithm and Extensions*. John Wiley & Sons, Inc., New Jersey, 2nd edition, 2008.
55. McMahan, Jason R., Stephen C. Cain, and Richard K. Martin. "Improving 3-D LADAR range estimation via spatial filtering". *IEEE Aerospace Conference*. 2009.

56. McMahon, Jason R., Richard K. Martin, and Stephen C. Cain. “3D FLASH LADAR Range Estimation via Blind Deconvolution”. *Journal of Applied Remote Sensing*, 4:043517, 2010. URL <http://link.aip.org/link/?JRS/4/043517/1>.
57. Moseley, General T. Michael. “The Nations Guardians Americas 21st Century Air Force”. *CSAF White Paper*, 2007.
58. Murray, James T., Steve E. Moran, Nick Roddier, Rick Vercillo, Robert Bridges, and William Austin. “Advanced 3D polarimetric flash ladar imaging through foliage”. *Proc. of SPIE*, 5086, 2003.
59. Oppenheim, Allen V., Ronald W. Shafer, and Thomas G. Stockham. “Nonlinear Filtering of Multiplied and Convolved Signals”. *Proceedings of the IEEE*, 56:1264–1291.
60. Papoulis, A. and S.U. Pillai. *Probability, Random Variables and Stochastic Processes*. McGraw-Hill, New York, 2002.
61. R. P. Millane, P. J. Bones and H. Jiang. “Blind Deconvolution for Multidimensional Images”. *IEEE*, 1994.
62. Richardson, W.H. “Bayesian-Based Iterative Method of Image Restoration”. *Journal of the Optical Society of America*, 62(1), 1972.
63. Richmond, Richard and Stephen Cain. *Direct-Detection LADAR Systems*. SPIE Publications, Washington, USA, 2010.
64. Richmond, Richard, Roger Stettner, and Howard Bailey. “Laser radar focal plane array for three-dimensional imaging”. *Proc. of SPIE*, 2748, 1996.
65. Richmond, Richard, Roger Stettner, and Howard Bailey. “Laser radar focal plane array for three-dimensional imaging (Update)”. *Proc. of SPIE*, 3065, 1997.
66. Richmond, Richard, Roger Stettner, and Howard Bailey. “Laser radar focal plane array for three-dimensional imaging (Update)”. *Proc. of SPIE*, 3380, 1998.
67. Roggemann, Michael C. and Byron Welsh. *Imaging Through Turbulence*. CRC Press, New York, 1996.

68. Rosenbush, Gavin, Tsai Hong, and Roger D. Eastman. "Super-Resolution Enhancement of Flash LADAR Range Data". *Proc. of SPIE*, 6736, 2007.
69. Rye, Barry J. and R. Michale Hardesty. "Discrete Spectral Peak Estimation in Incoherent Backscatter Heterodyne Lidar. I: Spectral Accumulation and the Cramer-Rao Lower Bound". *Geoscience and Remote Sensing, IEEE Transactions on*, 31(1):16–27, 1993.
70. Schroeder, Daniel J. *Astronomical optics*. Academic Press, 2nd edition, 2000.
71. Schulz, Timothy J. "Multiframe blind deconvolution of astronomical images". *Optical Society of America*, 10, No. 5, 1993.
72. Söderman, Ulf, Simon Ahlberg, Magnus Elmqvist, and Åsa Persson. "Three-dimensional environment models from airborne laser radar data". *Proc. of SPIE*, 5412, 2004.
73. Seal, Michael D. *Nonlinear Time-Variant Response in an Avalanche Photodiode Array based Laser Detection and Ranging System*. Master's thesis, Air Force Institute of Technology, 2007. [Http://handle.dtic.mil/100.2/ADA469310](http://handle.dtic.mil/100.2/ADA469310).
74. Shepherd, O., A.J. LePage, G. Wyntjes, and T.F. Zehnpfennig. "Counter sniper 3-D laser radar". *SPIE Sensor Law Enforcement Conference*, 3577.
75. Shepp, L.A. and Y. Vardi. "Maximum-likelihood reconstruction for emission tomography". *IEEE Transactions on Medical Imaging*, MI-1(2):113–122, 1982.
76. Skolnik, Merrill I. *Introduction to RADAR Systems*. McGraw-Hill, New York, 3rd edition, 2002.
77. Stann, Barry, Mark Giza Brian C. Redman, William Lawler, and John Dammann. "Chirped amplitude modulation ladar for range and Doppler measurements and 3-D imaging". *Proc. of SPIE*, 6550, 2007.
78. Steinvall, Ove, Lena Kiasen, Christina Grnwall, Ulf Söderman, Simon Ahlberg, Asa Persson, Magnus Elmqvist, Hkan Larsson, Dietmar Letalick, Pierre Andersson, Tomas

- Carlsson, and Markus Henriksson. “3 D laser sensing at FOI overview and a system perspective”. *Proc. of SPIE*, 5412:294–309, 2004.
79. Steinvall, Ove, Hakan Larsson, Frank Gustafsson, Tomas Chevalier, Asa Persson, and Lena Klasen. “Characterizing targets and backgrounds for 3-D laser radars”. *Proc. of SPIE*, 5613, 2004.
80. Steinvall, Ove, Hkan Larsson, Frank Gustafsson, Dietmar Letalick, Tomas Chevalier, sa Persson, and Pierre Andersson. “Performance of 3-D laser radar through vegetation and camouflage”. *Proc. of SPIE*, 5792, 2005.
81. Stettner, Roger, Howard Bailey, and Richard D. Richmond. “Eye-safe laser radar 3-D imaging”. *Proc. of SPIE*, 5412, 2004.
82. Stockham, Thomas G., Thomas M. Cannon, and Robert B. Ingebretsen. “Blind deconvolution through digital signal processing”. *Proceedings of the IEEE*, 1975.
83. Sundaramurthy, P. and M.A. Niefeld. “Super-resolved laser ranging using the Viterbi algorithm”. *Quantum Electronics and Laser Science Conference*. 2005.
84. van Trees, Henry L. *Detection, Estimation, and Modulation Theory*. John Wiley & Sons, Inc., New York, 2001.
85. Ullrich, Andreas, Nikolaus Studnicka, and Johannes Riegl. “Hybrid 3D laser sensor based on a high-performance long-range widefield-of-view laser scanner and a calibrated high-resolution digital camera”. *Proc. of SPIE*, 5412, 2004.
86. Vadlamani, Ananth K. and Maarten Uijt de Haag. “Aerial Vehicle Navigation over Unknown Terrain Environments using Inertial Measurements and Dual Airborne Laser Scanners or Flash LADAR”. *Proc. of SPIE*, 6550, 2007.
87. Vural, Cabir and William A. Sethares. “Blind deconvolution of noisy blurred images via disperion minimization”. *IEEE 14th International Conference on Digital Signal Processing*, volume 2, 787–790. 2002.
88. Weiner, Andrew. *Ultrafast Optics*. John Wiley & Sons, Inc., New York, 2009.

89. Winick, Kim. “Cramer-Rao lower bounds on the performance of charge-coupled-device optical position estimators”. *J. Opt. Soc. Am. A*, 3(11):1809–1815, 1986.

REPORT DOCUMENTATION PAGE

*Form Approved
OMB No. 074-0188*

The public reporting burden for this collection of information is estimated to average 1 hour per response, including the time for reviewing instructions, searching existing data sources, gathering and maintaining the data needed, and completing and reviewing the collection of information. Send comments regarding this burden estimate or any other aspect of the collection of information, including suggestions for reducing this burden to Department of Defense, Washington Headquarters Services, Directorate for Information Operations and Reports (0704-0188), 1215 Jefferson Davis Highway, Suite 1204, Arlington, VA 22202-4302. Respondents should be aware that notwithstanding any other provision of law, no person shall be subject to a penalty for failing to comply with a collection of information if it does not display a currently valid OMB control number.

PLEASE DO NOT RETURN YOUR FORM TO THE ABOVE ADDRESS.

1. REPORT DATE (DD-MM-YYYY) 16-09-2010		2. REPORT TYPE Doctoral Dissertation		3. DATES COVERED (From - To) September 2007-September 2010	
4. TITLE AND SUBTITLE Improving Range Estimation of a 3D FLASH LADAR via Blind Deconvolution				5a. CONTRACT NUMBER	
				5b. GRANT NUMBER	
				5c. PROGRAM ELEMENT NUMBER	
6. AUTHOR(S) McMahon, Jason, R., Major, USAF				5d. PROJECT NUMBER	
				5e. TASK NUMBER	
				5f. WORK UNIT NUMBER	
7. PERFORMING ORGANIZATION NAMES(S) AND ADDRESS(S) Air Force Institute of Technology Graduate School of Engineering and Management (AFIT/EN) 2950 Hobson Way WPAFB, OH 45433-7765 DSN: 785-3636				8. PERFORMING ORGANIZATION REPORT NUMBER AFIT/DEE/ENG/10-13	
9. SPONSORING/MONITORING AGENCY NAME(S) AND ADDRESS(ES) The Air Force Office of Scientific Research 875 N Randolph St, Suite 3112 Arlington, VA 22203				10. SPONSOR/MONITOR'S ACRONYM(S) AFOSR/NE	
				11. SPONSOR/MONITOR'S REPORT NUMBER(S)	
12. DISTRIBUTION/AVAILABILITY STATEMENT APPROVED FOR PUBLIC RELEASE; DISTRIBUTION UNLIMITED					
13. SUPPLEMENTARY NOTES					
14. ABSTRACT The purpose of this research effort is to improve and characterize range estimation in a three-dimensional FLASH LAsER Detection And Ranging (3D FLASH LADAR) by investigating spatial dimension blurring effects. The myriad of emerging applications for 3D FLASH LADAR both as primary and supplemental sensor necessitate superior performance including accurate range estimates. Along with range information, this sensor also provides an imaging or laser vision capability. Consequently, accurate range estimates would also greatly aid in image quality of a target or remote scene under interrogation. Unlike previous efforts, this research accounts for pixel coupling by defining the range image mathematical model as a convolution between the system spatial impulse response and the object (target or remote scene) at a particular range slice. Using this model, improved range estimation is possible by object restoration from the data observations. Object estimation is principally performed by deriving a blind deconvolution Generalized Expectation Maximization (GEM) algorithm with the range determined from the estimated object by a normalized correlation method. Theoretical derivations and simulation results are verified with experimental data of a bar target taken from a 3D FLASH LADAR system in a laboratory environment. Additionally, among other factors, range separation estimation variance is a function of two LADAR design parameters (range sampling interval and transmitted pulse-width), which can be optimized using the expected range resolution between two point sources. Using both CRB theory and an unbiased estimator, an investigation is accomplished that finds the optimal pulse-width for several range sampling scenarios using a range resolution metric.					
15. SUBJECT TERMS Laser radar, range estimation, image processing, blind deconvolution					
16. SECURITY CLASSIFICATION OF:			17. LIMITATION OF ABSTRACT	18. NUMBER OF PAGES	19a. NAME OF RESPONSIBLE PERSON
REPORT	ABSTRACT	c. THIS PAGE			Dr. Richard K. Martin
U	U	U	UU	163	19b. TELEPHONE NUMBER (Include area code) 937.255.3636 x4625 email: richard.martin@afit.edu